ABSTRACT

Title of Document: MEMORY-RELATED COGNITIVE MODULATION OF HUMAN AUDITORY CORTEX: MAGNETOENCEPHALOGRAPHY-BASED VALIDATION OF A COMPUTATIONAL MODEL

Feng Rong, Doctor of Philosophy 2008

Directed By: Dr. José L. Contreras-Vidal
Department of Kinesiology, School of Public Health, University of Maryland – College Park

It is well known that cognitive functions exert task-specific modulation of the response properties of human auditory cortex. However, the underlying neuronal mechanisms are not well understood yet. In this dissertation I present a novel approach for integrating 'bottom-up' (neural network modeling) and 'top-down' (experiment) methods to study the dynamics of cortical circuits correlated to short-term memory (STM) processing that underlie the task-specific modulation of human auditory perception during performance of the delayed-match-to-sample (DMS) task. The experimental approach measures high-density magnetoencephalography (MEG) signals from human participants to investigate the modulation of human auditory evoked responses (AER) induced by the overt processing of auditory STM during

task performance. To accomplish this goal, a new signal processing method based on independent component analysis (ICA) was developed for removing artifact contamination in the MEG recordings and investigating the functional neural circuits underlying the task-specific modulation of human AER. The computational approach uses a large-scale neural network model based on the electrophysiological knowledge of the involved brain regions to simulate system-level neural dynamics related to auditory object processing and performance of the corresponding tasks. Moreover, synthetic MEG and functional magnetic resonance imaging (fMRI) signals were simulated with forward models and compared to current and previous experimental findings. Consistently, both simulation and experimental results demonstrate a DMS-specific suppressive modulation of the AER and corresponding increased connectivity between the temporal auditory and frontal cognitive regions. Overall, the integrated approach illustrates how biologically-plausible neural network models of the brain can increase our understanding of brain mechanisms and their computations at multiple levels from sensory input to behavioral output with the intermediate steps defined.

MEMORY-RELATED COGNITIVE MODULATION OF HUMAN AUDITORY CORTEX: MAGNETOENCEPHALOGRAPHY-BASED VALIDATION OF A COMPUTATIONAL MODEL

By

Feng Rong

Dissertation submitted to the Faculty of the Graduate School of the
University of Maryland, College Park, in partial fulfillment
of the requirements for the degree of
Doctor of Philosophy
2008

Advisory Committee:
Professor José L. Contreras-Vidal, Chair
Professor Barry Horwitz
Professor Jane Clark
Professor Todd W. Troyer
Professor Jonathan Z. Simon
Professor James A. Reggia

I dedicate this dissertation with all my love and gratitude to my grandmother

Acknowledgements

I gratefully thank my advisors, Dr. Contreras-Vidal and Dr. Horwitz for kindly offering me opportunities to pursue my research in their labs, patiently guiding me through each step, and for making this process a joyful challenge.

I sincerely thank my committee members: Dr. Jane Clark, Dr. Todd Troyer, and Dr. Jonathan Simon for all of the academic guidance, the stimulating advices on my studies, and all the kindness. I also want to thank Dr. James Reggia, who kindly admitted to be the Dean's representative in the committee.

I extend my deep appreciation to my colleagues and my friends, Bruce Swett, Michelle Costanzo, Trent Bradberry, Hyuk Oh, Anusha Venkatakrishnan, Rodolphe Gentili, Fatima Husain, Hung Thai-Van, Jieun Kim, Jason Smith, Marina Papoutsi, Yukiko Kikuchi, Ping Du, Huan Luo, Xing Tian, Youjun Wang, Juanjuan Xiang, and so many more, for their helps and encouragement.

My heart goes out to Pamela Komarek, Deborah Jones, and Sandy Davis, who have been of incredible help to me.

Finally, I want to thank my family, my parents and my mother in law, their unselfish help always arrives when we need. And my little angel, Iliana, who is the best gift I can have and the prettiest thing I can imagine in the world. At last and the most important, to the one I don't have enough word to express my heart, my wife, Haiyan …

Table of Contents

List of Tables

List of Figures

List of Abbreviations

A1	Primary auditory cortex
A2	Secondary auditory cortex
AEF	Auditory Evoked Fields
AER	Auditory Evoked Response
ANOVA	Analysis of variance
AP	Action Potential
ART	Adaptive Resonance Theory
BOLD	Blood-Oxygen-Level Dependent
CNT	Counting
DICS	Dynamic Imaging of Coherent Sources
DMS	Delayed-Match-to-Sample
ECD	Equivalent Current Dipole
EEG	Electroencephalography
EPSP	Excitatory Postsynaptic Potential
ERF	Event-Related Field
FM	Frequency Modulated
fMRI	functional Magnetic Resonance Imaging
HG	Heschl's Gyrus
IC	Independent Component
ICA	Independent Component Analysis
IPSP	Inhibitory Postsynaptic Potential
ISI	Inter-Stimulus Interval
LCMV	Linearly Constrained Minimum Variance
MEG	Magnetoencephalography
MGN	Medial Geniculate Nucleus
MI	Modulation Index
PFC	Prefrontal Cortex
PP	Planum Polare
PSC	Percentage Signal Change
PSD	Power Spectral Density
PSL	Passive Listening
PSP	Postsynaptic Potential
PT	Planum Temporale
RMS	Root Mean Square
SI	Source Index
SQUID	Superconductive Quantum Interference Device
STG	Superior Temporal Gyrus
STM	Short-Term Memory
STS	Superior Temporal Sulcus
TC	Tonal contour

CHAPTER 1. GENERAL INTRODUCTION AND BACKGROUND STUDIES

Traditionally, the auditory cortex has been viewed as a refinement along a continuum of information processing beginning at the thalamocortical afferent pathways to represent the temporal, spectral and spatial properties of sounds (Rauschecker 1998; Kaas et al. 1999). However, recent studies have revealed task specificity of auditory cortical responses to the acoustic stimuli that reflect complex top-down guidance in these refinements (Fritz et al. 2005, 2007; Scheich et al. 2007). While the observed phenomena have been interpreted as consequences of interactions between the feedforward afferent and feedback modulation pathways, exactly when and where the modulations are exerted during the task performance remain illusive and still beg for further investigations to understand the underlying neuronal mechanisms. In this dissertation, I combined the 'bottom-up' modeling and 'top-down' brain imaging methods with a specific auditory task to study cortical dynamics underlying the task-specific modulation of human auditory perception.

1.1 Task-specific modulation of auditory object perception

1.1.1 Hierarchical pathway of auditory object perception

Auditory object refers to the acoustic events that can be perceived as one unit (Kubovy & Van Valkenburg 2001). For example, melodic segments, words, animal communication sounds, and environmental sounds are all well-known auditory objects. A plausible approximation of these objects is that they can be described by

compositions of frequency modulated (FM) sweeps and tones, and perception of them requires not only the processing of the temporal and spectral features, but also the direction of the sweeps and their transitions. Cortical processing of auditory objects involves multiple brain regions, such as the primary (A1) and secondary (A2) auditory cortex, anterior and posterior regions in superior temporal gyrus and/or sulcus (STG/STS), and prefrontal cortex (PFC). The primary auditory cortex locates at the anterior part of the transverse temporal gyrus (Heschl's gyrus, HG) within the Sylvian fissure, receives tonotopically organized inputs from the medial geniculate nucleus (MGN) in thalamus (Hall et al. 2002). In human EEG/MEG studies, the peak of the evoked responses in A1 can be observed as early as 20 ms after stimulus onset (Lutkenhoner et al. 2003). There are two secondary regions located lateral to A1 -- planum polare (PP, anterior to HG) and planum temporale (PT, posterior to HG). Although borders between these regions are not clearly defined (Westbury et al. 1999), studies have shown that PP has finer tonotopic organization (Zattorre & Berlin 2001) and PT has broader tuning of frequencies but higher sensitivity to sound motion (Warren et al. 2002), which suggests that PP may play a more important role in processing the basic features of auditory objects. STG/STS refer to the regions either anterior or posterior to the secondary auditory cortex in the superior temporal gyrus/sulcus, which integrate the inputs from A2 to construct an abstract 'percept' of the sound stimulus and can retain it for a short period (Colombo et al. 1990; Zatorre & Samson 1991). In the auditory cortices, sensitivity to FM sweeps has been observed in both nonhuman primate (Rauschecker et al. 1997; Rauschecker 1998; in belt area) and human studies (Binder et al. 2000; Hall et al. 2002; in primary auditory

areas and STG/STS). Furthermore, lesion of bilateral ST has shown impairment of the monkeys' ability to perform a pattern discrimination task (Colombo et al. 1996). For the frontal regions, neurons in the ventrolateral prefrontal cortex (vlPFC) have shown activity correlated to representation and short-term storage of the stimuli's acoustic features (Romanski et al. 1999; Romanski & Goldman-Rakic 2002; Romanski 2004). In addition, anatomical studies have shown both feedforward (Romanski et al. 1999) and feedback (Budinger et al. 2000a, 2000b, 2006) connections between the auditory and frontal regions. These experimental evidences point to the crucial roles of these cortices in the perception of auditory objects.

1.1.2 Task-specific cognitive modulation of auditory cortex

Classical theory views the physiological function of the auditory cortices as intermediate stations that relay information from subcortical regions to higher cognitive centers. However, both animal and human studies have shown active modulation of the auditory cortical activities. In animal studies, modulations have been demonstrated by changes in the representational properties of A1 neurons, such as shift of the firing pattern among neurons by the context of previously presented stimuli (Condon & Weinberger 1991; Malone et al. 2002; Ulanovsky et al. 2003; Bartlett & Wang 2005) and changes in properties of receptive fields as a function of behavioral states (Gottlieb et al. 1989; Fritz et al. 2005). In human beings, both hemodynamic and electromagnetic studies have shown modulations of the auditory response patterns by attention (Hillyard et al. 1973; Woldorff et al. 1993; Fujiwara et al. 1998; Hughes & Jones 2003; Sabri et al. 2006; Ahveninen et al. 2006), memory (Stanny & Elfner 1980; Lu et al. 1992; Luo et al. 2005), task requirement (Chait et al.

2004) and perceptual decision (Pollmann et al. 2006). An important aspect of the modulation effects demonstrated by EEG/MEG studies is the suppression of the N1/M100 response, which has been observed in both passive tasks such as listening to repeated stimuli (May et al. 1999), and active tasks such as rare sound detection (Haenschel et al. 2005), dichotic listening (Hillyard et al. 1973; Woldorff et al. 1993; Fujiwara et al. 1998; Brancucci et al. 2004), discrimination (Melara et al. 2005) and working memory paradigms (May & Tiitinen 2004; Luo et al. 2005; Lu et al. 1992). It has been proposed that the suppression effect results from 'neuronal adaptation' in response to the repeated presentations of the same sounds (for review, see Baldeweg 2006). However, since the suppression effects also have been found in other tasks which do not involve repetitive presentation of the same stimuli (Luo et al. 2005, Lu et al. 1992), it is suggested that task-specific active modulation mechanisms, other than neuronal adaptation, might also be underlying the suppression effect observed during performing the tasks.

The underlying mechanism of the cognitive modulation has been hypothesized as either by intrinsic dynamics (Wehr & Zador 2005) or feedback modulation from downstream cognitive processes. The hypotheses of feedback modulation include biasing the competition to favor the relevant information processing (Miller & Cohen 2001; Deco & Rolls 2005), or by predicting upcoming sensory events (Friston 2005). In these hypothesized mechanisms, frontal regions have drawn much more attention: They're proposed to provide biasing signals to preferentially strengthen the task-relevant processing (Miller & Cohen 2001) and specifically inhibit the task-irrelevant or unwanted stimuli (Aron et al. 2004; Aron

2007). They may also be involved in holding a short-term storage of the stimuli and use them for perceptual decision (for a recent review, see Funahashi et al. 2006); They may even be important for predicting the upcoming stimuli based on either a statistical estimation by experience (Friston 2005) or by estimation of the sensory outcome (or reafference) through the use of the efference copy of the prepared motor behavior and an internal model of the interaction between the body and the environment (Wolper & Kawato 1998, Martikainen et al. 2005, Chen et al. 2006). Therefore, investigation of the functional connectivity between the frontal and sensory regions will help us to further our understanding of the top-down modulation mechanisms and the neural circuits underlying auditory information processing.

1.1.3 Delayed-match-to-sample (DMS) task and DMS-specific neuronal activity

This dissertation uses an auditory delayed-match-to-sample (DMS) task to investigate the task-specific modulation of human auditory cortex. Auditory DMS task requires the participants to discriminate given features between a pair of sounds interleaved by a delay period (Posner 1967). Performing the DMS task involves the formation, maintenance, and manipulation of the short-term memory (STM) for the specified features of the first sound in the pair during the delay period, thus the participant could make judgment based on the comparison between the memorized features of the first sound and the perceived features of the second one (Postle et al. 1999). Neurons in both prefrontal (Romanski et al. 1999; Romanski 2004; Romanski & Goldman-Rakic 2002) and auditory (Gottlieb et al. 1989; Zatorre et al. 1994) cortices have been demonstrated to show response patterns reflecting the memorized features of the stimulus, and lesion studies have shown both regions (Zatorre &

Samson 1991; Knight et al. 1999) are necessary for successful performance of the task. While participants are performing the task, the involved cortical regions display a complicated activity pattern: increase of the beta band activity is observed in the frontal regions during the first half of the delay period while increase of the alpha band activity in the temporal region kicks in later during the late delay period (Klimesch 1997; Luo et al. 2005). In addtion, in frontal regions, increased activity in theta band (Klimesch et al. 1999, 2007) and gamma band (Leiberg et al. 2006a, b) have also been observed during the delay period. There are two major modulation effects that have been shown in the auditory cortex while performing the auditory DMS task: (1) suppression of the evoked responses to the second sound (Luo et al. 2005), and the suppression becomes weaker with longer delay period (Lu et al. 1992); (2) The auditory neuronal responses to the second sound depend on whether it matches the first one. For instances, studies of the nonhuman primate's auditory neuronal activity during performance of a DMS task showed both neurons that increased response to the nonmatched sounds while similar activity level to the matched sounds and neurons with decreased response to the matched sounds while similar response level to the nonmatched sounds (Goettlieb et al. 1989). These experimental findings indicate that, while performing the auditory DMS task, both temporal and frontal cortical regions show task-related dynamics which are reflected by various spectral components. And the modulation of the evoked response to the second sound is influenced by the stimuli context in each pair and possibly the memory trace formed during the delay period. However, it is unclear whether this modulation effect is due to adaptation to the repeatedly-presented sound stimuli or is

specifically related to the task. Therefore, it is important to assess the task-specificity of the modulation effect and examine the functional connectivity patterns between temporal and frontal regions during task performance in order to understand the underlying neural mechanisms of the modulation effect.

Both regional (Tagamets et al. 1998; Husain et al. 2004) and neural mass models (Moody & Wise 2000; Gisiger et al. 2005) of DMS task have been proposed to simulate the neuronal dynamics during task performance. There are also models focusing on the influence of attention (Deco & Rolls 2005) and neuromodulation (Chadderdon & Sporns 2006) to neuronal activities. One of these models simulates the regional dynamics during performance of auditory DMS task (Husain et al. 2004). This model is composed of modules representing the MGN, Ai, Aii, ST, PFC regions, where each region consists of basic units that represent local populations of neurons firing consistently during the task performance. The PFC region contains memory-processing units and response units, where the manipulation of the gain value to the memory unit can simulate the task conditions such as DMS and rest. DMS correlated fMRI signal also was simulated using the forward model in this study. In this dissertation, I expanded this model to simulate the DMS-specific modulation of AER in MEG measurements and corresponding dynamics in fMRI signals.

1.2 Exploring human cognitive function – integration of 'top-down' and 'bottom-up' approaches

1.2.1 'Top-down' approaches: brain imaging methods

Non-invasive brain imaging techniques have provided powerful tools for simultaneously investigating the neural dynamics, interactions between neural substrates of multiple brain regions by measuring brain activity correlated with external signals using appropriate psychophysiological paradigms. Among these techniques, Magnetoencephalography (MEG) and Electroencephalography (EEG) detect the weak electric or magnetic fields generated by the synchronized intracellular synaptic currents (Baillet et al. 2001; Hämäläinen et al. 1993); while functional magnetic resonance imaging (fMRI) and Positron Emission Tomography (PET) signals reflect the metabolic related hemodynamic changes related to changes of regional blood flow, blood volume and blood oxygen level in the brain (Ogawa et al. 1992). Besides measurements of different types of brain activity related signals, these types of techniques show differences in their sensitivities to brain dynamics in different spatial or temporal scales: MEG/EEG have temporal resolution in the millisecond order but relatively poor spatial resolution (in the order of centimeters) due to signal smearing by the low conductive skull (Nunez & Srinivasan 2006), limitation of the spatial measurement (up to several hundred of sensors) and inherent static electromagnetic inverse problem (Baillet et al. 2001). In contrast, fMRI/PET have spatial resolution in the millimeter range but poor temporal resolution (in the order of seconds or tens of seconds) given the relatively slower changes of the hemodynamic response (Ogawa et al. 1992).

1.2.1.1 Instrumentation of MEG

MEG measures the weak extracranial magnetic fields from living human beings. It is based on the sensitive detector called the superconducting quantum interference device (SQUID). Immersed in a dewar cooled by liquid helium, SQUID can detect the very weak changes of magnetic flux generated by brain activity at the femto (1×10^{-15})-Tesla levels, which is around 10 to 11 orders of magnitude smaller than the strength of the earth's magnetic field. Modern MEG scanners usually have multisensor arrays that contain up to 300+ SQUID magnetometers, which can cover the whole head of the subject and record the magnetic flux across multiple sites simultaneously. The signals are commonly recorded inside a magnetic-shielded room to reduce the influence of environmental magnetic fields. In addition to the magnetic-shielded room, the gradiometer coil configurations (e.g. The third-order gradiometer used in CTF 275 system) are used to reduce other instrumental noises (for review, see Hämäläinen et al. 1993).

1.2.1.2 Neural basis of MEG signals

Two major sources of electric signals in neural systems are action potentials (AP) and post-synaptic potentials (PSP). The detectable extracranial magnetic flux recorded by MEG is believed to be generated by the synchronized PSP of pyramidal cells (Hämäläinen et al. 1993). Constituting 75~80% of the neuronal population in neocortex (Buxhoeveden & Casanova 2002), the pyramidal cells have asymmetrically morphological and roughly parallel oriented apical dendritic trees (Mountcastle 1979). Arrival of impulses through the pre-synaptic axons at the synapses along the apical dendrite of the post-synaptic neuron changes the permeability of ion channels

near the synaptic site, which in turn either increases or decreases the intracellular potential. Therefore, the potential difference between the synaptic site and the soma generates the current flow along the dendrite. Each PSP can be represented by an equivalent current dipole (ECD) with the strength of 20 fA·m, but the detectable strength of source current with MEG is in the order of 10 nA·m, thus the detectable current source measured by MEG is generated by synchronous flow of post-synaptic current in the same direction among thousands of pyramidal cells (Baillet et al. 2001).

Current sources underlying the MEG signals are composed of two components: the primary current is the intracellular current flow along the dendritic tree due to the depolarization (excitatory postsynaptic potential, EPSP) or hyperpolarization (inhibitory postsynaptic potential, IPSP) of the membrane potential near the synaptic site. The induced extracellular passive ohmic current closes the loop of current flow with flow in the opposite direction through the surrounding medium, which is called the volume current or return current. The magnetic field is generated by both primary and volume current. Spreading in all directions through brain tissue, cerebro-spinal fluid, skull and scalp to the sensors, the magnetic field recorded by each sensor of the MEG scanner contains information of all functional sources in the brain, which contributes to the ill-posed inverse problem of MEG for estimation of the sources from measurements at the sensors.

1.2.1.3 Forward and inverse solutions of MEG

The forward solution of MEG is to calculate the extracranial magnetic field at the location of the MEG sensors given the putative primary current inside the brain. As showed in Appendix A, given a selected head model and known location of the

sensors, estimation of the magnetic field is linearly correlated to source dipole current and depends on the geometric properties of the head models with consideration of the return currents, the remaining variables for estimating the magnetic field with the simulated dipole current include the location of the dipole and the orientation and magnitude of the dipole moment. Numerous head models for either analytical or numerical forward solutions have been developed for MEG, across a wide spectrum from the simplest one-layer semi-infinite volume sphere model (Cuffin & Cohen 1977) to the complicated three-layer real-shape head model based on boundary element method (Hämäläinen & Sarvas 1989). In this dissertation, a sensor weighted overlapping sphere head model (Huang et al. 1999) is used to take advantage of both the real head shape and relatively lower computational cost provided by this model.

The inverse solution provides an estimate of the source current with the sensor measurement, and usually requires the lead field computed from the forward solution. Due to the ill-posed inverse problem, the estimation of the sources is usually based on certain constraints or assumptions, such as the approximation of minimized variance for each source used in beamformer techniques (van Veen et al. 1997). In this spatial filter beamformer, a three dimensional grid of sources covering the whole head of the subject is constructed. Each voxel in the grid contains one equivalent current dipole (ECD) with its base at the center of that voxel. The lead field is built upon the selected head model, and is computed with a unit virtue dipole in each voxel. Computation of the transform matrix to calculate the ECD for each source with a spatial filter beamformer is illustrated in detail in Appendix B.

1.2.1.4 Analysis and interpretation of MEG signal

Analysis of measured MEG signals usually takes pre-processing steps first to reduce the noise and remove the artifacts from the signal. Further analysis is then taken either in the manner of event-related analysis by averaging across the epochs aligned to time markers of certain events, such as onset of sound stimuli, or in the manner of induced response analysis by measuring the phase change of the spontaneous activity correlated to certain sensory, cognitive or behavioral paradigm. Interpretation of the experimental results obtained from analysis of the MEG measurements usually takes into account changes of magnetic field patterns across the sensors or activity patterns across estimated sources, as well as the changes of the connectivity pattern among the sensors or sources, correlated to the experimental behavioral paradigm (Hari 1990; Hämäläinen et al. 1993; Baillet et al. 2001). This work focuses on the dynamics of the auditory evoked field (AEF) in sensor space and corresponding auditory evoked responses (AER) in source space, as well as the dynamics of the functional connectivity between cortical regions during performance of the DMS task.

1.2.1.5 Isolate artifact and function-related signals in MEG: independent component analysis (ICA) and categorization of independent components

One of the essential problems in MEG data analysis is that the measurement on each sensor is a mixture of magnetic fields generated by multiple sources, including both the artifact-related non-brain sources and the functioning neural activities inside the brain. Thus how to isolate/sort out the signal of interest and remove the irrelevant artifacts becomes the first obstacle in analyzing the MEG data.

By blindly decomposing the multi-channel recordings into spatially fixed and temporally independent components (Bell and Sejnowski, 1995), independent component analysis (ICA) has proven to be an efficient tool in reducing the complexity of MEG signal processing (Vigario et. al. 2000). For each independent component (IC), the fixed projection on the sensors (which is called a 'scalp map') provides spatial information of the biological sources, irregardless of their activation source size and whether they are locally activated or broadly distributed, at the same time the maximally independent activation denotes the accurate timing of the events, which is extremely useful in identifying the sources of the evoked-responses (Makeig et al. 1997). Compared to direct application of source localization methods on raw MEG data, ICA carries two main advantages: (1) It can identify and remove signal artifacts such as eye movements, heart beat and muscle activity produced during the experimental measurements (Vigario et. al. 2000, Tang et. al. 2002, James et. al. 2003, Barbati et. al. 2004); and (2) it can provide accurate temporal information on the dynamics of much fewer functioning neural circuits as compared to the raw MEG signal (Contreras-Vidal & Kerick 2004; Makeig et. al. 1999; Makeig et. al. 2001; for review, see Delorme et. al. 2004), which in turn will help to improve the analysis of the correlated activities among co-activated brain regions with greatly reduced dimensionality.

The advantage of applying ICA in artifact rejection is mainly manifested in comparison to the segment-rejection method, which is based on signal thresholds for the detection of large artifacts such as eye blinks. The segment-rejection method requires an arbitrarily-set magnitude threshold, which makes the identification and

rejection of artifacts with smaller magnetic fields such as heart beat difficult (Hämäläinen et al, 1993). Moreover, as this approach also requires rejection of data segments that are identified to have artifacts, valuable brain activity information contained in the rejected segment is lost with the artifacts. In contrast, by applying IC to identification and rejection of the artifacts, it is possible to recover the functional brain activities masked by artifactual signals thus save the useful information from mass data loss.

While patterns of scalp maps and activities of the ICs can be identified and correlated to both artifacts and functional signals, it has been shown that the ICs computed from different trials and different individuals vary in both spatial and temporal patterns, despite the fact that they are correlated to the similar biological events. Visual examination across the trials for artifact rejection is not only inefficient, but also arbitrarily dependent on the person doing the analysis. Thus, to develop an automatic artifact identification method based on the features of the ICs for MEG data analysis becomes necessary in concerns of time and labor efficiency, as well as accuracy and reliability of data analysis. This dissertation presents an automatic IC identification tool with iterative clustering methods based on the spatial, spectral and informational features of the ICs to categorize both artifacts and evoked response related ICs.

1.2.2 'Bottom-up' approaches: Large-scale neural network modeling

As discussed in the sections above, MEG is capable of providing insightful data to infer the evoked and ongoing neuronal activities related to sensory, motor and cognitive functions in human brain. However, congruent interpretation of these

findings with other functional brain imaging studies and correlating them with the understanding of neural dynamics obtained from microscopic electrophysiological recordings in either non human animals or neurosurgical patients have proven to be difficult tasks due to the different spatial and temporal resolution and the different methods of measurement (e.g. invasive vs. non-invasive) among the techniques. In the effort to bridge the gaps between multiple levels of knowledge acquired, 'bottom-up' approaches, which simulates either hemo-metabolic or electromagnetic dynamic signals based on a general biophysical realistic neural network model, have been proposed in various studies (Tagamets & Horwitz 1998, Husain et al. 2004, Horwitz & Poeppel 2002, David & Friston 2003). Furthermore, the modeling approach, by taking the assumptions and constraints inferred from other anatomical, physiological and behavioral studies, can provide common substrates for simulation of the system dynamics under different cognitive, behavior, and pathological conditions, which, in combine with more experimental studies, can help to corroborate the conclusions from experimental data as well as revealing possible directions for further experiments. Here, I explore the combination of these two approaches -- a 'bottom-up' simulation supported by a 'top-down' analysis and show that it provides much deeper understanding of the neuronal activity involved in certain cognitive function that either approach could do by itself.

1.2.2.1 Modeling the evoked responses in EEG/MEG

Although it is known that synchronized intracellular synaptic current of the pyramidal cells and correlated volume currents are the main contributor of the EEG/MEG signal, and using equivalent current dipole and forward models can

simulate the evoked responses observed in EEG/MEG studies (Nunez & Silberstein 2000), only recently a few models have been developed to simulate the network dynamics of the evoked responses during task performance. David and Friston (2003) postulated the method of simulating the evoked responses with dynamic causal modeling (DCM) and addressed the modulation of AER in an oddball paradigm (Kiebel et al. 2006). A recent layer-specific model of somatosensory evoked fields (SEF) also simulated task-related local neuronal activities and their contributions to the observed changes in SEF in a tactile detection paradigm (Jones et al. 2007). Here I take a similar approach by estimating the simulated integrated synaptic activity from a biophysically realistic network model, and using this estimation to obtain the forward solution with specified source location, orientation and source-sensory relationship to simulate the auditory evoked responses and the corresponding modulation during task performance.

1.2.2.2 Modeling the BOLD signal

In contrast to MEG, many more approaches have been taken to correlate the multiple regional neuronal electrophysiological dynamics to the fMRI signal (Tagamets & Horwitz 2000, 2001; Corchs & Deco 2002; Husain et al. 2004; Riera et al. 2004; Marreiros et al. 2008). Particularly, the neuronal activity, integrated synaptic activity (ISA) and corresponding fMRI signals of the regions involved in performing the auditory DMS task have been simulated and compared with the experimental results (Husain et al. 2004), in which most of the regions except the primary auditory cortex showed comparable BOLD signal changes to the experimental results. The similarity across these approaches is that hemodynamic response functions (HRF)

were used as the mediator between the regional ISA and synthetic BOLD signal, as experimentally proved (Logothetis 2001, 2002, 2003). However, it is worthy to note that the excitatory and inhibitory PSP (EPSP and IPSP) are assumed to contribute cumulatively to the BOLD signal (Logothetis 2003; Tagamets & Horwitz 2001), which is different from their contributions to the EEG/MEG signals, in which IPSPs are canceled from EPSPs to generate the moment strength of ECDs for forward simulation. This leads to fundamental problem when one tries to correlate results obtained from EEG/MEG and fMRI experiments, as I will mention in the following part.

1.2.2.3 Integrated models of MEG and fMRI

Since it has been proven that postsynaptic currents are the common source of forward solution for both MEG and fMRI, it seems quite obvious that we should try to combine and reconcile results obtained by both techniques to take advantage of their complementary features of superb temporal and spatial resolution. However, this turns out to be a rather difficult problem. Nunez and Silberstein (2000) have listed the difficulties of coupling the understanding from the analysis of MEG and fMRI signals: (1) for a detectable BOLD signal, the underlying EPSP and IPSP can cancel each other and produce no MEG signal; whereas (2) a small amount of synchronized PSP (although still in the order of thousands) can generate large MEG signal but the corresponding BOLD signal will be weak. In recent years, several computational models have emerged to address these problems and integrate the modeling of EEG/MEG and fMRI (Babajani et al. 2005, 2006, Riera et al. 2005, Liu et al. 2006, Sotero et al. 2008) to achieve both high spatial and temporal resolution. A common

feature of these models is that the postsynaptic currents for simulation of EEG/MEG and fMRI signals are integrated separately to address the difficulties mentioned above.

In this dissertation I choose to simulate both MEG and fMRI signals relevant to the performance of the auditory delayed-match-to-sample (DMS) task. In contrast, for the experimental approach I focus on MEG measurements with exquisite temporal resolution (~1.6 ms), since the fMRI correlates of the auditory DMS task have been investigated in a prior study (Husain et al. 2004). With this integrated approach, I investigate the task-specificity of the cognitive modulation of human auditory cortex and the neural mechanisms underlie the observed dynamics in evoked responses and BOLD signals.

CHAPTER 2. ISOLATING ARTIFACT AND FUNCTION SIGNALS IN MEG – AN AUTOMATIC CATEGORIZATION METHOD FOR INDEPENDENT COMPONENT ANALYSIS

This chapter illustrates a method for combining independent component analysis (ICA) and clustering algorithms to isolate the artifact and function-related signals from experimental MEG measurements. The method and its application in categorization of artifact-related independent components (IC) were described in the Journal of Neuroscience Method (Rong & Contreras-Vidal, 2006), and it is attached to this dissertation for completeness. As the first author, I had following contributions to this paper:

(1) Participated in experimental design and MEG data collection.

(2) Participated in developing the categorization method.

(3) Analyzed the data and produced the figures and tables in the paper.

(4) Participated in writing and revising the manuscripts.

ELSEVIER

Journal of Neuroscience Methods 157 (2006) 337–354

JOURNAL OF NEUROSCIENCE METHODS

www.elsevier.com/locate/jneumeth

Magnetoencephalographic artifact identification and automatic removal based on independent component analysis and categorization approaches

Feng Rong [a], José L. Contreras-Vidal [a,b,*]

[a] *Department of Kinesiology and Neuroscience and Cognitive Science Program, University of Maryland, College Park, MD 20742, United States*
[b] *Bioengineering Program, University of Maryland, College Park, MD 20742, United States*

Received 23 June 2005; received in revised form 24 April 2006; accepted 26 April 2006

Abstract

Artifact signals from eye movements, heart beat and muscle activity contaminate magnetoencephalographic (MEG) signals generated from the neural activities inside the brain. Rejection of contaminated trials not only causes data loss, but can also significantly increase the experimental time or even prevent the analysis of highly contaminated or noisy data. We combined the use of independent component analysis (ICA) and clustering methods to isolate the artifacts from MEG signals. Threshold-based clustering analyses based on the topographic pattern, statistical aspects and power spectral patterns of independent components (ICs) successfully identified ICs related to certain types of artifacts. Unsupervised neural network based on the Adaptive Resonance Theory (ART) also categorized the artifact ICs, albeit with lower accuracy. Performance of the identification methods were evaluated with measurements of underestimation and overestimation of the target artifactual ICs. The combination of threshold-based clustering and ART-2 neural network categorization methods demonstrated the best identification performance. Comparison between contaminated and artifact-cleaned MEG signal waveforms showed the efficiency of the proposed methods of artifacts rejection. The analysis of the artifact components suggested the possibility of automatic artifact removal based on general templates.

Keywords: Artifacts; Magnetoencephalography; ART-2; Categorization; Clustering; ICA

1. Introduction

The analysis of magnetoencephalography (MEG) signals always requires the identification and removal of artifacts such as eye movements, heart beat and muscle activity due to head and hand/arm movements produced during the experimental session. These biological events contaminate the MEG signals generated by task-relevant brain activities and thus make direct analysis of the MEG signal with artifacts difficult (Hämäläinen et al., 1993). Regression methods in the time domain (Hillyard and Galambos, 1970) and the frequency domain (Woestenburg et al., 1983) have been proposed for the removal of eye movements and other artifacts in electroencephalographic (EEG) signals. However, the lack of eye-movement reference electrodes in MEG recording makes it difficult to remove artifacts in MEG signals with these methods. Other methods based on signal thresholds for the detection of large artifacts such as eye blinks, need an arbitrarily set magnitude threshold, which makes the identification and rejection of artifacts with smaller magnetic field magnitude such as heart beat difficult (Hämäläinen et al., 1993). Moreover, as this approach requires rejection of data segments with artifacts, valuable brain information contained in the rejected segment represents an unacceptable data loss. Thus, the development of methods to identify the artifacts and remove them without loss of information related to the cerebral activity is of the utmost importance for MEG studies involving eye movements and/or subject motor responses.

Independent component analysis (ICA, Bell and Sejnowski, 1995) has been successfully applied to the processing of electroencephalography signals (Makeig et al., 1996; Delorme and Makeig, 2004). Various methods have been proposed in the identification of components related to artifacts in both EEG (Jung et al., 1998, 2000; Delorme et al., 2001; Joyce et al., 2004) and

* Correspondence to: 2363 HHP Bldg, Department of Kinesiology, University of Maryland, College Park, MD 20742, United States.
Tel.: +1 301 405 2495; fax: +1 301 405 5578.
E-mail addresses: rongfeng@glue.umd.edu (F. Rong), pepeum@umd.edu (J.L. Contreras-Vidal).

0165-0270/$ – see front matter © 2006 Elsevier B.V. All rights reserved.
doi:10.1016/j.jneumeth.2006.04.024

MEG (Vigario et al., 2000, Tang et al., 2002; James and Gibson, 2003; Barbati et al., 2004). The criteria used by most of these methods focus on a single feature of the artifactual components related to topographic patterns, statistical patterns, or spectral properties. One recent study claimed automatic detection of the artifactual components in MEG signal based on the analysis of the statistical and spectral aspects of the components (Barbati et al., 2004). However, this study did not take into account the scalp map of the components, which represents the fixed spatial feature of the components and has been used successfully in identification of the artifacts in former EEG studies (Delorme and Makeig, 2004).

Here we propose an approach for efficient artifact identification and automatic removal of MEG signals based on iterative clustering of independent components (ICs) features including the scalp map, the statistical and the spectral properties. Both threshold-based clustering in feature space and automatic neural network-based categorization were implemented for discrimination of certain types of artifacts in MEG signals. We report that both approaches can detect and remove artifacts for single-trial and multiple-trials (concatenated) MEG signals from datasets within subject and across subjects. Evaluations of performance showed that threshold-based clustering could identify the artifacts with higher accuracy, whereas the neural network categorization performed with minimal intervention from the researchers. The performance gain obtained by combining these two methods is also demonstrated, namely the improvement in alleviating overestimation and/or underestimation of target artifactual ICs.

We have applied our proposed methods for ICA-based artifactual IC identification and removal on both single-trial based epochs and the concatenated MEG signals (Delorme and Makeig, 2004). The iterative template updating used for the categorization and clustering of the identified components suggests that the same type of independent components with slightly different features can be clustered together. The statistical analysis of the feature values also showed that the components related to artifacts can be significantly discriminated with combination of two or more features. Since the proposed methods are not specific or restricted to any biological event, they may also be useful in the identification and categorization of ICs related to brain signals generated by similar functional brain networks.

2. Methods

2.1. MEG signal collection and pre-whitening

2.1.1. Participants

Five healthy right-handed adults volunteered to participate in the study after giving informed consent. All subjects had normal or corrected-to-normal vision. All procedures were approved by the Institutional Review Board at the University of Maryland, College Park.

2.1.2. Apparatus

Subjects lay supine on a table with their heads inside the recording dewar of the MEG device, which was located in a magnetic-shielded room in the KIT-MEG laboratory at the University of Maryland, College Park. The subjects performed center-out drawing movements with an optic pen on a glass panel in front of them (Fig. 1). During the experiment, the subjects' vision of the pen and their hands was occluded by a black curtain. A video camera placed over the glass panel captured the movement of the pen tip with a 60 Hz sampling frequency. The signal of the movement was transformed onto a screen cursor moving on a monitor screen outside the room and another glass panel over the subject's head, providing the subjects with visual information of the pen tip movement. The subjects' task was to draw a line from a home circle centered on the screen to one of the targets at the four corners of the screen. MEG signals were recorded with the 192-neuro-magnetometer-channel system (Kado et al., 1999). This system uses coaxial type first-order gradiometers which have a magnetic field resolution of 4 ft/$Hz^{1/2}$ or 0.8(ft/cm)/$Hz^{1/2}$ at the white noise region. One hundred and fifty seven channels (channel index 0–156) out of the 192 channels were used to record magnetic signals related to brain activity. The remaining 35 channels are commonly reserved for triggering or other purposes. In this experiment, four of these channels were used for temporal markers of behavioral events (160: target onset; 161: go signal; 162: movement onset; 163: target acquisition), and three channels (channel index 157–159) served as references for noise reduction (Adachi et al., 2001). The continuous MEG signals were sampled at 1 kHz and on-line filtered in the SQUID electric circuit units using three kinds of analog filters: high-pass filter (1st order Butterworth, fl = 1 Hz, attenuation step: 6 dB/octave), low-pass filter (2nd

Fig. 1. Experimental setup. The subjects' view of their hands and arms has been occluded during the experiment. The participants were asked to move an optic pen on a plexiglass panel in front of them. A camera captured the movement of the pen tip and transformed it into cursor movement on a screen over the subjects' heads.

order Butterworth, fh = 100 Hz, attenuation step: 12 dB/octave), and a notch filter (1st order paired band elimination filter, center frequency = 60 Hz, attenuation rate: >30 dB at center frequency).

2.1.3. MEG signal pre-whitening

The non-periodical low-frequency environmental noises (e.g., noise from urban traffic surrounding the MEG facility) recorded by three reference sensors during MEG measurements were pre-whitened using the continuously adjusted least square method (CALM, Adachi et al., 2001), which is implemented in MEG160 software (MEG Laboratory 2.001 M, Yokogawa Corporation, Eagle Technology Corporation, Kanazawa Institute of Technology). The pre-whitened MEG signal was epoched with 10.2 s time length, which corresponded to 10,201 samples per sensor per epoch. Each epoch was viewed as a single trial. Four datasets were constructed with the pre-whitened MEG signal to test the methods of ICA and artifactual IC identification: dataset one was from one randomly picked trial; dataset two consisted of 95 trials from one subject; dataset three contained 123 trials randomly selected across all five subjects, and dataset four contained 21 trials from one subject. Dataset four was used to compare the performance of artifactual IC identification methods when applying ICA on the concatenated continuous MEG signal and on single-trial based epochs. The proposed methodology for artifact identification and removal is illustrated in Fig. 2.

2.2. Independent component analysis

First, we applied Infomax ICA (EEGLAB v4.512, which was downloaded from http://www.sccn.ucsd.edu/eeglab/index.html) on the pre-whitened MEG signals. We did not use the extended ICA algorithm because the main target sources (artifactual sources) of this study were mainly supra-Gaussian distributed (kurtosis > 0) (Delorme and Makeig, 2004). For the first three datasets, ICA was applied on single-trial based epochs. For dataset four, ICA was applied on both a concatenated dataset and in single-trial based epochs.

For the application of ICA, we assumed that the MEG signal $x(t)$ was generated from sources $s(t)$ with a linear mixing

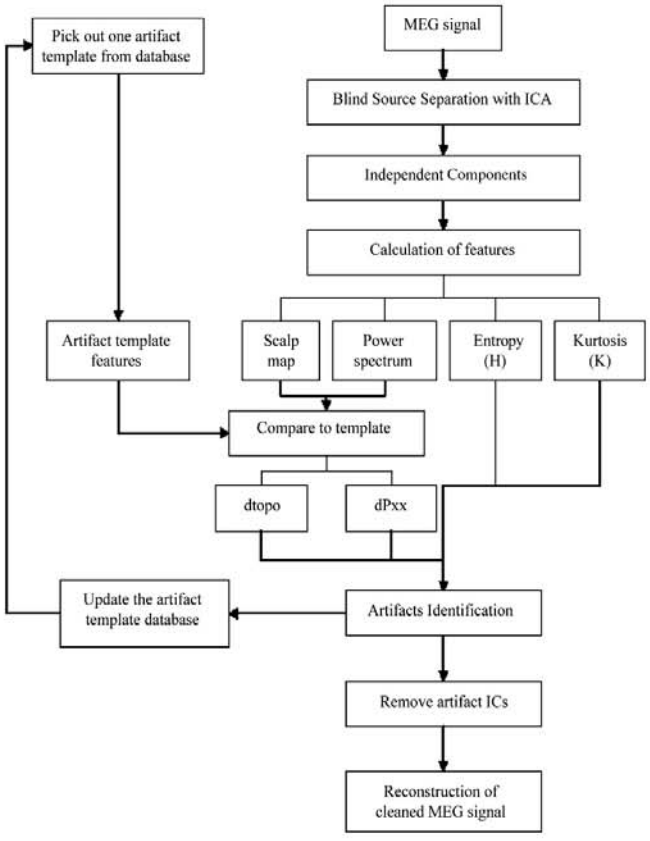

Fig. 2. The illustration of the procedure for independent component calculation, artifactual IC identification, template updating, artifact rejection and reconstruction of cleaned MEG signal.

procedure

$$x(t) = A\,s(t) \tag{1}$$

where t was a vector of the sampling time with length T, $x(t) = [x_1(t)\ldots x_n(t)]$ was a $n \times T$ matrix of noise reduced MEG signal recorded from n sensors; $s(t) = [s_1(t)\ldots s_m(t)]$ was a $m \times T$ matrix of m sources' activations; A was an unknown $n \times m$ full-rank mixing matrix. The application of ICA involved processing the MEG signals following the demixing procedure:

$$\hat{s}(t) = W\,x(t) \tag{2}$$

where $\hat{s}(t) = [\hat{s}_1(t)\ldots\hat{s}_m(t)]$ is an m-dimensional matrix of the independent components, which represents the estimation of the sources $s(t)$; W is a demixing matrix

$$W = \hat{A}^{+} \tag{3}$$

where $\hat{A}^{+}$ denotes an estimate of the pseudo-inverse of the mixing matrix A.

After the artifacts had been identified, the MEG signals were reconstructed with the components which have not been labeled as artifacts. Thus, in the *remixing* matrix, the weight vectors of the identified artifactual ICs have been set to zeros, such that

$$x'(t) = W^{+}_{\text{clean}}\hat{s}(t) \tag{4}$$

where $x'(t)$ is the reconstructed artifacts-free MEG signal for n sensors, W^{+} is the pseudo-inverse of the demixing matrix W, and W^{+}_{clean} is the $n \times m$ remixing matrix with its columns corresponding to the artifactual ICs set to zeros, $\hat{s}(t)$ is the activation matrix of ICs as mentioned above.

It is important to note that the application of Infomax ICA on EEG/MEG signals makes at least the following four assumptions (Vigario et al., 2000): (1) the underlying sources are statistically independent[1] and spatially stationary, however, if the total temporal independence cannot be reached, the sources are nevertheless computed with maximal independence to each other; (2) the sources do not have a Gaussian distribution[2]; (3) the components are characterized by a fixed, but possibly overlapping, spatial topography; and (4) the mixing process is instantaneous and stationary. The instantaneous mixing assumption can be met if we accept the quasi-static approximation of Maxwell equation (Jackson, 1999). The widely accepted current dipole model of the brain sources of MEG signals is congruent with the assumed stationarity of the ICs (Hämäläinen et al., 1993).

[1] Independence is not a strong constraint of ICA as ICA can be viewed as a maximum projection algorithm so it will find the sources which are maximally independent. This makes sense when studying brain processes as it is unreasonable to assume that the activity in one part of the brain is completely independent of the activity in another part of the brain.

[2] Strictly speaking, it is not necessary to assume for the information maximization in ICA that the sources not have a Gaussian distribution. In the case of Gaussian distributed signals, ICA merely degenerates to regular old PCA with summarized variance equivalent to information and uncorrelated components also being independent (Vigario et al., 2000).

2.3. Component feature calculation and clustering identification

Four feature values were calculated for identification of the artifactual ICs: the pairwise distance between topographic patterns (dtopo); the entropy of the component activations (H); the pairwise distance between the power spectral density patterns of the component activations (dPxx), and the global kurtosis coefficient of the component activations (K). The ICs were visualized as scatter points in feature space for threshold-based clustering of the artifactual ICs. For dataset one, the EKG-related artifactual ICs were clustered with criteria of dtopo ≤ 0.2, dPxx ≤ 0.5, $H \leq 2.78$ and $K > 0$, the ocular movement-related artifactual ICs were clustered with criteria of dtopo ≤ 0.2, dPxx ≤ 0.5, $H \leq 3.0$ and $K > 20$. For dataset two and three, the EKG related artifactual ICs were clustered with criteria of dtopo ≤ 0.2, dPxx ≤ 0.5, $H \leq 2.8$ and $K > 0$, the EOG1-related artifactual ICs were clustered with criteria of dtopo < 0.2, dPxx ≤ 0.5, $H \leq 3.0$ and $K > 10$. The EOG2-related ICs were clustered with criteria of dtopo ≤ 0.2, dPxx ≤ 0.5, $H \leq 3.0$ and $K > 10$. For dataset four, the threshold-based clustering methods used two sets of thresholds for each type of artifactual ICs, which are provided in Table 3.

2.3.1. Distance between IC topographic patterns

The ICs are commonly viewed as related to field activity with fixed spatially distributed sources (Makeig et al., 2002, 2004). In applications of ICA, the spatial distribution of sources is usually represented as scalp maps (Makeig et al., 2002, 2004) or field maps (Tang et al., 2002), which are represented mathematically as projection of the ICs on sensor space. This measurement represents the estimate of the mixing matrix $\hat{A}$, which is denoted as the pseudo-inverse of the demixing matrix (that is, W^{+}). The pairwise distance of these topographic patterns can give us information how close the spatial distributions of these sources are. In our study we used the correlation method to calculate this distance,

$$\text{dtopo} = 1 - \frac{(\text{Topo}_c - \overline{\text{Topo}_c})(\text{Topo}_t - \overline{\text{Topo}_t})'}{\sqrt{(\text{Topo}_c - \overline{\text{Topo}_c})(\text{Topo}_c - \overline{\text{Topo}_c})' \times (\text{Topo}_t - \overline{\text{Topo}_t})(\text{Topo}_t - \overline{\text{Topo}_t})'}} \tag{5}$$

where Topo_c was the topographic pattern of the compared IC and Topo_t was the topographic pattern of the template IC. If this value is close to zero then the topographic pattern of the current IC is a close match to that of the template IC, which represents a certain type of artifacts. In this study we used the built-in *pdist.m* function in statistical toolbox v4.0 and MATLAB 6.5 (The Math Works Inc., MA, USA) to compute dtopo. Note that because the exact polarity of the components separated by ICA is unknown, and because eye movement-related IC's of opposite polarity had slightly different reversing projection patterns to each other, we allowed for two different templates rather than use the absolute value of the fraction above (Eq. (5)) to increase the sensitivity of the proposed method.

2.3.2. Entropy of the IC activation

The entropy of the IC was defined as:

$$H = -\sum_{t=1}^{T} p(\hat{s}(t) = y) \log(p(\hat{s}(t) = y)) \quad (6)$$

where $p(\hat{s}(t) = y)$ was the probability density of observing the activity value y in IC activation $\hat{s}(t)$. Higher entropy values corresponded to more 'random' source activities. ICs with lower entropy than other ICs can be viewed as artifactual ICs with characteristic probability densities (Barbati et al., 2004).

2.3.3. Kurtosis of the activation

The global kurtosis coefficient of one IC was calculated as

$$K = d_4 - 3 \times (d_2^2) \quad (7)$$

where $d_n = E\{(\hat{s}(t) - d_1)^n\}$ was the nth central moment of the IC component activity, and E, or the mean, was the expectancy function. With this equation, ICs with $K = 0$ represented components with Gaussian distributed activations. ICs with much higher kurtosis values than the average were viewed as artifacts which have supra-Gaussian distributed activities. Here we used the built-in *kurt.m* function provided by the EEGLAB software package (Delorme and Makeig, 2004).

2.3.4. Correlation between power spectral densities

We used the built-in *pmtm.m* function of signal processing toolbox v6.0 and MATLAB 6.5 to compute the power spectral density (PSD) of the IC activities with multi-taper spheroidal methods (nw = 3.5, which corresponded to the use of seven discrete prolate spheroidal sequences as data tapers for the multi-taper estimation method). The sampling frequency was 1000 Hz, and the window size of the fast Fourier transform (fft) was 512. Their distances to the chosen template PSD were computed with the same equation used in the computation of topographic pattern distances with substitution of topographic pattern vectors with power spectral pattern vectors. The higher the correlation between IC power spectrums the lower their pairwise distance, which means the IC's PSD represents a close match to the template.

2.4. Categorization of ICs with ART-2 network

Another method we used to identify artifactual ICs consisted of applying the analog adaptive resonance theory (so-called ART-2) neural network to categorize IC features. ART networks are self-organizing, dynamic neural networks that recognize patterns with stable structures (Carpenter and Grossberg, 1987a). The two-layer ART-2 network architecture and equations, as originally proposed by Carpenter and Grossberg (1987b), are reproduced with permission in Appendix A for the convenience of the reader. The inputs to the network were vectors composed of four normalized feature values of each IC in the order of [dtopo dPxx H K]. dtopo and dPxx values ranged from 0 to 2 and represented the outcome of the correlation-based distance metric described above. H values were normalized between 0 and 1 based on the minimum and maximum H values in each dataset. Normalized K values were obtained by dividing the computed global kurtosis coefficient by 50, which was arbitrarily selected based on experience. The ART-2 output consisted of two nodes or categories [target IC artifact, IC non-artifact]. Categorization results were analyzed after the ART-2 system had stabilized for a given pattern mismatch threshold ρ (so-called the 'vigilance' parameter by Carpenter & Grossberg). All other parameters in the ART-2 network were set as in the original publication and no parameter optimization was performed (see Appendix A for the model parameters).

2.5. Artifact identification and updating of the templates

All datasets were processed with the proposed artifact identification and removal procedures. As illustrated in Fig. 2, four feature attributes {dtopo, dPxx, H, K} were extracted from the ICs. The initial artifact template was chosen based on topographic and/or activation patterns previously characterized as certain type of artifacts (e.g., eye movement) in former studies (Tang et al., 2002; Vigario et al., 2000). Artifactual ICs have been identified through iterations with threshold-based clustering, neural network categorization or the combination of these two methods. After each iteration the template was updated with the average of the target artifactual ICs among the identified ICs.

2.6. Independent component datasets

We set the IC number of each trial to 157, then dataset one contained 157 ICs, dataset two contained 14,915 ICs (95 trials × 157 ICs/trial = 14,915 ICs) and dataset three contained 19,311 ICs (123 trials × 157 ICs/trial = 19,311 ICs). For dataset four, there were 157 ICs for the concatenated ICA analysis, and 3297 ICs (21 trials × 157 ICs/trial = 3297 ICs) for the ICA analysis on single-trial based epochs. Artifactual IC templates related to two types of ocular movements (EOG1 and EOG2), heart beat (EKG) and muscle activity were found in the datasets (Fig. 7). Three types of components related to muscle activity were displayed. EKG, EOG1 and EOG2 IC templates were applied in artifactual IC identification. Both identification procedures were employed for all four datasets. For dataset one and four, the results were calculated with one repetition of the identification loop, whereas for datasets two and three, this loop was iterated three times with template updating after each round. Further steps of removing the artifacts and reconstructing the cleaned MEG signal were performed on single trial basis for all four datasets.

2.7. Evaluation of performance

2.7.1. Comparison of performance between threshold-based clustering methods and ART-2 categorization neural network

We then compared the performance of the two methods in identifying the artifactual ICs. We picked dataset three for this purpose since dataset three contained MEG signal from all subjects, which was closer to most of the empirical conditions

than dataset one and dataset two. The artifactual ICs were identified with template EKG and EOG1 since they were the most prominent artifactual ICs found in the datasets. We applied both methods with three iterations. For the ART-2 categorization neural network, we used five vigilance levels (0.95, 0.96, 0.97, 0.98 and 0.99). The criteria for the threshold-based clustering method were the same as described in Section 2.3 for the corresponding type of artifactual ICs. The target artifactual ICs among the identified ICs were selected via visual inspection. The number of identified ICs and selected target artifactual ICs were

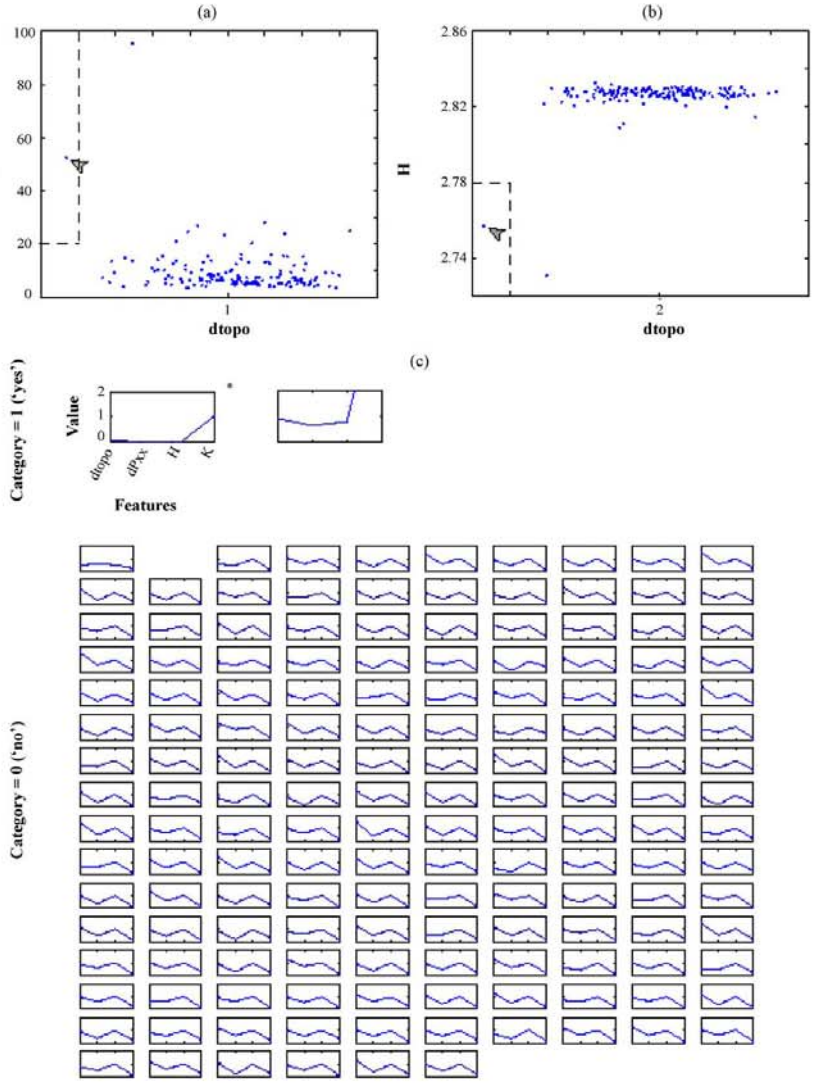

Fig. 3. Threshold-based clustering of ICs for artifactual IC identification of single trial MEG signals. (a) The identification of the IC related to EOG1 artifact with threshold-based clustering method (indicated by arrowhead), feature values of dtopo and *K* were displayed. (b) The identification of the IC related to EKG artifact with threshold-based clustering method (indicated by arrowhead), feature values of dtopo and *H* were displayed. The threshold criteria for clustering were indicated with gray dash lines. (c) The categorization of the ICs with ART-2 network. The inputs to the network were the vectors composed of four normalized feature values of each IC. The IC feature values of dtopo and dPxx (see text for the description of the calculation) were calculated from template related to EOG1 artifactual ICs. The ICs were categorized into 'yes' and 'no' groups. 'Yes' group contained ICs identified as EOG1 artifacts, 'no' group contained ICs identified as non-EOG1. Two ICs were identified as EOG1 artifactual ICs with the network method, while only one was target EOG1 artifactual IC. The target IC was selected via visual inspection and was labeled with (*).

counted. The correctness of the identification was calculated as the proportion of target artifactual ICs in the identified ICs.

$$\text{Correctness} = \frac{\text{Number of target ICs}}{\text{Number of identified ICs}} \times 100\% \quad (8)$$

The number of identified ICs and the correctness of identification are plotted in Fig. 9 to compare the performance between the methods. The performance of ART-2 categorization neural network was displayed with five vigilance levels.

2.7.2. Comparison of performance on continuous data and single-trial based epochs

We applied ICA and artifactual IC identification methods on dataset four to compare the performance between the ICA

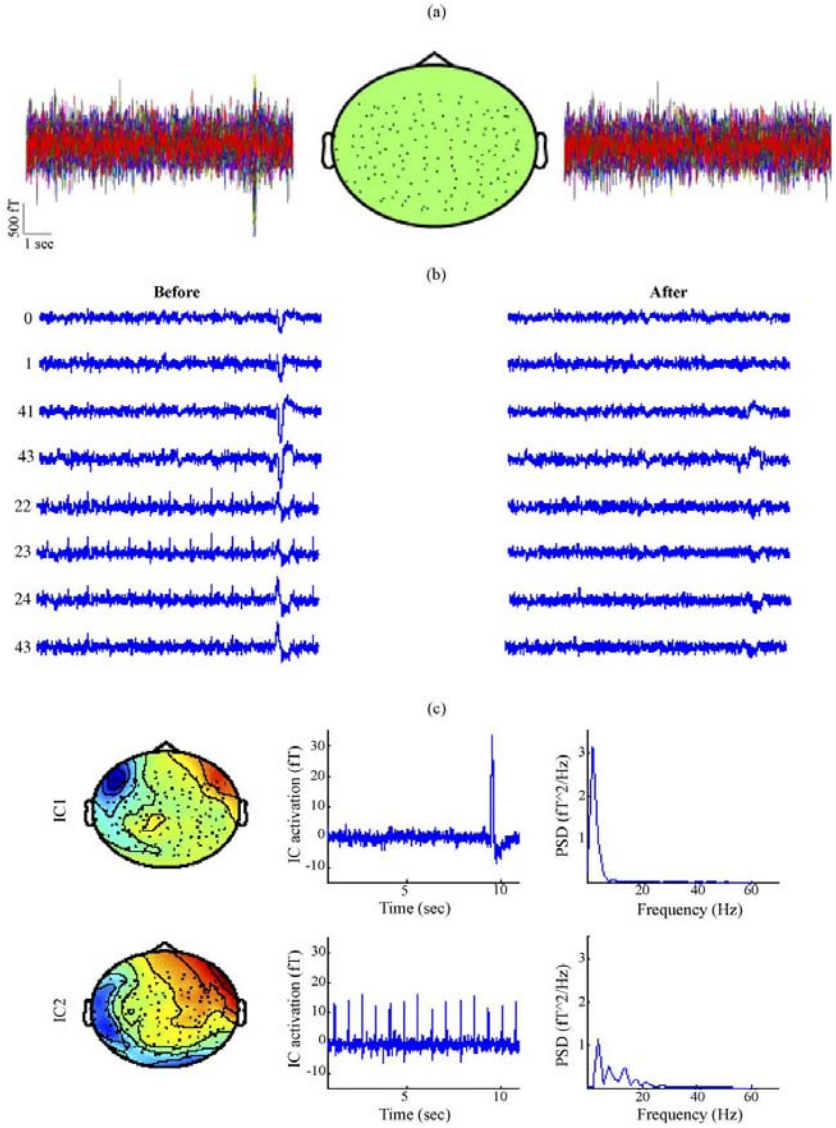

Fig. 4. Single trial artifactual component identification and rejection. (a) Whole channel noise-reduced raw MEG signal (left); 2D top view of channel position (center), and whole channel artifact-cleaned MEG signal (right). (b) Bilateral frontal channel recording before removing artifactual components (left panel), and MEG signals on same channels after rejection of artifactual components (right panel). The scales are the same as in (a). (c) The components found in this trial. (Upper) topographic pattern, activity and power spectrum of the component identified as EOG1; (lower) component identified related to heart beat (EKG).

analysis of the continuous (concatenated) MEG signals and the single-trial based epochs. The concatenated dataset contained 21 trials of MEG signals since it was the highest amount of continuous data our data analysis workstation (Gateway 6100 series with 3.20 GHz CPU and 1.0 GB RAM) could process using ICA without memory problems. Percentage of variance accounted for (pvaf) of the ICs for each sensor were calculated for each trial.

$$\text{pvaf} = \frac{\text{Var}(x(t) - x'(t))}{\text{Var}(x(t))} \quad (9)$$

where $x(t)$ and $x'(t)$ had the same mathematical denotation to the ones in Eqs. (1) and (4). Var () operation was to compute the sample variance of the signal.

The 10 sensors with the highest absolute values in the topographic component of the target artifactual IC templates were selected as the most influenced sensors, while the 10 sensors with lowest absolute values were selected as the least influenced sensors. The pvaf values calculated on most influenced sensors and least influenced sensors were statistically analyzed with repeated measures ANOVA. The mean pvaf values between ICA on concatenated signal and single-trial epochs were pair-wisely compared. Significant differences were the comparisons with probability value $p < 0.05$. The statistical analyses were performed with SAS v9.1 (SAS Institute Inc., Cary, NC, USA.).

2.7.3. *Evaluation of overestimation and underestimation of identification methods*

With dataset four, EKG, EOG1 and EOG2 artifactual ICs were identified with the ART-2 categorization neural network, higher threshold-based clustering, lower threshold-based clustering, and the combined method involving the neural network categorization on the ICs which have been identified with higher threshold-based clustering method. These identification methods were applied on both concatenated data and single-trial epochs. Numbers of target artifactual ICs in identified ICs were visually examined. Underestimation was evaluated with a measurement of coverage, which was computed as the ratio of the number of target artifactual ICs within the identified ICs divided by the number of target ICs in the dataset; if coverage value was less than 100%, this type of artifactual ICs was underestimated

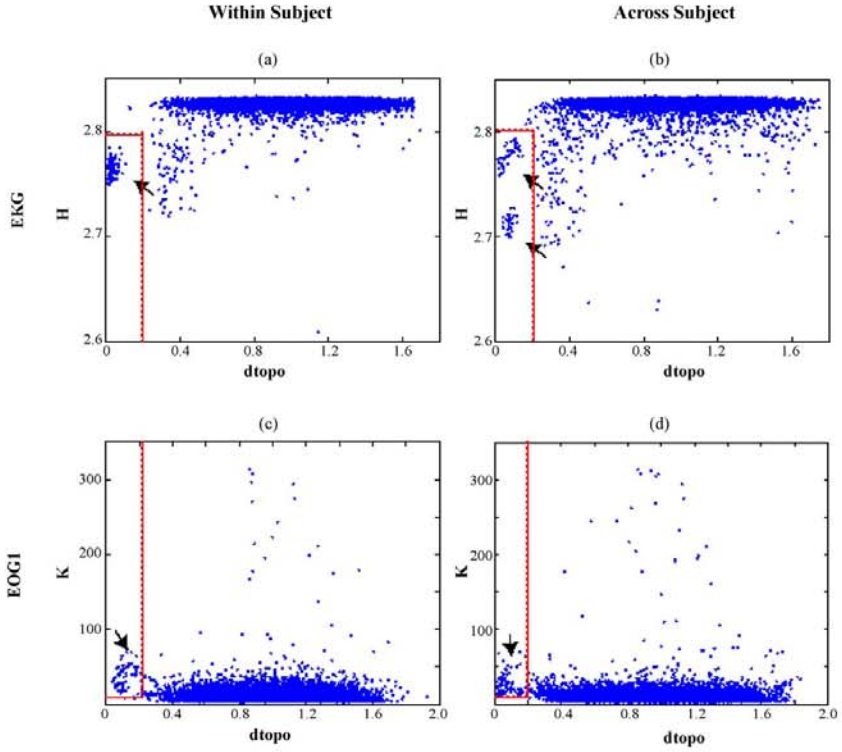

Fig. 5. Threshold-based clustering of artifactual ICs across multiple trials, the threshold criterion for clustering was indicated with red dash lines, the clustered ICs were labeled with arrowheads. (a) Clustering of EKG-related artifactual ICs in dataset two, dtopo and H values were displayed. (b) Clustering of EKG-related artifactual ICs in dataset three, dtopo and H values were displayed. (c) Clustering of EOG1-related artifactual ICs in dataset two, dtopo and K values were displayed. (d) Clustering of EOG1-related artifactual ICs in dataset three, dtopo and K values were displayed.

with this method. Overestimation was evaluated with measurement of correctness, which was computed using Eq. (8). If the percentage correctness value was less than 100%, then this type of artifactual ICs was overestimated with this method.

3. Results

3.1. Identification of artifacts and effect of removal in single trials

In general, scalp map distances (dtopo) and global kurtosis coefficients (K) were adequate for discriminating EOG artifacts, whereas scalp map distances and entropy (H) values were sufficient in identifying EKG artifacts. For dataset one, threshold-based clustering methods successfully identified components related to EKG and EOG1, as displayed in scatter plot of dtopo versus H and in scatter plot of dtopo versus K (Fig. 3(a) and (b)), in which gray dash lines indicated the threshold used for clustering. No EOG2 artifactual IC was identified in dataset one.

Fig. 3(c) shows the inputs to ART-2 network for identification of type 1 EOG (EOG1) artifactual ICs and the identification results. Two ICs were identified as EOG1 artifacts—one more than EOG1 ICs identified through threshold-based clustering process. The same IC identified through network method and threshold-based clustering method were labeled with *. The vigilance level of the reset system in the ART-2 network was set to 0.96.

Fig. 4(a) depicts the whole-channel pre-whitened MEG signals before and after artifact removal (left and right panels, respectively), and the 2D view of the sensor positions (center panel). Fig. 4(b) shows the bilateral frontal channel recordings with synchronous activity caused by eye movement and heart beat related artifactual components. Comparison between the MEG signal before and after removal of the artifactual components demonstrated successful decontamination of the MEG signals by removing the identified artifactual ICs. The scalp map pattern, activity and power spectral density of the artifactual ICs identified in this trial are shown in Fig. 4(c). These artifactual ICs are consistent with the artifactual components identified in former studies (Vigario et al., 2000).

3.2. Identification of artifacts in multiple trials

Fig. 5 shows threshold-based clustering of the ICs for the multiple trial datasets after three iterations. Red dash lines indicate the threshold used for clustering. Fig. 5(a) and (c) are scatter plots of EKG and EOG1 feature values for dataset two (within subjects); Fig. 5(b) and (d) correspond to scatter plots for dataset three (across subjects). For EKGs, the features displayed are dtopo and H. For EOG1s, the features displayed are dtopo and K. Clusters marked with arrows were selected, and corresponding ICs were removed on a single trial basis. We also compared mean values of the IC features between the identified ICs and the un-identified ICs with Kruskal–Wallis non-parametric statistical analyses. Both dtopo ($\chi^2 = 307.33$, $p < 0.001$), and K value ($\chi^2 = 251.23$, $p < 0.001$) between EOG1 and non-EOG1 ICs, and dtopo ($\chi^2 = 274.32$, $p < 0.001$), and H value ($\chi^2 = 277.24$,

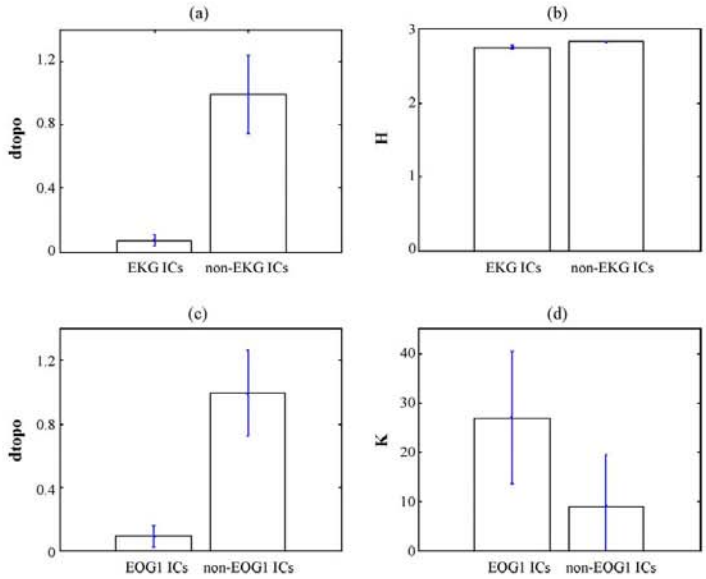

Fig. 6. Comparison of feature values between artifactual ICs and non-artifactual ICs, independent components were categorized from dataset three. (a) Comparison of dtopo values between EKG-related ICs and non-EKG ICs. (b) Comparison of H values between EKG-related ICs and non-EKG ICs. (c) Comparison of dtopo values between EOG1-related ICs and non-EOG1 ICs. (d) Comparison of K values between EOG1-related ICs and non-EOG1 ICs.

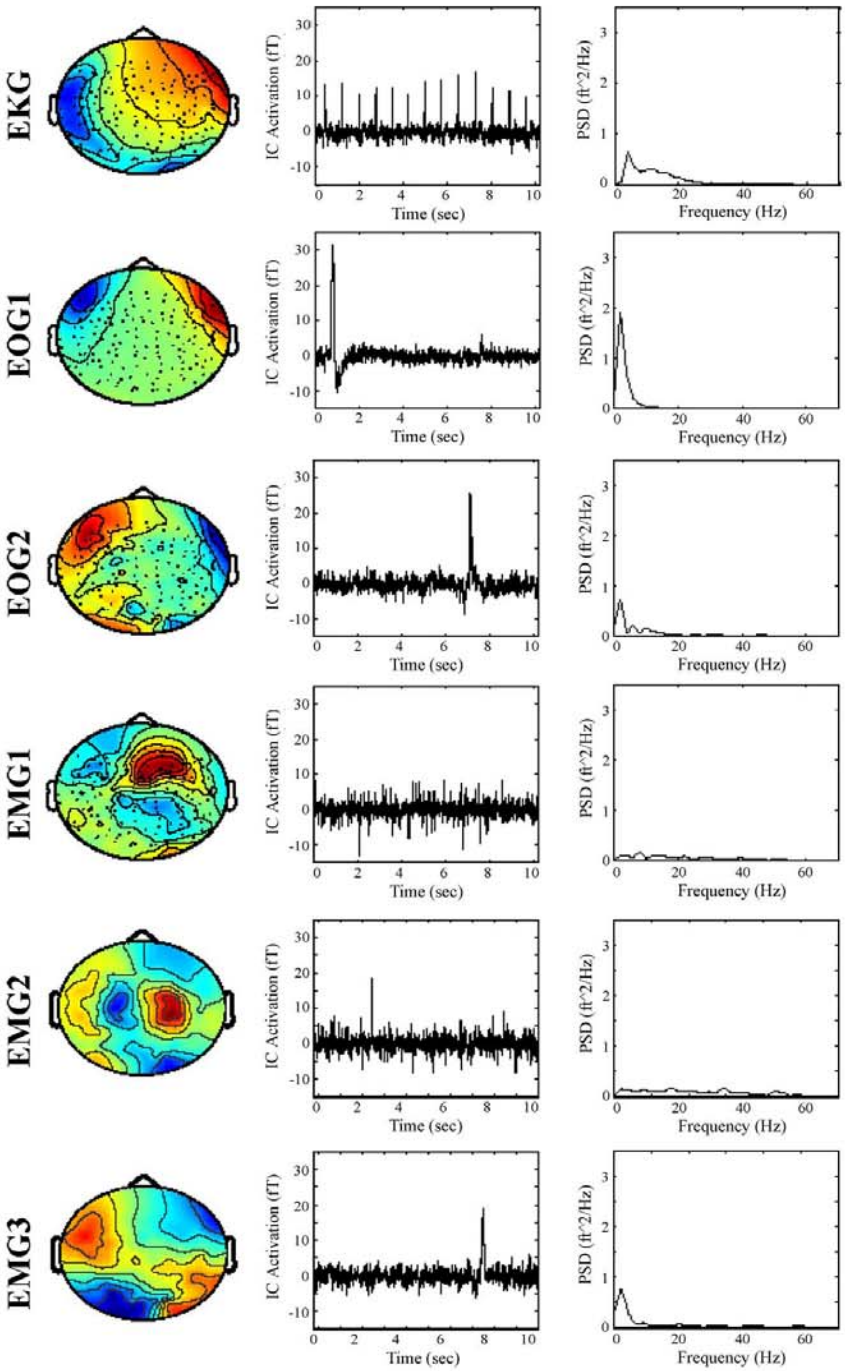

Fig. 7. The artifactual IC templates. Left column: topographic patterns of IC templates; center column: activations of IC templates; right column: power spectral patterns of IC templates. First row: the features of the template IC related to EKG; second row: features of template IC related to EOG1; third row: features of template IC related to EOG2; fourth row to sixth row: features of template ICs related to three instances of muscle activities.

$p < 0.001$) between EKG and non-EKG ICs showed statistically significant differences (Fig. 6).

3.3. The artifactual IC templates and update

Fig. 7 depicts the initial templates for the artifactual IC scalp maps (left panel), activations (center panel) and power spectral density plots (right panel). The six templates represent the artifactual ICs related to EKG, EOG1, EOG2 and three instances of muscle activities, respectively. EKG template IC showed the characteristic activation pattern. EOG1 and EOG2 template ICs represented the types of eye movements with opposite direction of electric sources. The three muscle activity-related IC templates were selected with the similar topographic patterns as the ones showed in a former study (Vigario et al., 2000) and with the characteristic bursting pattern in IC activations. Fig. 8 shows the comparison between the initial template and the final identified IC features in the identification of EKG artifactual ICs with dataset two. The similarity between the initial template topographic pattern and the mean topographic pattern of identified ICs indicated the closeness of the identified EKG ICs. The similarity of the characteristics between same types of ICs also can be seen in the power spectral patterns. The typical 4 and 8 Hz peaks in EKG ICs are clearly seen in the averaged EKG IC power spectrum.

3.4. Performance of identification methods

As shown in Fig. 9, the threshold-based clustering method identified more ICs and showed higher correctness than the ART-2 network categorization method although the threshold-based clustering method for EOG1 artifactual ICs did not reach 100% correctness. As expected, different vigilance levels showed different performance levels, so that increasing the vigilance level resulted in an increased number of identified ICs. However, the correctness of identification decreased when $\rho > 0.97$.

3.5. Continuous signal versus single-trial based identification

Table 1 and Fig. 10 illustrate the identification and clustering of artifactual ICs in dataset 4. The scatter plots in Fig. 10 illustrate the ICs in feature space constructed with the two features with the highest discriminatory power for the target artifactual ICs.

As shown in Table 1 and Fig. 10(a) and (c), two EKG and two EOG1 artifactual ICs were identified within 157 ICs when applying ICA on the concatenated MEG signal. EOG2 artifactual ICs were not found in these 157 ICs (Fig. 10 (e)), so we only compared pvaf (percentage variance accounted for) values for the identified EKG and EOG1 artifactual ICs (Table 2).

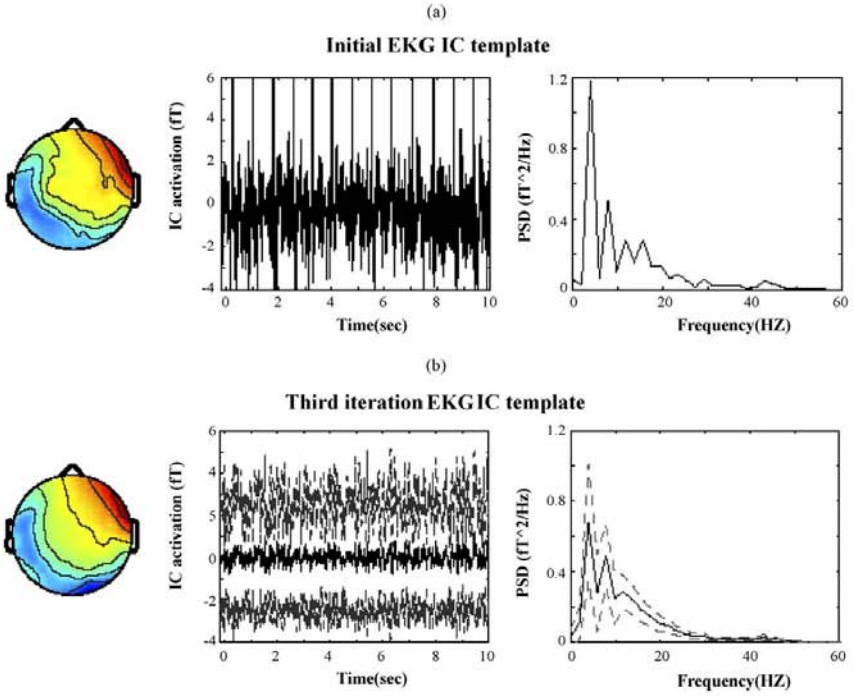

Fig. 8. The illustration of iterative identification processes of artifactual ICs. (a) The initial template of EKG-related IC for identification of EKG in dataset two. Topographic pattern, activation and power spectral pattern of the template IC were showed. (b) The identification results after three iterations. Left: mean topographic pattern of identified ICs; center: mean activation and 95% confidence interval (light gray dash lines) of identified ICs, and; right: mean power spectrum and 95% confidence interval (light gray dash lines) of identified ICs.

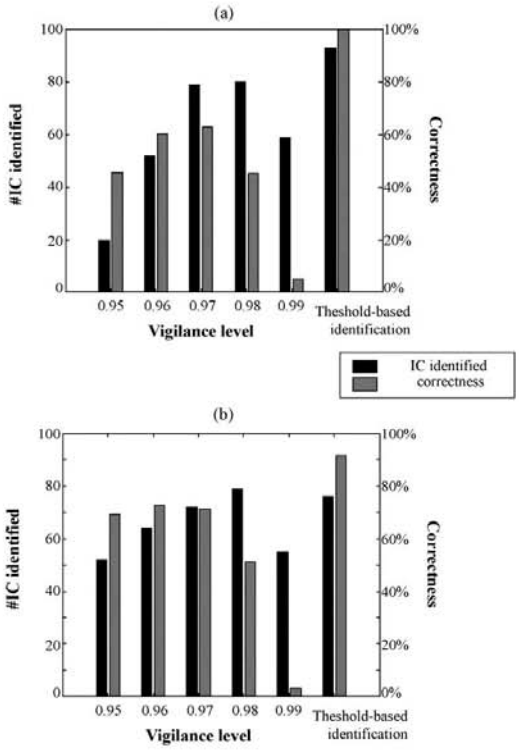

Fig. 9. Performance evaluation of artifactual IC identification with ART-2 network and threshold-based clustering. Data from dataset two. Vigilance levels used in ART-2 network were 0.95–0.99. (a) Identification of EKG-related ICs. Left *y*-axis indicates the number of IC identified with each method as indicated in *x*-axis, right *y*-axis indicates the correctness values. (b) Identification of EOG1-related ICs.

Fig. 11(a) and (b) shows the 2D projection (location) of the least (denoted by the filled dots) and the most (denoted by the white dots) influenced sensors. As shown in Fig. 11(c) and (d), for the most influenced sensors, the mean pvaf values of the identified artifactual ICs for the ICA processing of single-trial based epochs were similar to the identified artifactual ICs using ICA on the concatenated MEG signals (see Table 2). For the least influenced sensors, the mean pvaf values of the identified artifactual ICs from the single-trial based epochs were significantly smaller statistically for the EKG ICs ($p < .01$; Table 2). No statistically significant difference was found for EOG1 ICs in the least influenced sensors.

3.6. Overestimation and underestimation in identification of artifactual ICs.

Table 1 shows the evaluation of overestimation and underestimation of the identification methods. The results were computed from dataset four. For EKG ICs, the higher threshold-based clustering method performed best for the concatenated ICA procedure (coverage = 100%, correctness = 100%), whereas the lower threshold-based clustering method performed best for the single-trial based epochs (coverage = 100%, correctness = 100%). Applying the ART-2 neural network categorization on ICs identified by the higher threshold-based clustering method alleviated the overestimation caused by the lower clustering threshold with slight underestimation of the EKG-related ICs computed from single-trial based epochs.

For EOG1 and EOG2 ICs, both coverage and correctness performance based on the neural network categorization were not as good as those seen in the threshold-based clustering method. The higher threshold-based method captured all artifactual ICs at expense of correctness because of the broader threshold criteria used, whereas the lower threshold-based method achieved 100% correctness, but the coverage was low. Applying the ART-2 method on the ICs identified with the higher threshold-based method increased the correctness ratio.

No EOG2 ICs were identified or visually found in ICs computed from the concatenated MEG signal. However, for the single-trial based epoch IC dataset, seven EOG2 ICs were identified. The lower threshold-based clustering method has identified only one IC among the seven ICs, whereas the neural network categorization identified six of them with very low correctness. The higher threshold-based clustering method identified all seven ICs with less than 50% correctness. Applying network categorization on ICs identified with the higher threshold-based clustering method increased correctness to 54%.

4. Discussion

In this paper we proposed a method for artifact identification and removal in MEG signals based on independent component analysis and clustering methods. The procedure consisted of four iterated consecutive steps: (1) ICA computation, (2) calculation of IC features, (3) identification of artifact ICs with iterative procedures and template updating, and (4) removal of artifactual ICs and reconstruction of artifact-cleaned MEG signals.

In this study we tested two IC identification methods. Both methods identified the artifactual ICs based on feature values computed from the scalp map, power spectral density, kurtosis and entropy. The threshold-based clustering method showed effective identification and higher accuracy; whereas the automatic ART-2 network categorization method had the highest identification rates and correctness at vigilance level of 0.97. Combination of these two methods increased the accuracy of identification with no or very small decrease of coverage for target artifactual ICs. To our knowledge, this is the first attempt to use an ART-2 categorization neural network in artifact identification and automatic removal for MEG signals.

For artifactual IC identification and removal, both overestimation and underestimation should be avoided since overestimation may cause data loss related to non-artifactual sources, where underestimation may cause insufficient removal of artifacts in the MEG signals. We evaluated the performance of each method using measurements of coverage and correctness of identification. The results showed that for EKG ICs, the threshold-based method was better in avoiding both overestimation and underestimation. This may be because of the amount of information

Table 1
Evaluation of performance—over estimation and underestimation

	ICA processes	Methods[a]	Parameters[b]	Number of artifactual ICs in dataset	Number of ICs identified	Number of target artifactual ICs among identified ICs	Coverage (%)	Correctness (%)
EKG	CAT[c]	nw	0.97	2	2	1	50.00	50.00
		Ltb	[0.4 0.5 0 2.84]	2	1	1	00.00	100.00
		Htb	[0.8 0.5 0 2.84]	2	2	2	100.00	100.00
		comb	nw + Htb	2	2	2	100.00	100.00
	EPOCH	nw	0.97	21	37	18	85.71	48.65
		Ltb	[0.2 0.5 0 2.8]	21	21	21	100.00	100.00
		Htb	[0.4 0.5 0 2.84]	21	35	21	100.00	60.00
		comb	nw + Htb	21	21	18	85.71	85.71
EOG1	CAT	nw	0.97	2	3	1	50.00	33.33
		Ltb	[0.5 0.5 10 2.84]	2	2	2	100.00	100.00
		Htb	[0.8 0.5 10 2.84]	2	2	2	100.00	100.00
		comb	nw + Htb	2	2	2	100.00	100.00
	EPOCH	nw	0.97	19	48	16	84.21	33.33
		Ltb	[0.2 0.5 10 3.0]	19	7	7	36.84	100.00
		Htb	[0.5 0.5 10 3.0]	19	23	19	100.00	82.61
		comb	nw + Htb	19	21	18	94.74	85.71
EOG2	CAT[d]	nw	0.97	0	3	0	n/a	n/a
		Ltb	[0.5 0.5 10 3.0]	0	0	0	n/a	n/a
		Htb	[0.8 0.5 10 3.0]	0	0	0	n/a	n/a
		comb	nw + Htb	0	n/a	n/a	n/a	n/a
	EPOCH	nw	0.97	7	51	6	85.71	11.76
		Ltb	[0.2 0.5 10 3.0]	7	1	1	14.29	100.00
		Htb	[0.5 0.5 10 3.0]	7	15	7	100.00	46.67
		comb	nw + Htb	7	13	7	100.00	53.85

[a] Methods: nw, ART-2 categorization neural network; Ltb, lower threshold-based clustering; Htb, higher threshold-based clustering; nw + Htb, ICs were identified with Htb method first, the identified ICs were then processed again with neural network method.

[b] Parameters: the parameters for nw method were the vigilance levels. The parameters for threshold-based clustering methods were vectors composed of threshold values, the values were $[T_{\mathrm{dtopo}}\ T_{\mathrm{dPxx}}\ T_K\ T_H]$. The identification criteria were dtopo $\leq T_{\mathrm{dtopo}}$, dPxx $\leq T_{\mathrm{dPxx}}$, $H \leq T_H$ and $K > T_K$.

[c] ICA process: CAT, MEG signal was concatenated from 21 trials, 157 ICs were computed from whole dataset; EPOCH, ICs were computed on single trial basis, each trial has 157 ICs.

[d] Since no EOG2 ICs were identified from CAT IC dataset, coverage and correctness values have not been computed. Hence, no evaluation of overestimation and underestimation was performed on this dataset.

carried in EKG ICs, which can be separated from other ICs by selecting an appropriate threshold. This effect has been demonstrated in Fig. 3(b) and Fig. 5(a) and (b). For EOG1 and EOG2 ICs, the threshold-based methods performed better than the neural network, albeit with imperfect performance—the higher threshold-based method demonstrated overestimation of the artifactual ICs whereas the lower threshold-based method demonstrated underestimation of the artifactual ICs. Combination of these two methods with the ART-2 method on ICs identified by higher threshold-based method alleviated the overestimation while keeping the benefit of coverage; the only exception was the failure to identify one of the EOG1 ICs. As a conclusion, the combined method appears to be the best approach showing higher accuracy and automatization.

Table 2
Evaluation of performance—ICA on continuous MEG signal (CAT) vs. ICA on single-trial epochs (EPOCH)

	ICA process[a]	Most influenced sensors[b]				Least influenced sensors[b]			
		Mean pvaf	S.E.M.[c]	F value	Probability	Mean pvaf	S.E.M.	F value	Probability
EKG	CAT	18.6	3.98	0.1	$p > 0.05$	2.9	0.64	8.42	$p < 0.01$
	EPOCH	16.8	3.98			0.2	0.64		
EOG1	CAT	10.1	2.26	0.87	$p > 0.05$	1.1	0.35	1.53	$p > 0.05$
	EPOCH	7.1	2.26			0.4	0.35		

[a] ICA process: CAT, MEG signal was concatenated from 21 trials, 157 ICs were computed from whole dataset; EPOCH, ICs were computed on single trial basis, each trial has 157 ICs.

[b] Sensors were grouped as most influenced sensors and least influenced sensors. Most influenced sensors were the sensors with highest absolute values in the remixing vectors of the target artifactual IC templates. Least influenced sensors were the sensors with lowest absolute values in the remixing vectors of the target artifactual IC templates.

[c] S.E.M.: standard error of means.

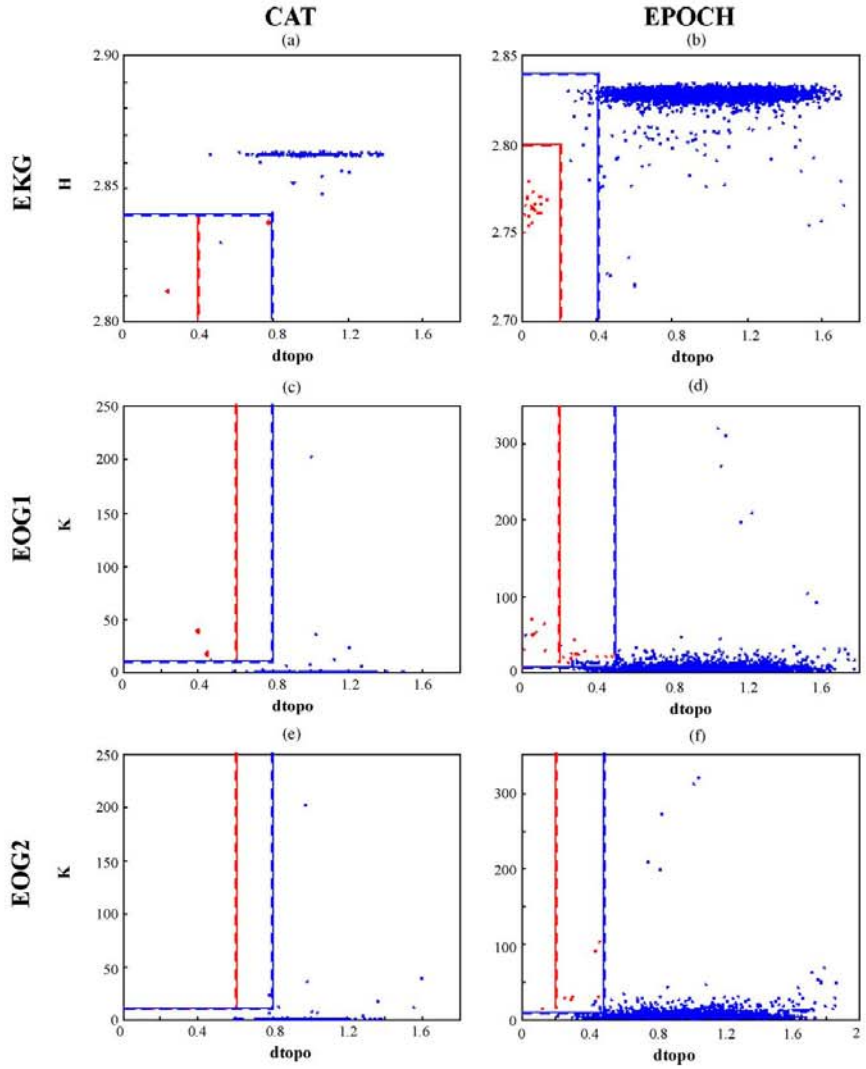

Fig. 10. Threshold-based clustering of artifactual ICs in dataset 4. The threshold criteria for clustering were indicated with red dash lines (lower threshold-based clustering) and blue dash lines (higher threshold-based clustering), which corresponded to the values shown in Table 3. The target artifactual ICs within the clusters were indicated with red dots. Subplots (a), (c) and (e) were scatter plots of the ICs computed from concatenated MEG signals; subplots (b), (d) and (f) were scatter plots of the ICs computed from single trial based epochs. Subplots (a) and (b) illustrate the clustering of EKG-related artifactual ICs in dtopo-*H* space, subplots (c) and (d) illustrate the clustering of EOG1-related artifactual ICs, and subplots (e) and (f) illustrate the clustering of EOG2-related artifactual ICs in dtopo-*K* space.

One issue regarding the application of ICA to blindly separate sources is whether it is appropriate to apply ICA on continuous (concatenated) data rather than on single-trial based epochs. To address this issue, we tested the percentage of variance accounted for (pvaf) by the identified ICs using concatenated data or epochs with 10,201 samples per sensor per trial. The significantly higher pvaf values of the least influenced sensors of EKG ICs indicated that the ICs computed with concatenated ICA contained information from other events which had been mixed with the heart beats since only 157 ICs had been computed with this dataset. As a comparison, applying ICA on single-trial based epochs produced 157 ICs for each epoch, which made separation of the sources relatively easier. Moreover, no EOG2 ICs was identified from the ICs extracted from the concatenated ICA processing, though seven EOG2 ICs have been identified with single-trial based epochs (as demonstrated

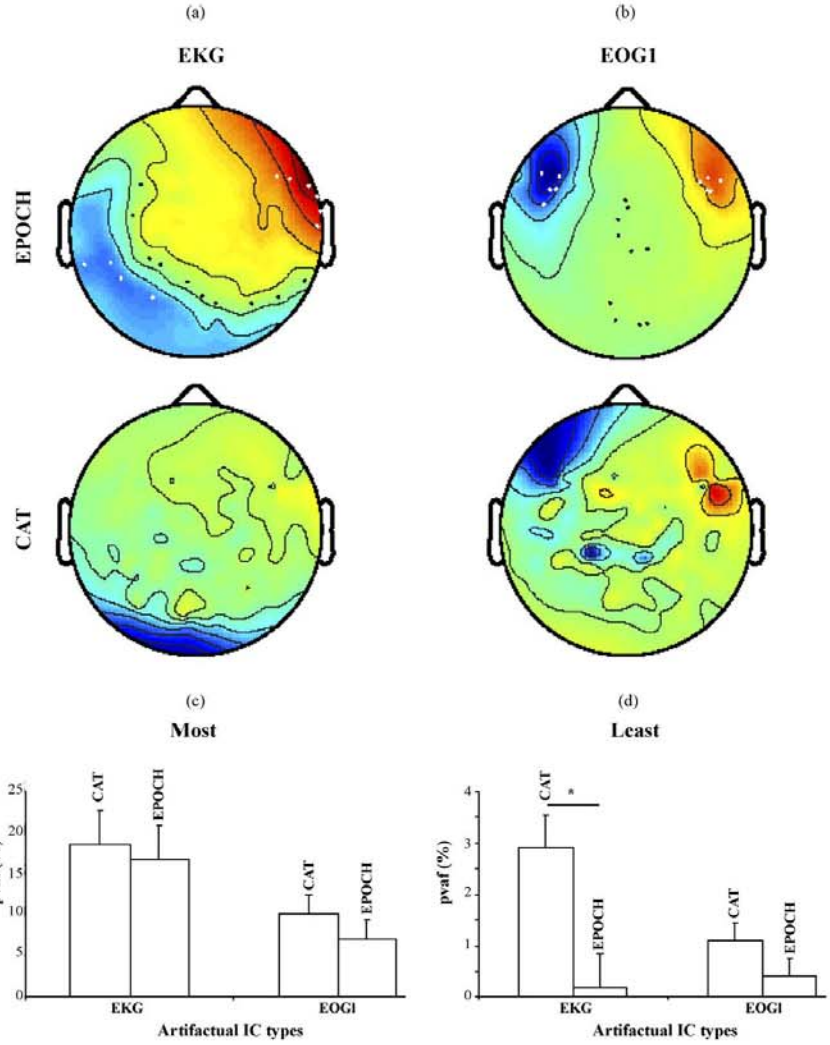

Fig. 11. Comparison of artifactual IC identification and rejection between concatenated vs. single-trial epochs ICA processing. (a) Topographic patterns of EKG-related ICs computed from concatenated MEG signal (CAT) and single-trial based epochs (EPOCH). In EPOCH pattern, sensors selected to compare pvaf values were labeled, with white circles indicating the most influenced sensors, and black circles representing the least influenced sensors. (b) Topographic patterns of EOG1-related ICs and demonstration of the sensors selected to compare pvaf values. (c) Pair-wise comparison of pvaf values on most influenced sensors (most). Height of bars indicated the mean pvaf values of identified target artifactual ICs. Error bars are standard error of means (S.E.M.). (d) Pair-wise comparison of pvaf values on least influenced sensors. (*) Indicates a statistically significant difference with $p < 0.05$.

in Table 2). Thus, we would like to argue that this epoch-based IC identification method works better than the concatenated approach provided there is enough number of data points (samples).

ICA has been shown to be an efficient tool for separating artifactual sources from functional brain signals (Jung et al., 2000) as well as to identify functional sources underlying similar neuronal mechanisms (Contreras-Vidal and Kerick, 2004; Makeig et al., 1999; Makeig et al., 2002; for review, see Delorme and Makeig, 2004) in EEG/MEG signal processing. As compared to segment-rejection methods, artifactual IC identification and rejection can save functional information from mass data loss as well as discover the functional brain activities masked by artifactual signals. Artifactual IC identification and rejection with computation of the features has been proved in this study to be less time and labor consuming for analysis of MEG signals, especially for datasets contained multiple subjects and multiple trials.

In this paper, we have combined typical components features to describe each IC, which have been used separately and emphasized individually in prior studies (Barbati et al., 2004; Delorme and Makeig, 2004). We also used data-driven clustering and categorization methods to identify the artifactual ICs. The results for single trial and multiple trials datasets confirmed that this approach can correctly identify the artifactual ICs efficiently while the best performance was obtained from combination of these two methods. However, the use of independent components rises the question of what their functional significance may be, that is, what is their functional relationship to the brain activities. Although prior ICA studies have shown ICs related to certain types of artifacts or event-related brain dynamics (Vigario et al., 2000), it is still a matter of debate whether independent components with small differences (e.g., from trial to trial or across subjects) in spatial and spectral features represent the same type of biological events. An important finding in the present study is that artifactual ICs have feature values close to each other albeit the variability displayed across subjects and trials (Fig. 6(b) and (d); see Fig. 7 for statistical analysis). The successful identification with template updating also proves that it is possible to describe artifactual ICs using template features with small distributions. As these templates can be used as initial templates for forthcoming MEG studies, it should be possible to create and update a general database of artifact and non-artifactual component templates. Thus, this method is applicable to ICs related to functional brain activities.

Acknowledgements

The authors would like to acknowledge the diligence and insight of the anonymous reviewers who contributed significantly to the revision of this manuscript.

Appendix A. Categorization of ICs with ART-2 neural networks

Based on the Adaptive Resonance Theory developed by Carpenter and Grossberg (1987a), ART networks categorize arbitrary sequences of input patterns with self-organized stable pattern recognition architectures. Implementations have been reported including a digital (binary) system (ART-1; Carpenter and Grossberg, 1987a), a system based on fuzzy logic (fuzzy ART; Carpenter et al., 1991), a system for categorization of analog inputs (ART-2; Carpenter and Grossberg, 1987b), an implementation based on a system of ordinary differential equations capable of stand-alone running in real time (Molenaar and Raijmakers, 1997), and a fast VLSI asynchronous system (ART-1m; Serrano-Gotarredona and Linares-Barranco, 1996). In the present study, we employed the analog implementation of the ART (that is, ART-2) network to categorize the IC features (see Fig. 12). The following description of the architecture and the equations defining the ART-2 network implemented in this paper is based on the original mathematical description (their Eqs. (1)–(20)) in Carpenter and Grossberg (1987a), which are reproduced (with the author's permission) herein as an Appendix A for the convenience of the reader. The network contains two competitive, short-term memory (STM) layers F1 and F2, and two long-term memory (LTM) traces z_{ij} and z_{ji}, which denote the synaptic strength from F1 layer to F2 layer and synaptic strength from F2 layer to F1 layer, respectively. These bottom-up and top-down pathways can be seen as adaptive filters.

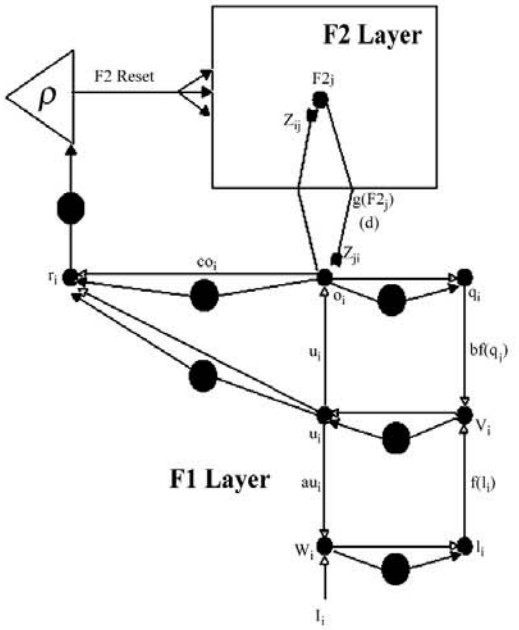

Fig. 12. A typical ART 2 architecture. Open arrows indicate specific patterned inputs to target nodes. Filled arrows indicate nonspecific gain control inputs. The gain control nuclei (large filled circles) nonspecifically inhibit target nodes in proportion to the L_2-norm of STM activity in their source fields (Eqs. (13), (14), (17), (23) and (24)). When F2 makes a choice, $g(F2_j) = d$ if the jth F2 node is active and $g(F2_j) = 0$ otherwise. (Figure and caption are adapted and reproduced with permission from Fig. 6 of Carpenter & Grossberg (1987b, p. 406).)

The F1 layer consists of six processing stages. Each stage has the same dimensionality as the input vector (I_i), which herein is composed of four feature values computed from each IC. The potential V_i, or the STM activity, of the ith node in each of the F1 layer processing stages obeys the membrane equation

$$\varepsilon \frac{\mathrm{d}}{\mathrm{d}t} V_i = -\alpha V_i + (1 - BV_i)J_i^+ - (C + DV_i)J_i^- \tag{10}$$

where J_i^+ denotes the total excitatory input, and J_i^- denotes the total inhibitory input to the ith node. ε represents the ratio between the STM membrane time constant and the LTM membrane time constant. With the constraints $0 < \varepsilon \ll 1$, $B = 0$ and $C = 0$, Eq. (10) reduced to (at steady state)

$$V_i = \frac{J_i^+}{\alpha + DJ_i^-} \tag{11}$$

in the singular form as $\varepsilon \to 0$. With Eq. (11), the STM activity of the ith node in each stage in F1 layer, represented as o_i, q_i, u_i,

v_i, l_i and w_i, becomes:

$$o_i = u_i + \sum_j g(\mathrm{F2}_j) z_{ji} \tag{12}$$

$$q_i = \frac{o_i}{e + ||\boldsymbol{o}||} \tag{13}$$

$$u_i = \frac{v_i}{e + ||\boldsymbol{v}||} \tag{14}$$

$$v_i = f(l_i) + bf(q_i) \tag{15}$$

$$w_i = I_i + au_i \tag{16}$$

$$l_i = \frac{w_i}{e + ||\boldsymbol{w}||} \tag{17}$$

where the expression $||\boldsymbol{x}||$ denotes the L2-norm of a vector $\boldsymbol{x}$; $\mathrm{F2}_j$ is the STM activity of the *jth* F2 node. Thus, z_{ji} is the weight of the projection from the *j*th F2 node to the *i*th node of the output stage O in the F1 layer. Function *f* is the piecewise linear function

$$f(\gamma) = \begin{cases} 0 & \text{if} \quad 0 \le \gamma \le \theta \\ \gamma & \text{if} \quad \gamma \ge \theta \end{cases} \tag{18}$$

where θ is the threshold.

The STM activity pattern in F2 layer represents the categorization output, which is computed in accordance with the 'winner-take-all' law based on the filtered input from the F1 layer. The total input to *j*th F2 node is calculated by

$$\mathrm{F2}_j = o_i \times z_{ij} \tag{19}$$

where o_i is the *i*th output STM activity of F1 layer, and z_{ij} is the weight of the projection from the *i*th output node of F1 layer to the *j*th node in F2 layer. The winner node in F2 layer is then identified as the node that receives the maximal input, and the other nodes are inhibited. The selection is performed through the function $g(\mathrm{F2}_j)$:

$$g(\mathrm{F2}_j) = \begin{cases} d & \text{active node} \\ 0 & \text{inactive node} \end{cases} \tag{20}$$

The top-down and bottom-up LTM trace equations defining the adaptive filters are given by

$$\frac{d}{dt} z_{ij} = g(\mathrm{F2}_j)[o_i - z_{ij}] \tag{21}$$

$$\frac{d}{dt} z_{ji} = g(\mathrm{F2}_j)[o_i - z_{ji}] \tag{22}$$

The F2 layer will be reset when a mismatch is detected (for a given vigilance parameter value) between the F1 STM pattern and an active LTM pattern. The degree of match is determined by the activity pattern in node *R* as a vector $\boldsymbol{r}$, in which the *i*th element r_i is determined by

$$r_i = \frac{u_i + co_i}{e + ||\boldsymbol{u}|| + ||c\boldsymbol{o}||} \tag{23}$$

Table 3
Parameter values used in the ART-2 network simulations

a	10
b	10
c	0.1
d	0.9
e	0
θ	0.2

A mismatch will be detected when

$$\frac{\rho}{e + ||\boldsymbol{r}||} > 1 \tag{24}$$

and the F2 layer will be reset. The vigilance parameter ρ is set between 0 and 1, and this is the only parameter that was parametrically varied in the present study. A categorization result will be accepted when both layers are stable and no mismatch has been detected. Table 3 shows the parameters of the network used in the present study.

References

Adachi Y, Shimogawara M, Haruta Y, Ochiai M. Reduction of non-periodic environmental magnetic noise in MEG measurement by continuously adjusted least squares method. IEEE Trans Appl Supercond 2001;11(1):669–72.

Barbati G, Porcaro C, Zappasodi F, Rossini PM, Tecchio F. Optimization of an independent component analysis approach for artifact identification and removal in magnetoencephalographic signals. Clin Neurophysiol 2004;115:1220–32.

Bell AJ, Sejnowski TJ. An information-maximazation approach to blind separation and blind deconvolution. Neural comput 1995;7:1129–59.

Carpenter G, Grossberg S. A massively parallel architecture for a self organizing neural pattern recognition machine. Comput Vis Graph Image Process 1987a;37:54–115.

Carpenter GA, Grossberg S. ART2: stable self-organization of category recognition codes for analog input patterns. Appl Opt 1987b;26(23):4919–30.

Carpenter G, Grossberg S, Rosen DB. Fuzzy ART: fast stable learning and categorization of analog patterns by an adaptive resonance system. Neural Netw 1991;4:759–71.

Contreras-Vidal JL, Kerick SE. Independent component analysis of dynamic brain responses during visuomotor adaptation. NeuroImage 2004;21:936–45.

Delorme A, Makeig S, Sejnowski TJ. Automatic artifact rejection for EEG data using high-order statistics and independent component analysis. In: Proceedings of the 3rd International Workshop on ICA, San Diego; 2001. p. 457–62.

Delorme A, Makeig S. EEGLAB: an open source toolbox for analysis of single-trial EEG dynamics including independent component analysis. J Neurosci Methods 2004;134:9–21.

Hämäläinen M, Hari R, Ilmoniemi R, Knuutila J, Lounasmaa OV. Magnetoencephalography—theory, instrumentation and applications to noninvasive studies of the working human brain. Rev Mod Phys 1993;65(2):413–97.

Hillyard SA, Galambos R. Eye-movement artifact in the CNV. Electroencephalogr Clin Neurophysiol 1970;28:173–82.

Jackson JD. Classical electrodynamics. 3rd ed. New York: John Wiley & Sons Inc.; 1999. p. 218–23.

James CJ, Gibson OJ. Temporally constrainted ICA: an application to artifact rejection in electromagnetic brain signal analysis. IEEE Trans Biomed Eng 2003;50(9):1108–16.

Joyce CA, Gorodnitsky IF, Kutas M. Automatic removal of eye movement and blink artifacts from EEG data using blind component separation. Psychophysiology 2004;41:313–25.

Jung TP, Humphries C, Lee TW, Makeig S, Mckeown MJ, Iragui V, Sejnowski TJ. Extended ICA removes artifacts from electroencephalographic recordings. Adv Neural Inform Process Syst 1998;10:894–900.

Jung TP, Makeig S, Humphries C, Lee TW, Mckeown MJ, Iragui V, Sejnowski TJ. Removing electroencephalographic artifacts by blind source separation. Psychophysiology 2000;37:163–78.

Kado H, Higuchi M, Shimogawara M, Haruta Y, Adachi Y, Kawai J, Ogata H, Uehara G. Magnetoencephalogram system developed in KIT. IEEE Trans Appl Supercond 1999;9(2):4057–62.

Makeig S, Bell AJ, Jung T-P, Sejnowski TJ. Independent component analysis of electroencephalographic data. In: Touretzky D, Mozer M, Hasselmo M, editors. Advances in neural information processing systems, vol. 8. Cambridge, MA: MIT Press; 1996. p. 145–51.

Makeig S, Westerfield M, Jung TP, Covington J, Townsend J, Sejnowski TJ, Courchesne E. Functionally independent components of the late positive event-related potential during visual spatial attention. J Neurosci 1999;19(7):2665–80.

Makeig S, Westerfield M, Jung TP, Enghoff S, Townsend J, Courchesne E, Sejnowski TJ. Dynamic brain sources of visual evoked responses. Science 2002;295:690–4.

Makeig S, Debener S, Onton J, Delorme A. Mining event-related brain dynamics. Trends Cogn Sci 2004;8(5):204–10.

Molenaar PC, Raijmakers ME. Exact ART: a complete implementation of an ART network. Neural Netw 1997;10(4):649–69.

Serrano-Gotarredona T, Linares-Barranco B. A real-time clustering microchip neural engine. IEEE Trans VLSI Syst 1996;4:195–209.

Tang A, Pearlmutter B, Phung D, Reeb B. Independent component of magnetoencephalography:localization. Neural Comput 2002;14:1828–57.

Vigario R, Sarela J, Jousmaki V, Hamalainen M, Oja E. Independent component approach to the analysis of EEG and MEG recordings. IEEE Trans Biomed Eng 2000;47:587–93.

Woestenburg JC, Verbaten MN, Slangen JL. The removal of the eye-movement artifact from the EEG by regression analysis in the frequency domain. Biol Psychol 1983;16:127–47.

CHAPTER 3. MODULATION OF HUMAN AUDITORY EVOKED RESPONSES INDUCED BY PERFORMING A SHORT-TERM MEMORY (STM) TASK: A MAGNETOENCEPHALOGRAPHIC (MEG) STUDY

It is well acknowledged that both bottom-up and top-down procedures exert influences on information processing in the auditory cortices (Scheich et al. 2007). Compared to the relatively stereotype bottom-up hierarchical pathways, top-down modulation by cognitive functions on the early auditory cortices show a highly dynamic and task specific pattern whose underlying neuronal mechanisms have yet to be well understood. In this study we applied a short-term memory (STM) behavioral paradigm – the delayed-match-to-sample (DMS) task – to investigate the task-specificity of the cognitive modulation of human auditory activity with the measurement of whole-head Magnetoencephalography (MEG). By comparing to the control tasks such as passive listening (PSL) and counting (CNT), we observed a significant DMS-specific suppression of the auditory evoked response (AER) to the second stimulus in a sound pair, where the peak latency of the corresponding AER was around one hundred milliseconds after stimulus onset. Analysis of the cortical sources revealed the spatial center of this effect in the vicinity of the left auditory cortex. In addition to the demonstration of this DMS-specific top-down modulation effect, analysis of coherence between current sources showed correlated enhancement of the interareal functional interactions between the auditory cortex and frontal regions in various frequency bands, which indicated involvement of multiple cognitive functions in the observed modulation effect. Therefore, our findings

suggested that in contrast to automatic adaptation to repeated sound stimuli, the STM related neural dynamics during performance of the DMS tasks modulated the perception of incoming acoustic stimuli by suppressing the task-irrelevant procedures through the functional fronto-temporal feedback pathways based upon the memorized features of the auditory objects.

3.1 Introduction

Auditory cortical responses evoked by sound stimuli are highly modulated by acoustic context (Malone et al. 2002; Barlett & Wang 2005), attention (Hillyard et al. 1973; Woldorff et al. 1993; Hughes & Jones 2003; Sabri et al. 2006) and behavioral states (Stanny & Elfner 1980; Gottlieb et al. 1989; Fritz et al. 2005). It has been shown in both anesthetized (Condon & Weinberger 1991; Ulanovsky et al. 2003) and awake (Fritz et al. 2003; Barlett & Wang 2005) animals that previous events could induce representational changes in primary auditory cortical neurons, which might be caused by either intrinsic dynamics (Fritz et al. 2003; Wehr & Zador 2005) or feedback modulation from downstream cognitive processes (Miller & Cohen 2001; Friston 2005). In human beings, the modulation effect has been shown to occur early in the evoked cortical responses, such as modulation of the N1 component in electroencephalographic (EEG) and the corresponding M100 component in magnetoencephalographic (MEG) studies (Näätänen & Picton 1987; Hillyard et al. 1973; Woldorff et al. 1993; Jääskeläinen et al. 2004; Ahveninen et al. 2006).

As one of the early EEG/MEG evoked responses with a latency of around one hundred milliseconds after stimulus onset, N1/M100 is correlated with the detection of changes in the acoustic environment (Näätänen & Picton 1987; Hari 1990). Both magnitude enhancement and suppression have been shown for the modulation effect by different studies. While the enhancement effects were mainly observed in behavioral paradigms with active manipulation of the attention to the task-related auditory domain by comparing to the conditions that directed the attention away (Hillyard et al. 1973; Woldorff et al. 1993), the suppressive modulation effect has

been observed in both passive tasks such as listening to repeated stimuli (May et al. 1999), and active tasks such as dichotic listening (Fujiwara et al. 1998; Brancucci et al. 2004), discrimination (Melara et al. 2005) and working memory paradigms (May & Tiitinen 2004; Luo et al. 2005; Lu et al. 1992). It has been proposed that the observed suppression effects result from 'repetitive suppression' as an automatic adaptation to the repeated stimuli presentations (for review, see Baldeweg 2006). However, the experimental evidence with active task performance also has shown the effect without reliance of repetitively presentation of sounds. Therefore it remains unclear whether the task-specific cognitive functions, which involve active modulation mechanisms, might also underlie some of the observed suppression effects.

Here, we used MEG to investigate the active top-down modulation of the evoked responses in human auditory cortex during performing a delayed-match-to-sample (DMS) task by comparison to control tasks such as passive listening (PSL) and the simple counting (CNT). Performing the DMS task involves formation, maintenance, and manipulation of the short-term memory (STM) of the first sound in a pair of acoustic stimuli during the delay period (Gottlieb et al. 1989; Lu et al. 1992; Zatorre & Samson 1991; Zatorre et al. 1994), as well as decision making and motor responses based on the comparison to the perceived second one (Postle et al. 1999). By contrast, the PSL task does not require the active maintenance of the STM trace, although participants still need to listen to the sounds. Moreover, during performing the CNT task, the participants need not maintain the memory of the acoustic features, while it was required during performance of the DMS task. A task-specific

modulation of the auditory evoked responses to the second sound in the sound pair, which should be correlated with maintenance/retrieval of the STM of the first sound (Kaiser et al. 2003; Lutzenberger et al. 2002), was expected during performance of the DMS task but not in the control tasks. Additionally, it has been suggested that fronto-posterior oscillations during the delay period in frequency bands from theta to gamma were involved in memory processing and top-down inhibitory control (Klimesch 1999; Klimesch et al. 2007; Palva & Palva 2007). Here we investigated the DMS-specific functional interactions between cortical regions with the measurement of the coherence values between the current sources in three frequency bands (2~20 Hz, 20~30 Hz, and 30~50 Hz) to explore these top-down neural mechanisms involved in the DMS-specific modulation of the human auditory cortex.

3.2 Materials and Methods

Participants

Healthy right-handed adults (n=12; age, 23-35 years; six females) with normal or corrected-to-normal vision and normal hearing participated in the experiments. For each participant, the MEG and structural MRI signal were recorded in separate sessions. The participants gave the informed consents to the study, which were approved by the NIDCD-NINDS IRB (protocol NIH 92-DC-0178) and University of Maryland, College Park IRB (IRB#01566), before the scanning sessions.

Tasks and Stimuli

Ongoing MEG signals were recorded in three types of task conditions: passive listening (PSL), counting (CNT), and a delayed-match-to-sample (DMS) task. The stimuli (Fig. 3-1A) included pure tones (Tone, 350 ms acoustic stimuli with one frequency component) and tonal contours (TC, each TC stimulus consisted of two 125 ms up or down frequency modulated sweeps interspersed by a 100 ms tone). Each recording session was composed of 100 trials with the same type of sound stimuli and the same task. Each trial contained a 500 ms baseline period, followed by a pair of stimuli (S1 and S2, respectively) interspersed with a one-second silent period (delay period). Each stimulus was a sound with 350 ms duration and 65 ~ 75 dBA sound level. After presentation of S2, there was a 1.5 second inter-trial interval (ITI) before the baseline period of the next trial, which also served as the response interval in the DMS sessions (Fig. 3-1B). Within each session, match (identical sounds in the

pair) and non-match (different sounds in the pair) trials were randomly mixed and counter-balanced.

Each recording session began with visual instructions presented on a screen that informed the participants about the task condition, response requirement, and type of stimuli. The participants were also required to fixate on a cross mark at the center of the screen during each trial. During the PSL sessions, participants were instructed to relax, stay still and listen to the sounds without any response; during the CNT sessions, participants were instructed to count the number of sounds and report how many they heard; during the DMS sessions, participants were instructed to compare the two sounds in each trial, and press the left button with the left thumb for a match and press the right button with the right thumb for a non-match. The button box was held in both hands in all sessions. In addition to these task sessions, participants also had two training sessions before performing the DMS tasks (one type of stimulus for each, each session consisted of 40 trials) to become familiar with the task, and a click counting session, in which they were instructed to count the number of 50 ms 1kHz clicks they had heard, for the purpose of locating the representative sensors of the M100 response.

Data Acquisition

Participants lay in supine position during the MEG recording. MEG signals were recorded with the CTF Omega2000 275-channel whole-head MEG System (CTF Systems, Inc., Coquitlam, Canada) placed in a magnetically-shielded room (Vacuumschmelze, Germany) inside the MEG Laboratory of the National Institute of Mental Health (Bethesda, Maryland, USA). The ongoing MEG signals were sampled

at 600 Hz, filtered with 0-150 Hz bandpass analog filter, and balanced with 3rd gradient coils for noise reduction. The raw MEG signals were then stored for off-line analysis. The temporal events, such as stimulus onset and button presses (DMS sessions only) in each trial were on-line marked. In a separate session, the anatomical structure of the brain was obtained on a 3 Tesla Signa MR scanner (General Electric, Waukesha, WI), with a T1-weighted 3D MRI protocol (3-T MPRAGE; 24 cm FOV; 128 axial slices; 1 x 1 x 1.2 mm3 per voxel). Three head coils fixed at the nasion and the bilateral preauricular points were used for head motion detection during the MEG recording and in MRI scanning sessions the same points were marked with Vitamin E capsules for spatial alignment between the MEG sensors and the anatomical structures. During measurement of the MEG, the head coils were localized at the beginning and the end of each session to ensure that head movements did not exceed 0.5 cm.

Data Analysis

Preprocessing

Several steps were taken to reduce the noise and artifact contamination in the raw MEG signals: (1) the DC offset was removed based on the whole trial trend; (2) the power line noise plus harmonics were removed with notch filters at 60, 120, 180, and 240 Hz; (3) the MEG signal from each recording session was high-pass filtered with stop frequency at 0.5 Hz to remove the low-frequency fluctuations; and (4) artifacts (EKG, EOG and motion related signals) were identified and removed with an automatic clustering method based on independent component analysis (ICA) (Rong & Contreras-Vidal 2006, also see the chapter 2 of this dissertation). MEG signals

from three subjects (one male, two females) were removed from further analysis due to excessive artifact contamination. The noise reduced and artifacts cleaned datasets of the other nine subjects (four females) were then partitioned on a single-trial basis for further analysis. For each task trial, a 3.7 seconds epoch time-locked to the onset of S1 was extracted along with a 0.5 second baseline period (Fig. 3-1B). For each of the click counting trials, the epoch was 1.05 seconds time-locked to the stimulus onset with a 0.5 second baseline.

Quantification of the modulation effect

In this study, we were particularly interested in modulation of the auditory evoked responses (AERs) to the presentation of sound stimuli related to different task performance. For this purpose, we measured the AERs in both sensor and source spaces, and quantified the modulation effect by computing the values of a modulation index (MI). The MI values were then statistically analyzed to assess the task-specificity.

In sensor space, the measurements of the AERs were derived from a subset of representative sensors for each subject. These sensors were determined by examination of the M100 responses in the averaged epochs of the click counting session. The M100 response is usually seen as a deflection in the epochs of the averaged field strength at ~100 ms after sound stimulus onset, which has a bilateral dipole-like contour pattern of the magnetic field at the peak latency with a 'source' and a 'sink' located at fronto-temporal and parieto-temporal regions. For each subject, twenty sensors (ten per hemisphere) surrounding the centers of the sources and sinks of the M100 response in the click counting session were selected as the representative

sensors (Luo et al. 2005). The magnitudes of the M100 responses to the sound stimuli were then measured as the root mean square (RMS) value of the peak field strength averaged across the representative sensors for each hemisphere. After the magnitudes of the M100 responses to S1 and S2 for each experimental condition was determined, the MI value in sensor space was then computed as

$$MI = \frac{[(p1 - baseline) - (p2 - baseline)]}{[(p1 - baseline) + (p2 - baseline)]} \times 100\% \quad (3\text{-}1)$$

where $p1$ and $p2$ were the magnitudes of the M100 responses to S1 and S2 in the averaged epoch, respectively, and $baseline$ was the averaged RMS value of the field strength during the baseline period. Therefore, if the mean MI value from one condition was significantly greater than zero, it was considered to present a significant suppressive modulation effect, and vice versa.

In addition to the analysis in sensor space, we also investigated the modulation of AER in source space, where the evoked responses were computed from the moment strength of the equivalent current dipoles (ECDs). The ECDs were estimated using an event-related beamformer algorithm (Cheyne et al. 2006) based on the linearly constrained minimum variance (LCMV) method (Van Veen et al. 1997), for which the forward source-sensor relationship was determined by a multiple local-sphere head model (Huang et al. 1999; For a detail description of the forward and inverse solution, see Appendices A and B, respectively). For each participant, a 20 x 20 x 17 cm spatial grid covering the participant's head was used for the inverse estimation, where the grid was composed of 5x5x5 mm3 cubic voxels, and the integrated intracellular synaptic currents of the neuronal population in each voxel was

represented by an ECD whose basis was located at the center of the voxel. For each ECD, the normalized power (neural activity index) of the moment strength was computed as a measurement of the corresponding source activity (Van Veen et al. 1997). We then took following procedures to determine the auditory representative ECDs for each participant and quantify the modulation effect based upon analysis of the source activity of the representative ECDs: (1) the neural activity index for each ECD was computed on a single trial basis; (2) for each ECD in each trial, the evoked responses to S1 and S2 were computed by summing up the power of the source activity across a 50 ms time window with the center at the peak latency of the M100 response to corresponding stimulus, and normalized by the averaged power during the baseline period. Therefore, within each participant, we obtained one set of evoked response values for each stimulus under one task x trial type x sound type experimental condition; (3) we then applied paired t-test to compare the evoked responses to S1 and S2 for each ECD within each experimental condition. The ECDs showed significant difference (corrected $p<0.05$) were considered demonstrating within-participant significant modulation of the evoked response for the corresponding condition. Hence the significant ECDs located in the temporal regions obtained from the comparison within the DMS conditions were considered as the ECDs that showed DMS-related modulation effect of the AER; (4) for each participant, among the ECDs demonstrated DMS-related modulation of AER, the one with the maximal absolute t value was selected as the representative ECD for further analysis, and one representative ECD was selected for each hemisphere; (5) a MI value was then calculated for each experimental condition using equation (3-1) by

replacing the RMS values of the field strength by the source activity of the representative ECDs.

The MI values obtained from all subjects in both sensor and source spaces were then statistically analyzed with repeated measures ANOVA with three factors: task (PSL, CNT, DMS), sound type (Tone, TC), and trial type (match, non-match), to test the hypothesis that the modulation of the evoked responses in auditory cortex was significantly different in the DMS tasks than in the control tasks. The post-hoc multiple comparisons of means were applied using the Tukey-Kramer method. The statistical analyses of the MI values were performed with SAS v9.1 (SAS Institute Inc., Cary, NC, USA.).

In the source space, in addition to assessment of the modulation effect by selecting a few ECDs to represent the cluster within the auditory cortex that showed significant difference, we took another approach to confirm the DMS-specific modulation effect within the auditory cortices: In stead of computing the MI values with only the selected representative ECDs, we calculated the MI values for all ECDs, and input the MI values obtained from all subjects into a two-way three-dimensional ANOVA method to determine the cortical regions that showed DMS-specific modulation of the AER as compared to the passive listening control conditions. The variance analysis was done by using the type 4 3dANOVA3 AFNI script (Cox 1996; NIMH, Bethesda, MD, USA; also refer to http://afni.nimh.nih.gov/) with two factors: tasks (PSL and DMS) and sound types (Tone and TC). To avoid inflation of the significance by comparison with multiple ECDs, Monte Carlo simulation with estimation of the between-ECD spatial correlation (Forman et al. 1995; Xiong et al.

1995) was used to determine the criteria (the threshold cluster size and uncorrected probability value for each ECD within the cluster) of statistical significance. Therefore, if there is a cluster of ECDs located in auditory cortex showed significant difference between the MI values in DMS and PSL task conditions, we could draw the conclusion that there is a DMS-specific modulation effect to the auditory evoked responses as compared to the PSL conditions.

Analysis of the functional interaction among brain regions

After analysis of the AER modulations, the correlated dynamics of functional interactions were then investigated with the measurements of coherences between ECDs. For each participant, the representative ECD that demonstrated the DMS-specific modulation effect was selected as a reference, and the coherence between the source activities of this reference ECD and ECDs in other brain regions were computed in frequency bands of 2~20 Hz, 20~30 Hz and 30~50 Hz using the dynamic imaging of coherent sources (DICS) method (Gross et al. 2001). For each frequency band, the modulation related functional interactions were quantified as the ratio of coherence change (RCC) values, which were computed as normalized differences between the coherence values obtained from the late delay period (0.5 ~ 1 sec after offset of S1, which denoted a 500 ms window before onset of S2) and the coherence values obtained from the baseline period (-0.5 ~ 0 sec before onset of S1)

$$. \ RCC = \frac{(Ldelay - baseline)}{(Ldelay + baseline)} \tag{3-2}$$

where $Ldelay$ and $baseline$ represented the coherence values in late delay and baseline periods, respectively. We then used the two-way three-dimensional ANOVA

method described in above section to analyze the RCC values and to test the hypothesis that during the late delay period of the DMS task, the auditory cortical regions that displayed DMS-specific modulation effects had increased functional interactions with the other brain regions that were specifically recruited for performance of the DMS tasks. The factors included task (PSL and DMS) and sound type (Tone and TC), and Monte Carlo simulation was also used to estimate the criteria (the threshold cluster size and uncorrected probability value for each ECD within the cluster) of statistical significance.

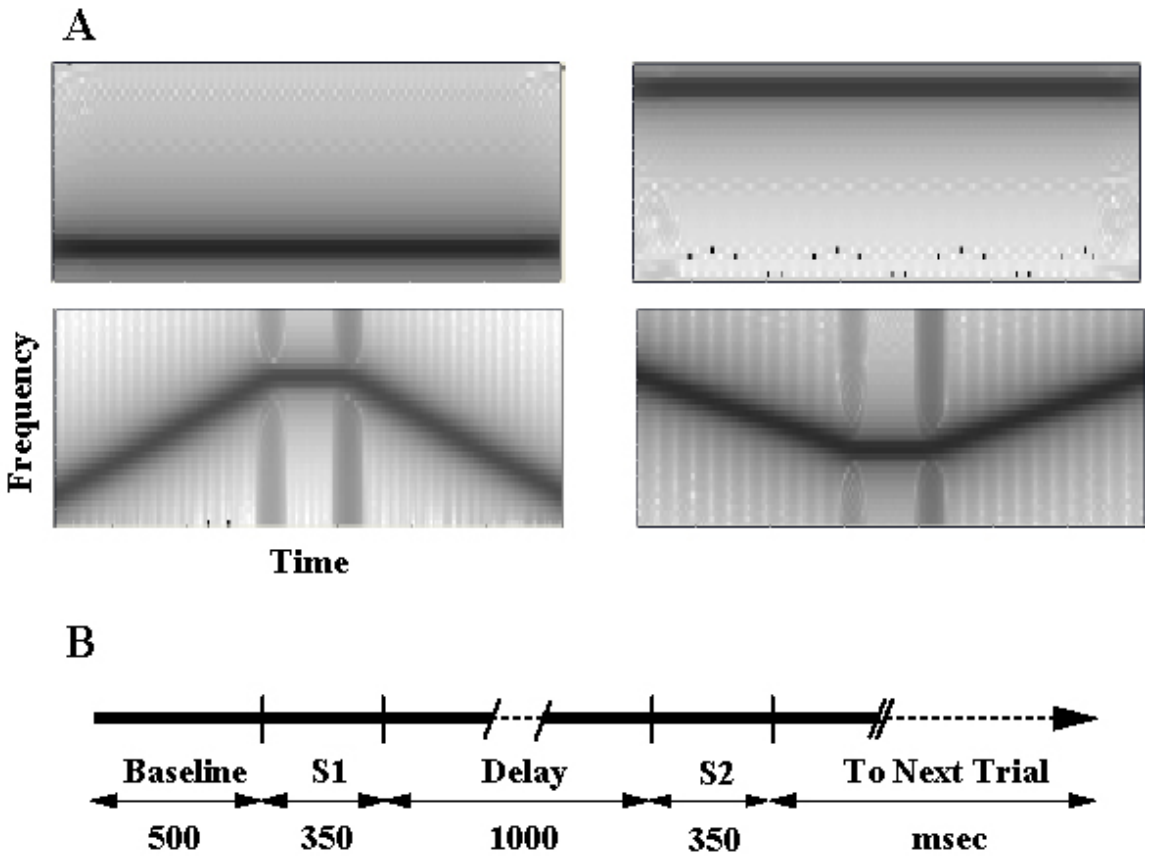

Fig 3-1 (A) The spectrogram of the representative stimuli. The gray scale represents the power spectral density (dB/Hz) of the sound stimuli. (B) The timeline of each trial. S1 and S2 denotes the time window of the stimuli presentation. The inter-trial-interval (ITI) was 1.5 second.

3.3 Results

3.3.1 Behavioral data

In the CNT task, all subjects recalled the number of sounds they heard with counting error within ± 2 sounds in each session.

In the DMS task, all subjects showed accuracy above 84% across the combinations of different sound types (Tone or TC) and trial types (match or non-match). However, a significant sound type * trial type interaction was observed ($F_{1, 24}$ = 12.9, $p<0.01$), which was correlated to the lower performance level of the TC non-match trials (91.1 ± 0.95%, mean ± SEM) than the other three conditions (Tone match: 99.8 ± 0.95%, Tone non-match: 98.7 ± 0.95%, TC Match: 98.9 ± 0.95%).

Response time (RT) in each trial was measured as the time elapsed from the onset of S2 to the button press. ANOVA revealed a significant sound type effect on RT (Fig. 3-2; $F_{1, 8}$=6.1, $p<0.05$), which showed that the RT to TC (812.4 ± 36.35 ms, mean ± SEM) is significantly longer than the RT to Tones (754.1 ± 36.32 ms). No significant effect of trial type or sound type * trial type interaction was observed. The longer RT for TC was consistent with the results in an fMRI study with same set of stimuli (Husain et al. 2004), and might be due to the longer temporal integration required for the recognition of tonal contours than tones.

3.3.2 Modulation effect in the sensor space

Ten frontal-temporal and parietal-temporal sensors in each hemisphere surrounding the local maxima of ‘sources’ and ‘sinks’ of the magnetic field at the

peak latency of M100 responses in the click-counting session were selected as representative sensors for each subject (see Fig 3-3 A, D).

In the left hemisphere, the grand mean RMS of the field strength obtained from the representative sensors across all participants showed a pattern of decreased M100 responses to S2 as compared to responses to S1 in all experimental conditions except the non-match pure-tone trials (Tone_M), where The DMS_TC_M condition showed the greatest reduction (Fig 3-3 B). A greater than zero mean MI value was demonstrated in the DMS_TC_M condition ($t_{8, 0.05} = 5.61$, $p<0.05$) but not in other experimental conditions. Furthermore, ANOVA of the MI values demonstrated significant sound type ($F_{1, 24} = 12.18$, $p<0.01$) and trial type ($F_{1, 24} = 7.74$, $p<0.05$) main effects and a significant task * sound type * trial type interaction ($F_{2, 24} = 8.93$, $p<0.01$). However, no significant task effect was demonstrated by either ANOVA ($F_{2, 16} = 0.18$, $p>0.05$) or comparison between conditions.

In the right hemisphere, the averaged RMS waveforms showed a suppressive pattern of the M100 responses to S2 in all conditions except DMS_Tone_N (Fig 3-3 E). ANOVA of the MI values demonstrated a trial type effect ($F_{1, 8} = 10.88$, $p<0.05$), where suppression of the M100 response to S2 for the match trials was greater than the nonmatch trials. No task or sound type main effect or any of the interaction effects was revealed by the statistical analysis. No mean MI value was significant different from zero across the experimental conditions.

To summarize the results in sensor space, a significant suppression of the M100 response to S2 as compared to the response to S1 was revealed by the left representative sensors in the DMS_TC_M condition. However, no significant

difference between tasks was observed by statistical analysis of the MI values for both hemispheres. However, the lack of task-related difference of the MI values in sensor space among conditions may due to the different task-related dynamics of the multiple cortical sources that contributed to the M100 response (Näätänen & Picton 1987; Hari 1990), whose locations were found not only in the auditory cortex, but also in other anterior and posterior regions. Thus, further analysis of the MI values obtained from the measurement of the neuronal activity in the bilateral superior temporal cortices is necessary to assess the task-specificity of the modulation to AER in a more focused manner.

3.3.3 Task-specific modulation effect revealed in left auditory cortex

For each experimental condition, within participant comparison in source space revealed clusters of ECDs that showed significant difference between the evoked responses to S1 and S2, and the locations and compositions of the clusters were different from each other among the conditions and participants. For instances, in figure 3-4 (A), the three subplots illustrates the probability maps of the left hemisphere ECDs obtained from the paired t-test in PSL, CNT and DMS tasks with TC stimuli for participant #4, respectively, where each map were plotted over a standard anatomical atlas (Talairach & Tournoux, 1988). Each subplot depicted several clusters that composed of the voxels with the corresponding ECD showed significant difference between the evoked responses to S1 and S2. The cluster in the superior temporal region (where auditory cortex is located) was larger for the DMS task than the control tasks, which indicated a larger suppressive modulation effect during performance of the DMS task for this participant. In contrast, in the cluster

anterior to the auditory cortex, fewer ECDs showed a significant difference during performing the DMS task, indicating a weaker modulation effect for the frontal sources. Furthermore, in the cluster posterior to the auditory cortex, an opposite sign of the modulation effect was demonstrated during performance of the DMS task (a greater response to S2 than the response to S1), which suggested enhancement rather than suppression for these current sources. A similar pattern of the task-specific modulation of the left auditory cortex was seen in eight out of nine subjects.

Figure 3-4 B displays the grand mean AER waveforms of the left representative ECDs averaged across the participants. A suppressed AER to S2 was demonstrated with performance of the DMS task but was not observed in the control tasks. The locations of these ECDs (Talairach coordinates: [-52.1 ± 9.33, -24.3 ± 7.83, 7.6 ± 4.67], mean ± SD) were within the vicinity of the left primary auditory cortex (Heschl's gyrus) and adjacent planum temporal region (Hall et al. 2002), which is consistent with the distribution of the superior temporal sources for M100 responses that have been described in previous studies (Herdman et al. 2003; Näätänen & Picton 1987; Hari 1990). Across subject analysis of the MI values demonstrated significant effects of task (ANOVA, $F_{2, 16} = 9.64$, $p<0.01$), sound type ($F_{1, 24} = 5.06$, $p<0.05$), and task * sound type interaction ($F_{2, 24} = 3.43$, $p<0.05$). No trial type effect or other interaction effects were observed. There was a significant suppressive modulation of the evoked responses to S2 as compared by the responses to S1 for both DMS_Tone ($t_{17, 0.05} = 4.48$, $p<0.05$) and DMS_TC ($t_{17, 0.05} = 7.80$, $p<0.05$) as shown by the mean MI values (Fig 3.4c), where none of the mean MI values from the control tasks was significantly different from zero. Comparison

between conditions demonstrated that the mean MI value of DMS_TC condition was significantly greater than both PSL_TC ($p<0.01$, Tukey-Kramer method) and CNT_TC ($p<0.01$) conditions, which indicated a greater suppression of the left auditory AER to S2 during performing the DMS task with TC stimuli. For the MI Values with Tones stimuli, no significant difference was observed between tasks, although DMS_Tone displayed a greater mean MI value than the control tasks (Fig 3-4 C). Furthermore, the significantly greater mean MI value for DMS_TC than DMS_Tone ($p<0.05$, Tukey-Kramer method) could account for the task * sound type interaction effect, and also suggests a greater suppression effect for TC than for Tones in performing the DMS task. Individual data showed seven out of nine participants (except participants #1 and #2) with greater MI values (Fig. 3-4 D) for DMS_TC as compared to the PSL_TC condition, indicating a consistency of the modulation effect to the left auditory cortex among individuals.

Figure 3-5 (A) illustrates the clusters of ECDs in the right hemisphere of participant #4 showing a significant difference between AERs to S1 and S2 during performance of the tasks with TC stimuli. In contrast to the left hemisphere, the cluster in the right temporal region displayed a similar modulation pattern across all three tasks for this participant. The locations of the right representative ECDs were almost symmetric to the left representative ECDs (Talairach coordinates: [-56.8 ± 6.50, -24.3 ± 6.06, 9.1 ± 7.91], mean ± SD), where the center coordinates falling in the vicinity of the right auditory cortex. However, the averaged AER waveforms from the right representative ECDs showed a pattern different from what is seen on the left side: Suppression of the AERs to S2 was seen in all three tasks, although for

the Tone stimulus, the CNT and DMS tasks showed a reduced suppressive modulation effect (Fig 3-5 B). There was no difference in the mean MI values across all three tasks (Fig 3-5 C; ANOVA, $F_{2, 16} = 2.44$, $p=0.12$). Consistent with the mean MI values across the subjects, individual data showed smaller differences in the MI values between the DMS_TC and PSL_TC conditions for the right representative ECDs as compared to the left hemisphere (Figure 3-5 D).

Furthermore, the analysis of the MI values across all ECDs in source space confirmed the findings with the representative ECDs by showing a cluster of ECDs in the left auditory cortex with significant suppression of the AER to S2 in DMS tasks as compared to the PSL condition (Figure 3-6 A), where the cluster extended from the left superior temporal regions to the left insula. Two other clusters also showed up with greater suppressive modulation effect during performance of DMS task than during the PSL conditions. One was located at the left orbital frontal region (Figure 3-6 B) and another one was in the premotor area of the right middle frontal cortex (Figure 3-6 C), suggesting their involvement of performing the auditory DMS tasks.

3.3.4 Functional interactions underlying the task-specific modulation effect

Analysis of the modulation effect in cortical source activities demonstrated a DMS-specific suppressive modulation of the AER in response to S2 in the left auditory cortex. We then asked if there were correlated task-specific dynamics of the functional interactions between the left auditory cortex and other brain regions. To answer this question, we used the left representative ECDs as the reference dipoles and used the DICS method (Gross et al. 2001) to evaluate the coherence values between ECDs, and computed a RCC value from the coherence values to represent

the changes of the functional interaction. Three dimensional two-way ANOVA of the RCC values revealed five cortical regions that showed significant task-related changes of their interregional functional interactions with the reference dipole in left auditory cortex: For the frequency band of 2~20 Hz, two clusters of ECDs demonstrated significant task * sound type interaction and significant or close to significant differences between the PSL_TC and DMS_TC conditions. One cluster consisted of 24 ECDs located in left anterior cingulate cortex (ACC, BA32, Fig 3-7 A), and another cluster with 11 ECDs located in the left precentral gyrus (BA4/6), in which the center ECD was located in the pre-motor area (Fig 3-7 B). The mean RCC values of the center ECDs of these two clusters demonstrated increased coherence values during the delay period of the DMS_TC condition as being compared to the PSL_TC trials. Moreover, in the same frequency band, another cluster of 18 ECDs located in the right middle frontal gyrus (BA6/9) showed a significant task effect, in which the center ECD located in the pre-motor area and demonstrated increased coherence values for both tones and TC during the delay period of the DMS task (Fig 3-7 C). For the frequency band of 20~30 Hz, one cluster of 10 ECDs located in the right ventral-lateral prefrontal cortex in inferior frontal gyrus (Fig 3-7 D) demonstrated a significant task effect with the center ECD showed increased coherence values during the delay period of the DMS task as compared to PSL condition. For the frequency band of 30~50 Hz, another cluster of 14 ECDs located in the right superior temporal gyrus (BA42/22) showed a significant task * sound type interaction and close to significant PSL_TC vs. DMS_TC difference. The center ECD demonstrated an increased coherence for DMS task with TC stimuli, and decrease

coherence for DMS task with Tone stimuli as compared to PSL conditions (Fig 3-7 F).

A similar analysis of the functional interaction between the left reference ECD and other brain regions was also undertaken with seven participants (without participants #1 and #2) considering the consistent modulation pattern of the left auditory cortex among these subjects. Except the clusters described above, a cluster of 35 ECDs extending from the ventral-lateral prefrontal cortex in the left inferior frontal gyrus (BA 47) to the anterior superior temporal gyrus (BA 42) and left Insula (BA 13) showed a significant task effect, where the center ECD showed increased coherence during the late delay period of the DMS task, whereas during the PSL task a reduction of inter-regional coherence between these ECDs and the reference dipole during the late delay period was observed (Fig 3-7 E).

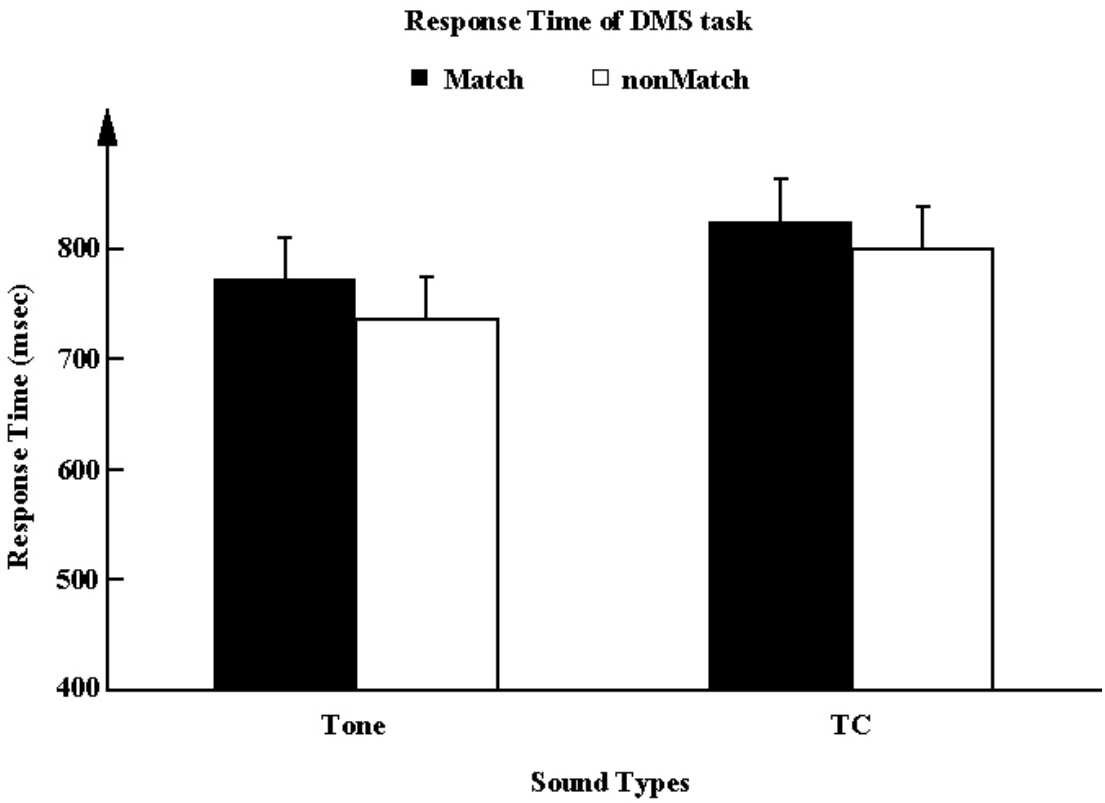

Fig 3-2 Mean ± SEM of the response times (RT) in DMS task (n=9). Response times were calculated as the duration elapsed from the onset of S2 to participants pressing the button for each trial.

Fig 3-3 Modulation effects in sensor space. (A) The alignment of the 10 representative sensors at left hemisphere. The view is from the left side. Blue sensors locate around the local maxima of 'sink' and red sensors locate around the local maxima of 'source' of the magnetic field at peak latency of the M100 response. Data were from the click counting session of participant #4. (B) The mean RMS waveforms of the field strength for the representative sensors at left hemisphere averaged across all participants. Each column represents one sound type * trial type combination and each row consists of the conditions within one task. In each subplot, RMS with the epoch of 50~250 ms aligned to the onset of S1 and S2 are plotted together, in which the blue trace is the averaged RMS aligned to the onset of S1, and red trace is the averaged RMS aligned to the onset of S2, respectively. (C). Mean ± SEM of the MI values computed from magnitude of the M100 responses across all participants. (E), (F) and (G) are plots for right hemisphere similar to (A), (B) and (C), respectively.

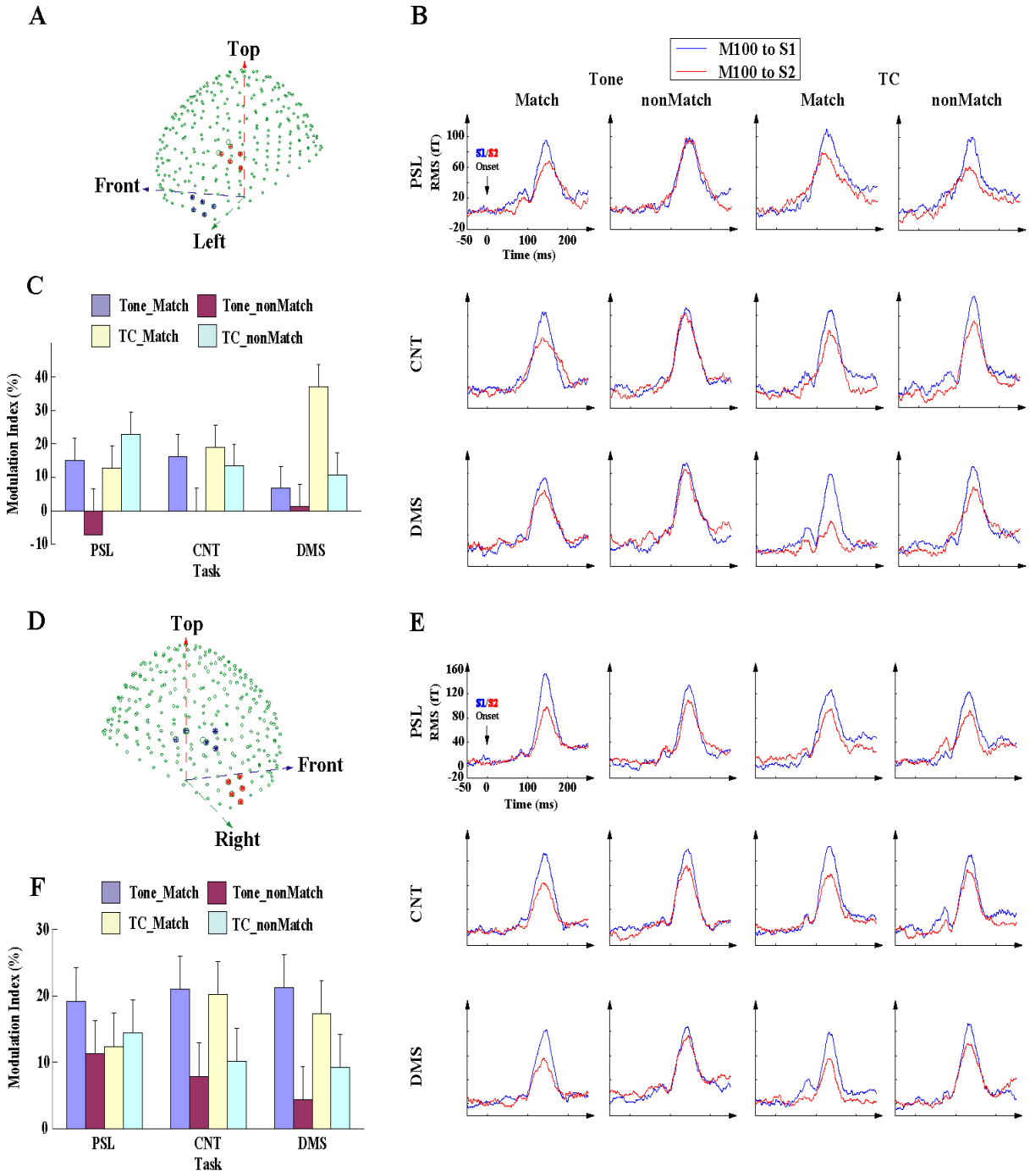
A
Top
Front
Left
B
M100 to S1
M100 to S2
Tone
TC
Match
nonMatch
Match
nonMatch
PSL
RMS (fT)
S1/S2
Onset
Time (ms)
CNT
DMS
C
Tone_Match
Tone_nonMatch
TC_Match
TC_nonMatch
Modulation Index (%)
PSL
CNT
DMS
Task
D
Top
Front
Right
E
F
Tone_Match
Tone_nonMatch
TC_Match
TC_nonMatch
Modulation Index (%)
PSL
CNT
DMS
Task

Fig 3-4 Task-specific modulation of the left auditory cortex. (A) The probability maps indicates the clusters of ECDs in left hemisphere that showed significant difference between the evoked responses to S1 and S2 by paired t-test with the experimental conditions of PSL_TC, CNT_TC and DMS_TC, respectively. The colors represents the negative logarithmic values of the probabilities for each ECD, which are plotted over the axial slices (z=6) of the Talairach anatomical atlas (Talairach & Tournoux, 1988). The cut off threshold of the displayed color values equals 8. Data were from participant #4. The location of the representative ECD in left auditory cortex for this participant is marked by a '*'. (B) Averaged neural activity index of the left representative ECDs time-locked to the onset of stimuli. Data were obtained by averaging across all participants. Mean ± SD Talairach coordinates of the representative ECDs are illustrated above the waveforms. Dash line box highlights the AER peak with the latency ~ 100 ms after the stimuli onset. (C) Mean MI values computed from the source activity of the left representative ECDs averaged across all participants. Error bars denote the standard error of means (SEM). (D) The mean and standard deviation of the MI values for each individual subject obtained from single trials during performing the PSL and DMS tasks with TC stimuli.

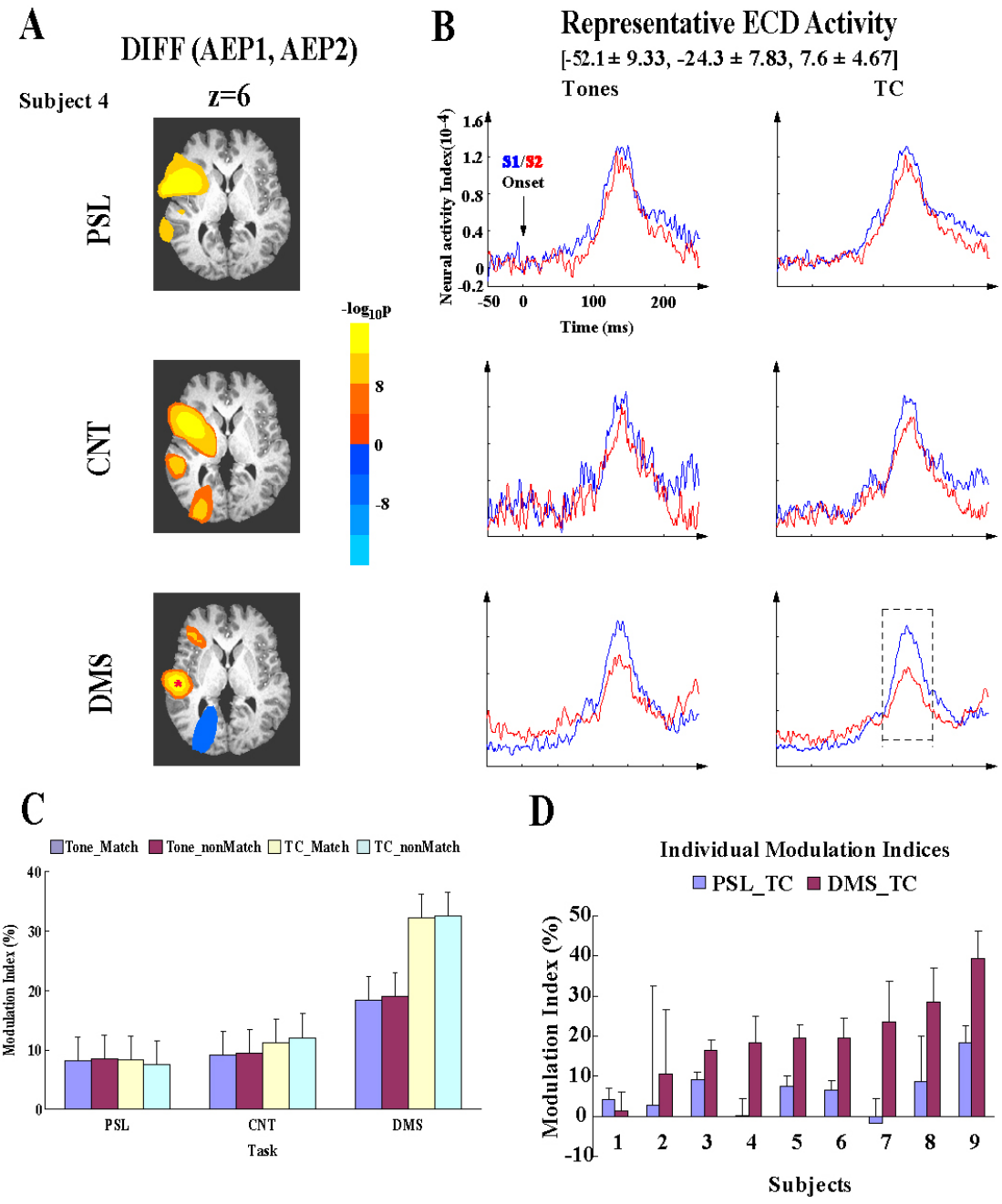
A
DIFF (AEP1, AEP2)
Subject 4
z=6
PSL
CNT
DMS
-log10p
8
0
-8
B
Representative ECD Activity
[-52.1 ± 9.33, -24.3 ± 7.83, 7.6 ± 4.67]
Tones
TC
Neural activity Index(10-4)
S1/S2
Onset
Time (ms)
C
Tone_Match
Tone_nonMatch
TC_Match
TC_nonMatch
Modulation Index (%)
PSL
CNT
DMS
Task
D
Individual Modulation Indices
PSL_TC
DMS_TC
Modulation Index (%)
Subjects

Fig 3-5 Task-invariant modulation of the right auditory cortex. (A) The probability maps show the clusters of ECDs in right hemisphere that showed significant difference between the evoked responses to S1 and S2 in PSL_TC, CNT_TC and DMS_TC experimental conditions. Data were from participant #4. The statistical criteria were the same to the left hemisphere. Anatomical axial slice was obtained from z=20. The representative ECD in right auditory cortex of this participant is marked by a '*'. (B) Averaged neural activity index of the right representative ECDs time-locked to the onset of stimuli. (C) Means and SEMs of The MI values computed from the neural activity index of the right representative ECDs. D) The mean ± SD of the MI values for each individual participant obtained from single trials during performing the PSL and DMS tasks with TC stimuli. The order of participants is the same to fig 3-4 (D).

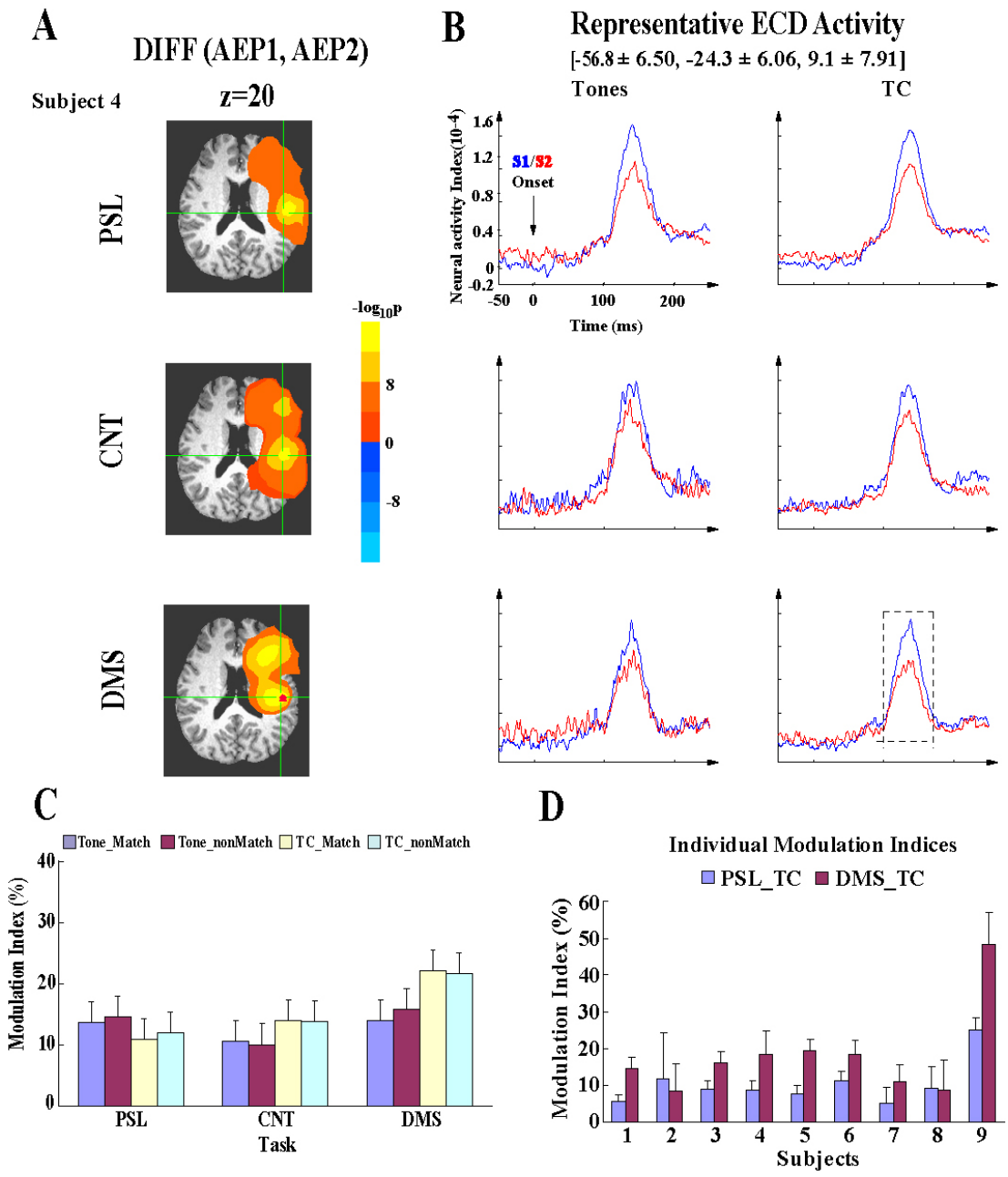
A
DIFF (AEP1, AEP2)
Subject 4
z=20
PSL
CNT
DMS
-log10p
8
0
-8
B
Representative ECD Activity
[-56.8 ± 6.50, -24.3 ± 6.06, 9.1 ± 7.91]
Tones
TC
S1/S2
Onset
Neural activity Index(10-4)
Time (ms)
C
Tone_Match
Tone_nonMatch
TC_Match
TC_nonMatch
Modulation Index (%)
PSL
CNT
DMS
Task
D
Individual Modulation Indices
PSL_TC
DMS_TC
Modulation Index (%)
Subjects

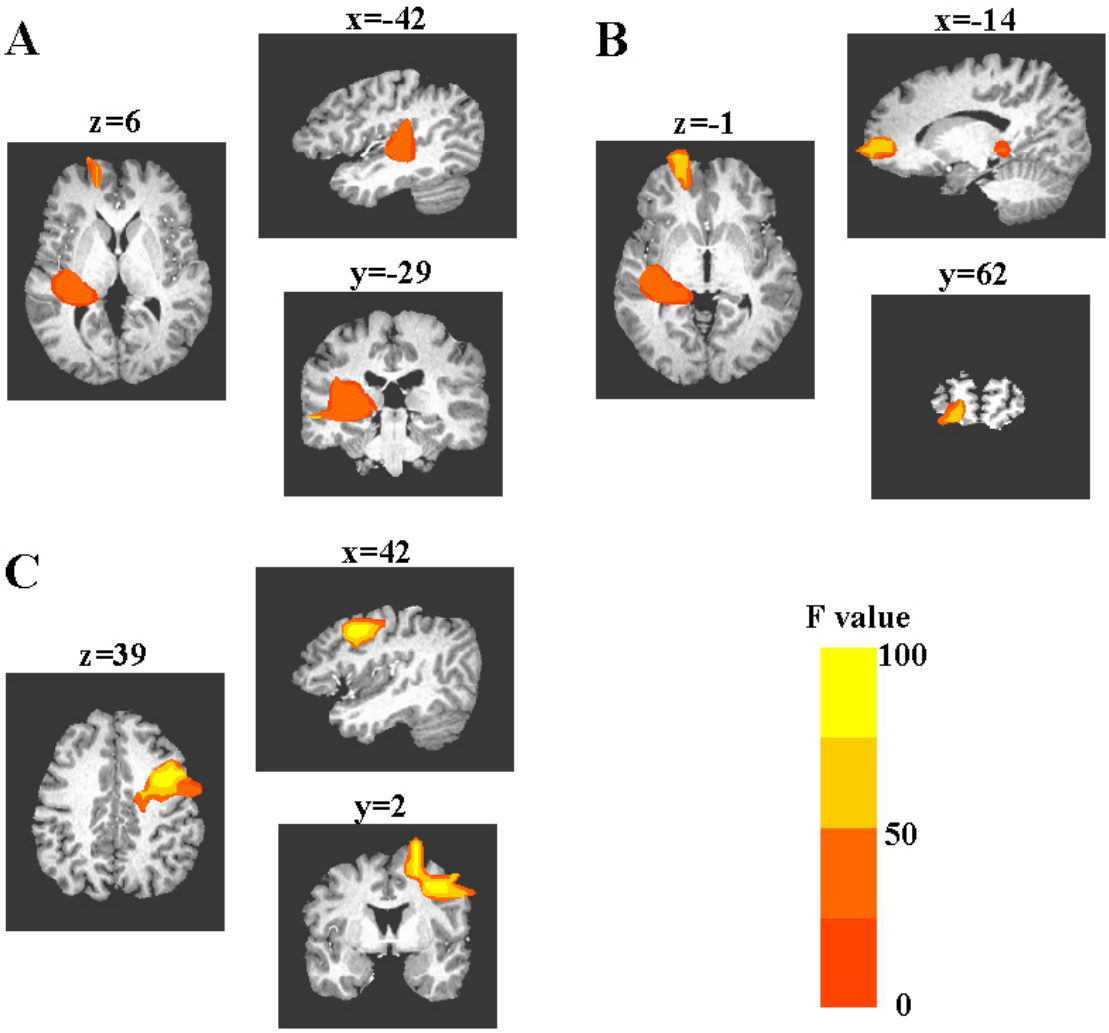

Fig 3-6 Grand-analysis of the MI values across all ECDs. 3dANOVA was applied to the MI values obtained from PSL and DMS tasks, Monte Carlo simulation was used to determine the threshold cluster size of significance (n=9, threshold cluster size for F-test is 17, with each ECD showed uncorrected $p<0.01$). Axial, sagittal, and Coronal views of the clusters showed significant task-related effect on the MI values were displayed, where the color represents the F-values. (A) The cluster in left auditory cortex, which included the ECDs in both superior temporal gyrus (BA41/22) and insula (BA13). (B) The cluster in left medial frontal gyrus (BA10) and. (C) The cluster in right middle frontal gyrus (BA6).

Fig 3-7 Task-specific changes of functional interaction between the left auditory cortex and other brain regions, which were obtained from analyses of the ratio of coherence change (RCC) values between PSL and DMS tasks with both Tone and TC stimuli. Subplots (A), (B) and (C) were from analysis with frequency range of 2~20 Hz. Subplots (D) and (E) were from analysis with frequency range of 20~30 Hz. Subplot (F) were from analysis with frequency range of 30~50 Hz. All results were derived from analysis with nine participants except (E), which was obtained from analysis with seven participants (without participants #1 and #2). In each subplot, the left inset maps the statistics of each ECD within the cluster (t or F values) with smoothed color values overlapped on a standard Talairach anatomical atlas (TT_N27), where the right insets depicts the Mean ± SD of RCC values obtained from the center ECD of the cluster. (A) and (B) depict the clusters showed significant task * sound type interaction and close to significant difference between PSL_TC and DMS_TC conditions. In both figures the color values represented the t values from the contrast between PSL_TC and DMS_TC conditions, which are mapped over a sagittal slice (x = -7) for (A) and an axial slice (z=55) for (B). In (A) the center ECD with the maximal t value in the cluster located in left ACC, whose Talairach coordinates were [-7 -20 -8]. In (B) the center ECD of the cluster located in left middle frontal gyrus, and whose Talairach coordinates were [-45 -15 55]. C) The cluster of ECDs showed significant task effect. The color values represent the F values of the task effect and are mapped over an axial slice (x = 34). The center ECD of the cluster located in right middle frontal gyrus, whose Talairach coordinates were [49 -6 34]. D) The cluster of ECDs showed significant task effect. The color values

represent the F values and are mapped over a sagittal slice (x = 42). The center ECD of the cluster located in right inferior frontal gyrus, whose Talairach coordinates were [42 -41 -1]. E) The cluster of voxels showed significant task effect. The color values represented the F values plotted over an axial slice (z = 0). The center ECD of the cluster located in left inferior frontal gyrus, whose Talairach coordinates were [-35 -1 -1]. F) The cluster of voxels showed significant task * sound type interaction and close to significant difference between PSL_TC and DMS_TC conditions. The color values represent the t values obtained from the PSL_TC vs. DMS_TC contrast and are mapped over an axial slice (z = 6). The center ECD in this cluster located in right superior temporal gyrus, whose Talairach coordinates were [63 -29 6].

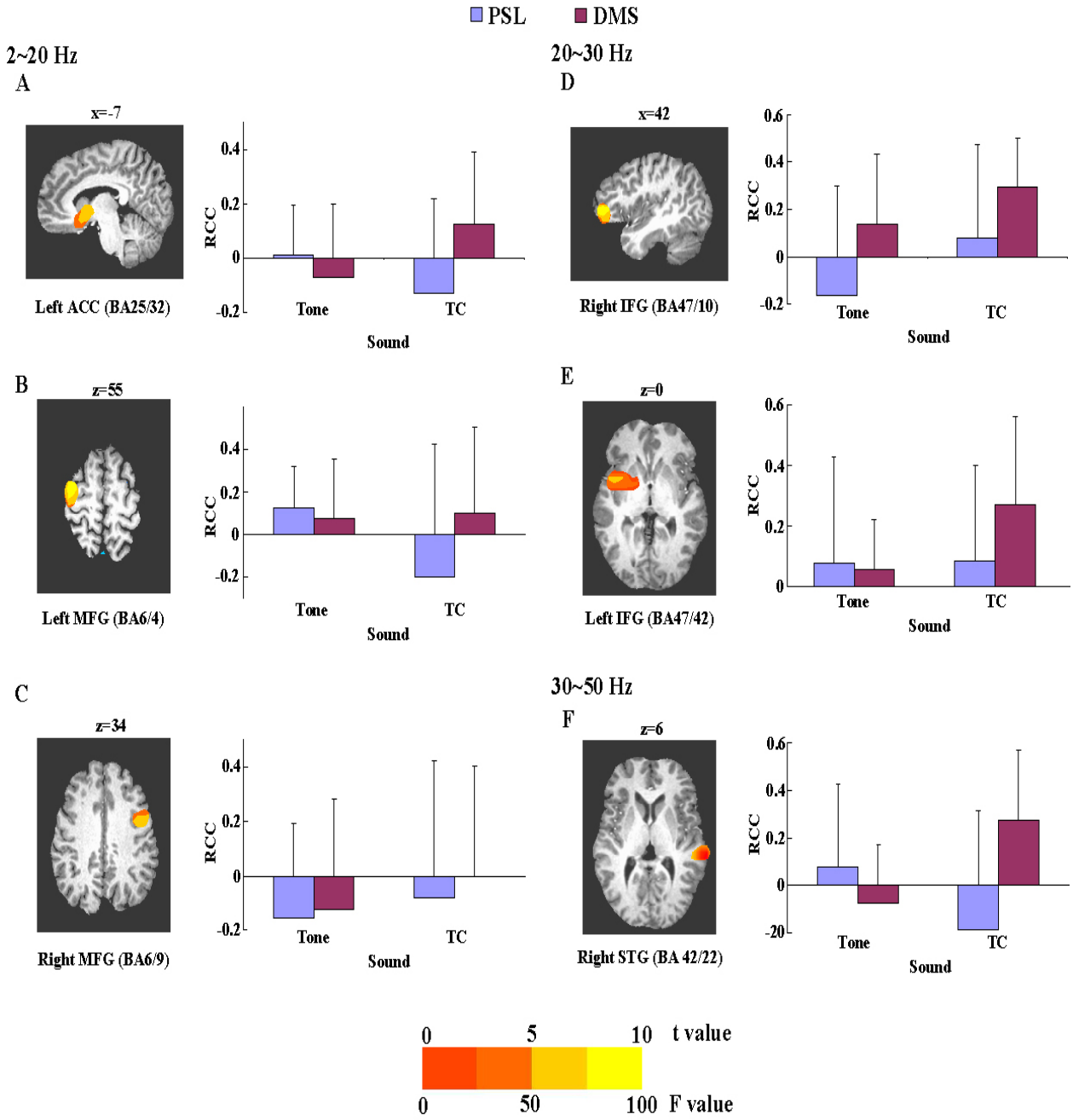
PSL
DMS
2~20 Hz
A
x=-7
Left ACC (BA25/32)
RCC
Tone
TC
Sound
B
z=55
Left MFG (BA6/4)
C
z=34
Right MFG (BA6/9)
20~30 Hz
D
x=42
Right IFG (BA47/10)
E
z=0
Left IFG (BA47/42)
30~50 Hz
F
z=6
Right STG (BA 42/22)
0 5 10 t value
0 50 100 F value

3.4 Discussion

3.4.1 Summary of results

The current experiment aimed at investigating the top-down modulation of human auditory cortex by task-specific cognitive functions recruited during performance of the auditory delayed-match-to-sample (DMS) task, which specifically emphasizes the maintenance of the short-term memory (STM) during the delay period and decision-making based on comparison between the STM trace and perception of the acoustic stimulus (Posner 1967). This DMS specific modulation effect was demonstrated as a suppression of the auditory evoked response (AER) with latency around 100 ms by comparison with control tasks such as passive listening (PSL) and counting (CNT). The auditory current sources showing this effect were lateralized to the left hemisphere, where the cluster of the significant equivalent current dipoles (ECD) covered both primary and association auditory cortices (Fig. 3-4a, Fig. 3-6a) with the center located in the superior temporal gyrus (STG). Furthermore, the modulation effect was greater for tonal contours (TC) than for tones in DMS task, which indicated a stimulus specificity of this effect. Furthermore, corresponding enhancement of the functional interactions between the left auditory cortex and frontal regions during the delay period of the DMS task were observed in the frequency bands of 2~20 Hz and 20~30 Hz. These regions included the lateral and orbital prefrontal regions in the inferior frontal gyrus (IFG) and the left anterior superior temporal region, premotor areas in the middle frontal gyri, and the anterior cingulate cortex (ACC). In the frequency range of the gamma band (30~50 Hz), it was right auditory cortex that demonstrated a DMS specific enhanced functional

interaction with left auditory cortex during the late delay period, suggesting the task-specificity of the interhemispheric inhibition between the bilateral auditory cortices. These results are consistent with previous findings suggesting the involvement of top-down modulation in the early phase of the auditory information processing and the task specificity of this modulation (for a review, see Scheich et al. 2007). Furthermore, our findings of DMS-specific enhancement of functional interactions between auditory cortex and multiple frontal regions suggest participation of multiple cognitive functions in the observed modulation effect. According to the location of the corresponding regions, these cognitive functions may include short-term memory, inhibitory control, and motor response preparation.

3.4.2 Task-specific cognitive modulation of auditory evoked responses

Measured by MEG/EEG, with peak latency around 100 ms after the stimulus onset, the M100/N1 response was believed to be involved in detection of changes in the acoustic environment (Rinne et al. 2006), and to which influences from both upstream and downstream auditory cortical regions have been demonstrated (Hari 1990, Näätänen & Picton 1987). With a variety of experimental paradigms, suppression of this response has been observed by passive listening to repetitively presented stimuli (Näätänen & Picton 1987) and by the active auditory perception during task performance (Hillyard et al. 1973; Worldorff et al. 1993; Luo et al. 2005; Martikainen et al. 2005). To account for these observations, a broad spectrum of interpretations from pre-attentive habituation (Baldeweg 2006) to cognition related top-down modulation (Scheich et al. 2007; Fritz et al. 2007) have been proposed.

With supportive experimental results mainly obtained from mismatch negativity (MMN) studies (Näätänen 1990), the habituation hypothesis postulated that the stimulus-specific adaptation to repetitively presented sounds suppresses the evoked response to an upcoming stimulus, given the upcoming one has similar salient features. According to this hypothesis, the sound stimuli are perceived through a series of hierarchical adaptive filters up to the frontal cognitive centers. During this procedure an implicit memory trace of the salient features is built up gradually, which in turn provides a prediction of the upcoming stimulus. It is the deviation between the prediction and the actual perception that determines the magnitude of the M100/N1 response. Therefore the magnitude of the M100/N1 response will be suppressed if the upcoming stimulus has similar salient features to the repetitively presented preceding ones (Tiitinen et al. 1994; Näätänen et al. 2001). Thus, according to the hypothesized hierarchical, gradual and implicit procedures of memory establishment, maintenance and retrieval, the suppressive modulation effect should be greater and earlier with increased repetition, to which the supportive evidence has been revealed by a recent study manipulating the number of 'standard' stimuli before presenting the 'deviant' sound (Haenschel et al. 2005).

By contrast, active performance of cognitive tasks has also demonstrated suppression of AER without reliance on repetitively presenting the identical sounds. For instances, with a dichotic listening paradigm, modulations of the M100/N1 response have been demonstrated with relatively suppressed magnitude to the unattended stimuli and enhanced magnitude to the attended stimuli (Hillyard et al. 1973, Woldorff et al. 1993). This intramodal attentional modulation effect was also

found for the anterior and posterior pathways depend on the feature (spatial or temporal-spectral) to be attended or ignored (Ahveninen et al. 2006). Moreover, intermoal selective attention studies also showed modulation effects on AERs , where suppression to the unattended modality was observed in both animals (Oatman 1971, 1976) and human beings (Alho et al. 1994; Eimer et al. 2004). In another type of behavioral paradigm, self-initiation of tones (Schafer et al. 1973; Martikainen et al. 2005) or speech (Houde et al. 2002) suppressed the M100/N1 response compared to the responses to externally generated sounds; the prediction of the upcoming sensory feedback by the efference copy of the motor command (Blakemore et al. 1998) was believed to be involved in the observed inhibitory modulation effect.

For the behavioral paradigms employing the DMS task, suppression of the M100 response to the second sound of the pair was observed for both simple sounds such as tones and tonal contours and complex speech sounds such as vowels and consonant-vowel syllables (Luo et al. 2005). In addition, experiments manipulating the duration of the delay period has demonstrated the correlation between the STM trace and the magnitude of the M100 response (Lu et al. 1992). This evidence suggested that task performance activated the involved cortical regions with a temporal order opposite to the habituation procedures. Task demands enter the network earlier than the stimulus perception: the expectation of the upcoming stimulus is actively selected from either STM or long-term memory (LTM) trace by corresponding task-specific cognitive functions. Thus, modulation of the evoked response can be highly dependent on the task demands, and can be observed independently from repetitive presentation of the same stimuli (Fritz et al. 2007).

Nevertheless, direct evidence was still absent to support the notion that the suppressive modulation of M100 found in DMS tasks has a specific correlation with the explicit memory processing other than the passive habituation effect.

In this study, by controlling the habituation effect with same timeline for each trial (a sound pair separated by a one-second silent delay period) and the attention effect by instructing subjects to listen to the sounds during both control and DMS conditions, we have demonstrated a suppressive modulation effect of the AER specifically correlated to performance of the DMS task, which involves overt STM processing and decision making based upon manipulation of the STM. Furthermore, the relatively greater suppression effect in the DMS task than the counting task not only strengthened the task-specificity of this effect, but also suggested that this effect is specifically related to the STM processing of the acoustic features of the sound stimuli, given that performing the counting task required the subject to hold a numbering format of the STM trace of the sound stimuli (Neider 2004, 2005).

In addition to the task-specificity, we also observed left lateralization and selectivity to TC stimuli of this modulation effect. Consistent to our findings, previous MEG studies have showed task-specific hemispheric asymmetry of the M100 response (Poeppel et al. 1996; Chait et al. 2004). Furthermore, a recent fMRI study also demonstrated that BOLD activation related to WM of frequency modulated (FM) tones was lateralized to the left auditory cortex (Brechmann et al. 2007), which was overlapped with the location of the significant ECDs observed in our study. For interpretation of this phenomenon, both hemispheric functional specificity (Grimm et al. 2006; Brechmann et al. 2005; Zatorre et al. 2002) and temporal scale sensitivity

(Poeppel et al. 2004; Boemio et al. 2005) were proposed. No matter whether it was due to the right auditory cortex's selectivity for the direction of frequency modulation (Brechmann et al. 2005), or its temporal sensitivity of the acoustic changes falling into the range of the stimuli used in this study, our finding of the asymmetric modulation to the auditory cortex is compatible with the hypothesis that the STM processing of the task-related stimuli suppressed the irrelevant processing in the left auditory cortex.

3.4.3 Functional interactions between brain regions underlie the task-specific modulation.

Consistent to our findings of the close relationship between the suppression of AER and performance of the DMS task, studies with impaired frontal patients showed correlated increasing of the AER magnitude and their behavioral deficit during performance of auditory DMS tasks (Chao & Knight 1998, Knight & Chao 1999), which also suggested the involvement of frontal regions as the sources of the observed suppression to AER. Furthermore, the DMS-specific suppression was to the AER of the second stimulus in the sound pair (Fig 3-4 b), which indicates that the neural dynamics during the delay period and the first 100 ms during presentation of the second sound were most likely behind this modulation effect. For the regions involved in STM processing during the delay period, previous studies have found both temporal lobe auditory (Gottlieb et al. 1989; Zatorre et al. 1991, 1994) and frontal lobe cognitive cortices (Fuster et al. 1971; Bodner et al. 1996; Levy et al. 2000; Kikuchi-Yorioka & Sawaguchi 2000), where the frontal regions, especially the prefrontal cortex (PFC), are believed to exert top-down influences to the sensory

cortices (Miller & Cohen 2001). Thus, analysis of the functional interaction between auditory cortex and frontal regions during the delay period should be able to provide information about the neural mechanism underlies the DMS-specific suppressive modulation of the AER.

As a measurement of the enhanced functional interaction, increased coherence values during the late delay period of the DMS task in various frequency bands was observed between several frontal regions and the left auditory cortex in this study. Among these regions, right inferior frontal gyrus (rIFG, Fig 3-4 D), left ventrolateral prefrontal cortex (vlPFC) and anterior superior temporal gyrus (aSTG, Fig 3-4 E) were showed in the frequency band of 20~30 Hz. In previous studies, multiple cognitive functions have been attributed to these regions. For instances, both vlPFC (Romanski & Goldman-Rakic 2002) and STG (Gottlieb et al. 1989) have been found involve in the memory maintenance of the object related information, where the corresponding oscillation during the delay period were found mainly in beta band around 20 Hz (Peterson et al. 2002; Leiberg et al. 2006b). In addition, vlPFC was believed to be correlated with selection of 'match' or 'non-match' rules (Roberts & Wallis 2000) for response. Furthermore, other cognitive functions such as inhibition of irrelevant memory retrieval (Aron et al. 2004) and interference information processing during performance of the working memory tasks (D'Esposito et al. 1999; Jonides et al. 1998) have also been correlated to regions in rIFG. Therefore, the cognitive functions such as STM maintenance and inhibitory control of memory retrieval should be involved in the observed DMS-specific suppression of the AER to upcoming stimuli.

The theoretical framework by Klimesch (Klimesch et al. 2007) postulated that EEG/MEG oscillation in lower frequency bands such as theta (4~8 Hz), and alpha (8~13 Hz) are correlated to STM demands, top-down inhibitory control processes, and STM/LTM interaction. Particularly, the interareal coherence in these frequency bands demonstrated patterns of frontal-posterior projection, and was believed to be correlated to inhibitory top-down control of the task-irrelevant processing (Schack et al. 2005; Von Stein et al. 2000). Consistent to this framework, in the frequency range of 2~20 Hz, our results demonstrated increased coherences between the left auditory cortex and frontal regions including ACC and bilateral premotor areas. Among these regions, ACC has been shown to be related to control of execution, particularly the competitive inhibition during selection of task appropriate responses (Pardo et al. 1990), while the motor regions were believed to involve in preparation of the correlated motor response. Previous supportive evidences of the correlation between these regions/functions and the modulation of AER included the studies that showed suppression of the M100 responses by listening to self-generated sounds as compared to passive listening to the external sounds (Martikainen et al. 2005; Houde et al. 2002), and a recent finding that rhythm-directed tapping increased the functional connectivity between premotor and auditory cortex (Chen et al. 2006). As to the underlying mechanism, the model of network memory postulated that the specific motor responses modulates the perception of the upcoming stimuli through the established associative motor-sensory efferent pathway in a competitive manner, where the associative selection of the information processing for the perceived stimulus and the motor responses was established through performance of the tasks

(Fuster 1997). Hereby, the results of the modulation of AER by ACC and pre-motor cortices should include inhibition of the irrelevant information processing pathway, which is consistent to our findings about the task-specificity of the suppressive modulation effect.

Interhemispheric inhibition between bilateral auditory cortices was found mainly in behavioral paradigms such as dichotic listening tasks (Brancucci et al. 2004) and sound localization paradigms (Marsat & Pollack 2005), to which the explicit competition of the attention resource between two ears was postulated. Our results demonstrated the increased functional interaction between the bilateral auditory cortex in the gamma band (30~50 Hz) in DMS task, which suggests that not only the explicit interhemispheric competition, but also the task-related implicit competition during auditory perception underlies the observed DMS-specific suppressive modulation effect. Moreover, this result further supports the notion of the hemispheric selectivity of sound features and suppression of task-irrelevant processing.

3.4.4 Neural network of the task-specific modulation effect

More experimental evidence supporting top-down modulation of auditory cortical activities and their task specificity were from studies using invasive recordings in animals (Fritz et al. 2005, Ohl et al. 2005), where more intricate patterns of the modulation effects were revealed. The modulation effects were mainly demonstrated by changes of the representational properties in both primary and secondary auditory cortical neurons after training the animals to perform certain tasks. For instance, the ferret primary auditory cortex showed different plasticity of its

receptive fields in detection and discrimination tasks (Fritz et al. 2002, 2005), to which recent experimental results suggested an important role of the top-down modulations from frontal regions (Fritz et al. 2007). Similarly, greater plasticity of the auditory space map in adult barn owl's optic tectum was observed when the animals were trained for actively hunting live mice as compared to being passively fed dead mice (Bergan et al. 2005); the top-down modulation from the forebrain was crucial to this behaviorally specific effect (Winkowski et al. 2006, 2007). Furthermore, primary auditory cortical neurons of Mongolian gerbils trained to perform a categorical discrimination task also displayed a performance related training effect with latency as early as 100 ms after stimulus onset (Ohl et al. 2005).

On the other hand, supporting evidence comes not only from auditory studies, but also from investigations of other sensory modalities. Stimulating the frontal eye fields (FEF) leads to modulation of V4, V2, and even the primary visual cortex in both animals (Armstrong et al. 2006) and humans (Ruff et al. 2006), where the modulation effects were similar to experimental results obtained from the studies manipulating spatial attention (Moran & Desimone 1985). Similar to the auditory domain, involvement of both ascending filtering based on saliency of the stimuli and descending modulation by task demands were observed in visual cortices, and the temporal sequence of recruiting the cortical regions depended on the experimental paradigm (Buschman & Miller 2007), where the task-specific frontal-posterior interactions were found in the frequency bands compatible to the findings of our study. Additionally, observations of the top-down modulation of evoked responses in primary and secondary somatosensory cortices were also obtained in studies using a

delayed discrimination paradigm (Hlushchuk & Hari 2006). Inhibitory feedback from frontal regions to primary and secondary somatosensory cortices was believed to play an important role for successful task performance (Miller & Wang 2006). Similar to our interpretation of the observed modulation in auditory domain, mutual inhibition between competitive processing of tactile information was modeled as the mechanism for discrimination (Machens et al. 2005).

It is believed that the top-down inhibitory modulation involves in the functions such as suppressing the task-irrelevant processing (Pfurtscheller & Neuper 1994), or synchronizing the functional neural network with phase reset among the involved regions (Klimesch et al. 1999, 2007). Multiple models have been proposed to interpret the top-down modulation of sensory processing and their correlation with the cognitive functions, such as executive control (Miller & Cohen 2001), predictive coding (Friston 2005), or the network of associative memory (Fuster 1997). Our findings of an increased functional interaction during the late delay period between the auditory cortex and frontal regions such as ACC and IFG supports the theory of executive control, whereas the involvement of vlPFC, aSTG, pre-motor regions, and the contralateral auditory cortex suggests more cognitive functions, such as the STM establishment, maintenance and retrieval, association of the established perception-action link, and interhemispheric competition also should be involved in the observed task-specific modulation effect. None the less, we would like to adapt the frame work of the ‘predictive coding’ theory (Friston 2005) to postulate the detail procedures of the modulation effect: Integration between the top-down prediction and bottom-up perception of upcoming acoustic events produces a code of ‘prediction error’ in

auditory cortex, which in turn determines the magnitude of AER. Most importantly, the prediction comes from the actively maintained STM trace within the task-specific memory network, rather than the automatic memory trace as postulated in the adaptation theory.

Generally, both enhancement of the task-relevant processing and suppression of the task-irrelevant responses have been found for the top-down modulation across sensory modalities (Frith & Dolan 1996). However, in this study, only a suppressive modulation effect was observed. This might due to the limit of the spatial resolution of the MEG method we applied, where the net effect integrated across multiple sources of modulation demonstrates a suppression effect at the spatial scale which can be detected by MEG. Therefore, further studies with control of either memory load or motor response can provide more knowledge concerning the aspects of the top-down modulation by each individual cognitive function.

3.4.5 Conclusion

The current study used the auditory DMS task to investigate the task-specificity of top-down modulation in human auditory cortex and the neural mechanisms underlying the observed modulation effects. Besides the demonstration of a DMS-specific suppressive modulation of the early phase auditory evoked responses, increased functional interaction between the modulated auditory cortex and frontal regions were also observed, which indicated the involvement of multiple cognitive functions such as STM processing, executive control and response preparation. Our results indicate that a task-specific interactive network including both auditory and frontal cortical regions is necessary for successful performance of

the auditory DMS task, where the frontal regions exert influences on the early phase of the primary and association auditory cortical processing, and the latency could be as early as tens of milliseconds after stimulus onset. Therefore, the findings from this study and previous studies suggest that the auditory perception in a noisy acoustic environment is accomplished by a task-specific and interwoven network, in which processing of the relevant auditory stimuli is usually enhanced and retained, and processing of the irrelevant stimuli is suppressed, where the relatively more broadly tuned suppression might cause the net effect as suppression of AER.

3.5 Isolating the functional signal in MEG measurements – categorization of M100 related independent components

In addition to the artifact rejection (section 3.2), I also used the method described in chapter 2 (Rong & Contreras-Vidal 2006), to isolate the M100 related MEG signals for analysis of the modulation effect in sensor space.

The noise-reduced MEG data were truncated into epochs that each one contained four trials for the task sessions and ten trials for the click counting session (see section 3.2 for detail description of the single trial epoch). Thus, there were 25 epochs for each task session (100 trials) and 20 epochs for each click-counting session (200 trials). In the task sessions, each epoch was a 273 x 8884 matrix of the noise-reduced MEG data; while in the click counting sessions, each epoch was a 273 x 6310 matrix of the noise-reduced MEG data. For each epoch, ICA was applied to compute the corresponding independent components (IC). Thus, for each task session, there were 6825 ICs (273 * 25 = 6825).

The M100 related ICs were then categorized in passive listening (PSL) and delayed-match-to-sample (DMS) datasets from a representative participant (participant #4): First, by taking the normalized magnetic field strength across the sensors at the peak latency of the M100 response observed in the averaged epoch of the click counting session (Fig. 3-8 A), two types of templates were determined by selecting the magnetic field at the peak latency of the M100 response as the scalp map for the template of 'AEP1' and its inversion as the scalp map for the template of 'AEP2'. Second, using each AEP template, the M100 related ICs were categorized in the click-counting dataset using the threshold-based categorization method without taking into account the dPxx features (thresholds for the features: dtopo = 0.4; H = 2.8; K = 30). The scalp and spectral maps of categorized ICs were then averaged to obtain the scalp map and spectral map of the template for each type of M100 related IC (Fig. 3-8 B). Third, using these templates, the M100 related ICs in PSL and DMS datasets were categorized and clustered using the threshold-based method (threshold for the features: dtopo = 0.4; dPxx=0.4; H = 2.8; K = 30). Fourth, using the categorized M100 related ICs, one MEG dataset was remapped for each task session (PSL_Tone: passive listening to Tones; PSL_TC: passive listening to TC stimuli; DMS_Tone: DMS task with Tones; DMS_TC: DMS task with TC stimuli). The auditory evoked field (AEF) and corresponding modulation index (MI) values were then calculated and analyzed using the methods described in section 3.2.

Visualization of the templates of AEP1 and AEP2 showed roughly opposite scalp maps and activation patterns at the latency of M100 response (the middle insets of Fig. 2-1 B), which suggested similar influences to the sensors by these two types of

ICs. In this dissertation they were treated as being correlated to same type of neuronal dynamics. The averaged scalp maps of the categorized M100 related ICs showed similar patterns to the templates (First column in Fig 3-9). In contrast, the averaged IC activation showed clearer peaks of the auditory evoked responses (Second column in Fig 3-9) than the templates (Second column in Fig 3-8 B), which confirmed the relationship between these categorized ICs and the neural dynamics underlies the M100 response. Comparison between the tasks showed that more ICs were clustered in the DMS conditions than the PSL conditions for TC stimuli but not for Tones (Table 3-1). Furthermore, the averaged IC activation showed that the categorized M100 related ICs in DMS task had weaker AER to S2 than PSL conditions (Fig 3-9 B). Further analysis of the remapped MEG using the M100 related ICs showed stronger suppressive modulation of the AEF to S2 in DMS task than in PSL conditions (Table 3-2).

The results showed that (1) In addition to the MEG dataset in the published results (attached paper, Rong & Contreras-Vidal 2006), this method also categorized and removed the artifactual ICs in a new MEG dataset collected from the experiment described in this chapter. Therefore, this method is applicable to MEG dataset collected from different scanners and different experiments; (2) the categorized M100 related ICs showed the M100 responses to the stimuli, similar averaged contour map to the templates, and differences in the averaged IC activation corresponding to task conditions. These results confirmed our prediction in the paper that this method can be also used in analysis of function-related ICs; and (3) The remapped MEG signals with the categorized M100 related ICs showed task-specific dynamics, which agrees

with the results from the auditory cortex. These results suggested that the categorized ICs are appropriate substrates for investigation of the task-related cognitive functions.

Table 3-1. Number of M100 related ICs that were categorized in each task session.

	PSL_Tone	**PSL_TC**	**DMS_Tone**	**DMS_TC**
AEP1	**308**	**302**	**320**	**457**
AEP2	**116**	**144**	**106**	**157**

Table 3-2. Modulation index values (%) computed from the remapped MEG signals using the M100 related ICs

	PSL_M *	**PSL_N**	**DMS_M**	**DMS_N**
Tone	**9.72**	**-6.04**	**21.10**	**-1.96**
TC	**2.31**	**4.54**	**16.08**	**12.80**

* The abbreviations are: PSL_M: Matched trials in passive listening task; PSL_N: non-matched trials in passive listening task; DMS_M: Matched trials in DMS task; DMS_N: non-matched trials in DMS task;

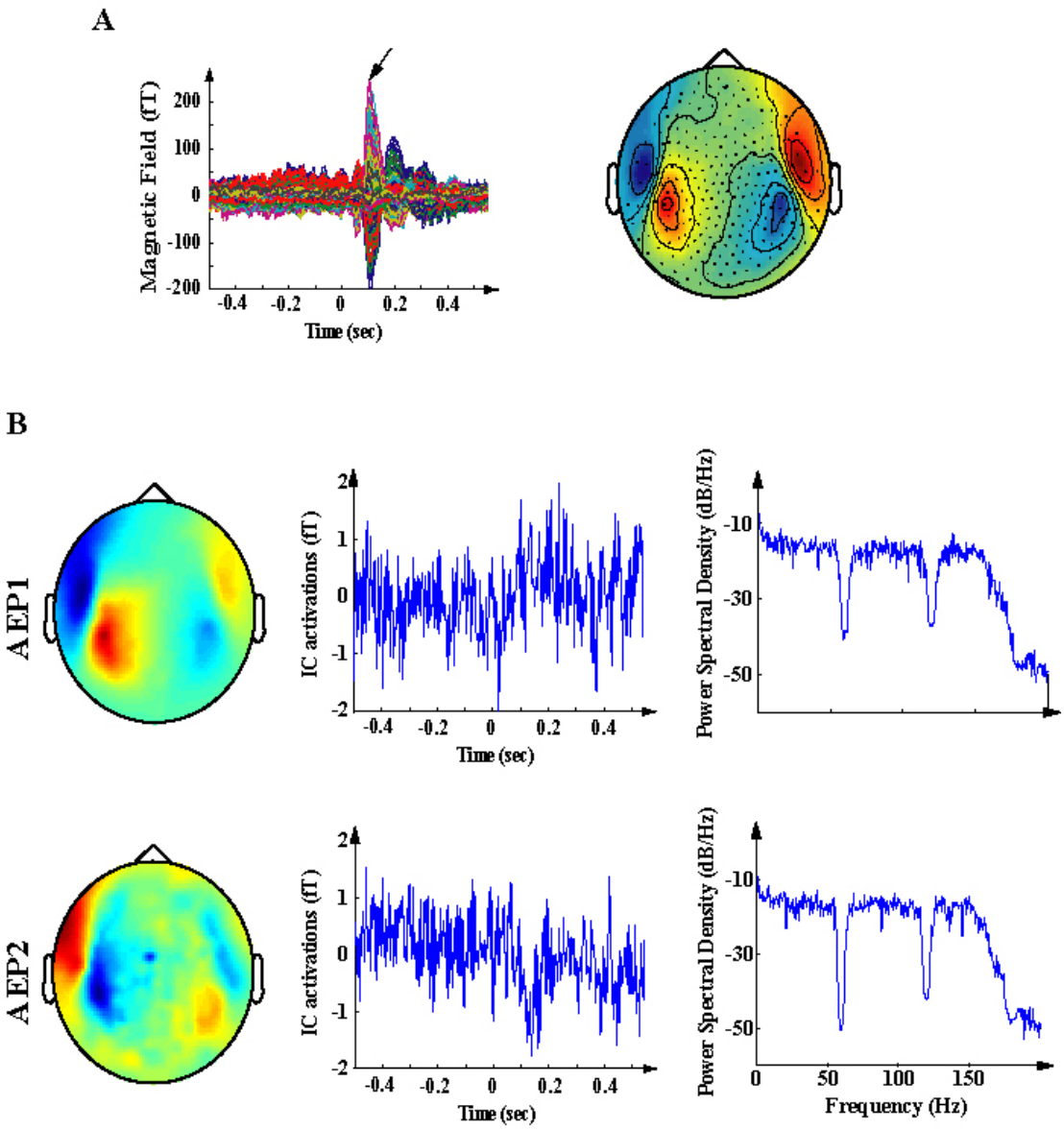

Fig. 3-8 Templates for identification of the M100 related independent components (IC). Data were collected in the click counting session performed by the participant #4 during the MEG recording (Chapter 3). (A) Left inset shows the averaged epoch of the auditory evoked field (AEF) across all sensors time-locked to stimulus onset. Black arrow indicates the peak of the M100 response. The right inset depicts the contour map of the AEF at the peak latency. (B) The templates of the M100 related ICs (as denoted by AEP1 and AEP2). The three columns are the scalp maps, the activations, and the spectral maps of the templates.

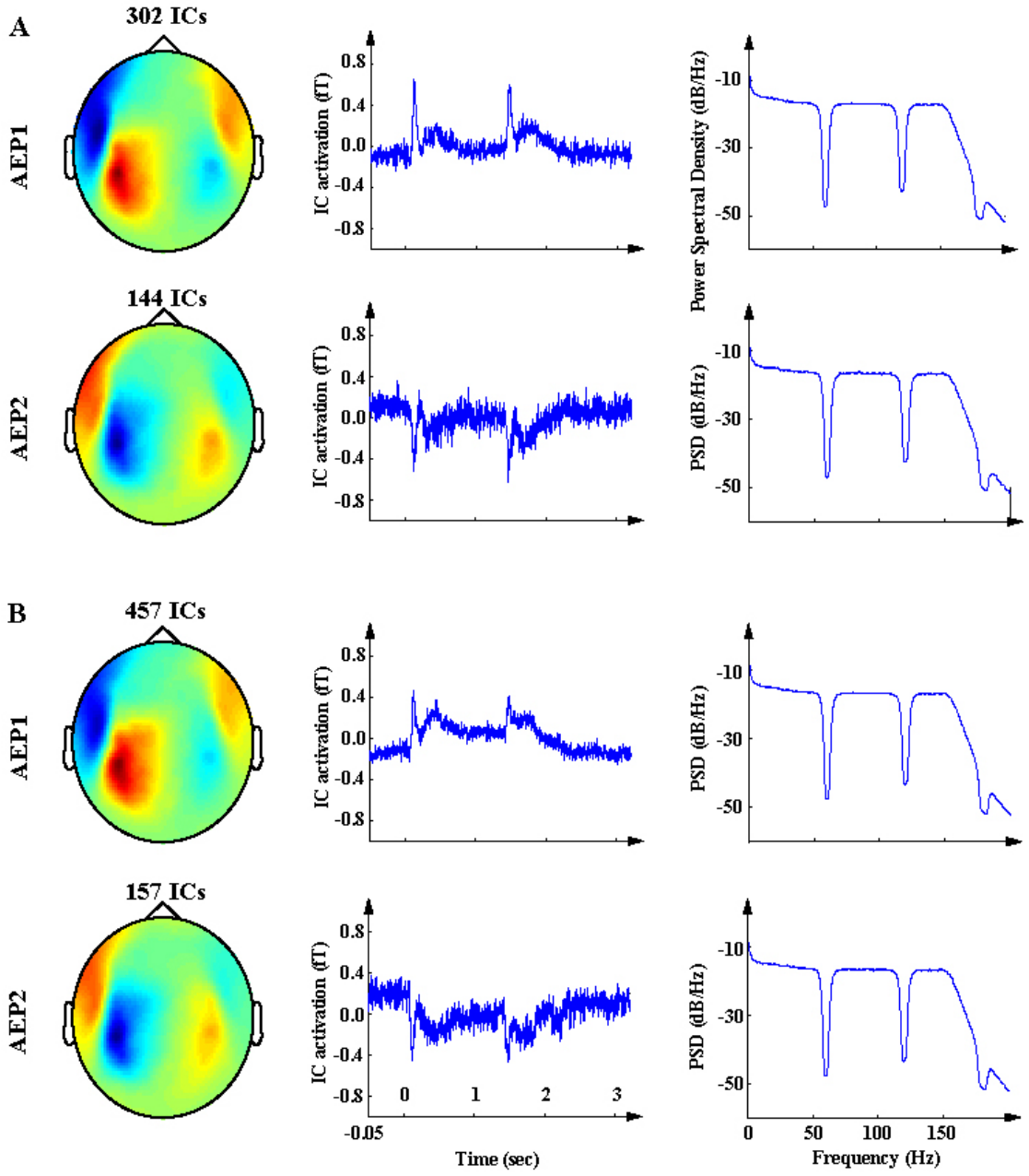

Fig 3-9 Identification results of the M100 related ICs. Data were from participant #4 in the MEG experiment (Chapter 3). (A) Averaged scalp maps, IC activations and spectral maps of the identified M100 related ICs in PSL_TC conditions. The upper row and lower row depict the identified ICs with template AEP1 and AEP2, respectively. (B) Averaged scalp maps, IC activations and spectral maps of the identified M100 related ICs in DMS_TC conditions.

CHAPTER 4: SIMULATING THE TASK-SPECIFIC COGNITIVE MODULATION OF HUMAN AUDITORY CORTICAL ACTIVITY USING A NEUROBIOLOGICALLY REALISTIC MODEL

A large-scale neurobiologically realistic neural network model of auditory object processing (Husain et al. 2004) is expanded to simulate the task-specific spatial-temporal neural dynamics correlated to performance of an auditory delayed-match-to-sample (DMS) task comparing to passive listening (PSL) conditions. The expanded model has two parallel subsystems to simulate the cortical networks processing the task-related sound stimuli and task-irrelevant background noise, respectively. Each subsystem is composed of the same temporal auditory and frontal cognitive regions, as well as the feedforward and feedback connections between the regions that link them together for successful task performance. Important to our purpose in this study, the cross subsystem top-down inhibitory connections between the specific memory processing units and the non-specific auditory units simulate suppression of the task-irrelevant processing. Furthermore, using the synthetic integrated synaptic activity (ISA) in each region as inputs, we simulate the corresponding MEG and fMRI signals with our forward models. Our results show DMS-specific suppression of the auditory evoked responses (AER) obtained from both ISA in auditory regions and MEG signals on sensors that agreed with the experimental findings in chapter 3. In addition, forward simulation of fMRI produced DMS-related signal change of the BOLD signal comparable to the experimental results. Therefore, these results support our hypothesis that the proposed modeling

approach is capable of bridging the knowledge about the task-related neural dynamics obtained with techniques that are sensitive to different types of signals and different temporal and spatial scales.

4.1 Introduction

Previous empirical observations have shown both task-specific enhancement and suppression of the auditory cortical activity during performance of the auditory DMS task and other similar short-term memory (STM) tasks. In animal studies, co-existing enhancement of task-relevant and suppression of the task-irrelevant auditory responses were observed correlated to corresponding behavioral rules and context of perceived stimulus (Goettlieb et al. 1989, Ohl et al. 2001, Fritz et al. 2005). In humans, fMRI and MEG experiments demonstrated opposite patterns regarding the DMS-specific auditory cortical activity. In fMRI studies, performing the DMS task related to increases in BOLD signal in the auditory cortices (Grady et al. 1997, Husain et al. 2004) compared to the passive conditions. In MEG/EEG studies, performing the auditory DMS task demonstrated suppression of the evoked responses in auditory cortex (Rämä et al. 2000, Lu et al. 1992, Luo et al. 2005; also see our results in Chapter 3). Furthermore, the extent of the BOLD signal enhancement (Brechmann et al. 2007) or evoked response suppression (Lu et al. 1992) was positively correlated with the performance level and memory manipulation. Because of these, it is necessary to find an approach which combines these seemingly discrepant experimental results obtained by different methods, in order to find a consistent understanding of the underlying physiological process.

Modeling has been proposed as one of the approaches for integrating MEG and fMRI data (Horwitz & Poeppel 2002), where the postsynaptic potential (PSP) can serve as the common link since the relationship of PSPs with MEG (Hämäläinen et al. 1993, Baillet et al. 2001) and BOLD (Logothetis et al. 2000, Logothetis 2001, 2002, 2003) signals has been intensively investigated. Recent studies have introduced multiple models to simulate the ERP/ERF (David et al. 2006), fMRI (Tagamet & Horwitz 1998, Husain et al. 2004) or both (Babajani et al. 2005, Riera et al. 2004, 2005) to incorporate the activity in multiple regions. Specifically, models have been developed to simulate correlated regional neuronal activities and fMRI signals during performance of the DMS task (Tagamet & Horwitz 1998, Husain et al. 2004, Deco & Rolls 2005, Chadderdon & Sporns 2006).

In this chapter, we combine an expanded version of a large-scale neural network model of auditory object processing (Husain et al. 2004) with MEG and fMRI forward models to simulate the DMS-specific event-related responses and BOLD signals. In this model, two parallel subsystems are included to simulate the neuronal groups that involve in performance of the auditory DMS task (specific part) and the neuronal groups that correlate to task-irrelevant processing (non-specific part), respectively (Horwitz et al. 2005). For each subsystem, both temporal auditory and frontal cognitive regions are simulated, where the different tasks are determined by different gain values (‘attention’) to the frontal memory units during the presentation of the stimuli and delay period. Furthermore, the connections from the frontal memory processing units to the superior temporal region and secondary auditory cortices in the specific part simulate the distributed network of the STM

maintenance and top-down enhancement of the task-relevant auditory activity correlated to task-performance; whereas the top-down inhibitory projections from the specific memory processing units to the non-specific auditory regions simulate the top-down suppression of the task-irrelevant auditory pathways. Simulation with this model provides synthetic neuronal activity and integrated synaptic activity (ISA) in each region. We then use the synthetic regional ISA for further simulation of the MEG and fMRI signals with forward models, where the inhibitory PSP (IPSP) were integrated separately to the excitatory PSP (EPSP) between the MEG and fMRI simulations. Calculation of the regional ISA for MEG simulation uses the vector sum of the PSPs, where the IPSP magnitudes were subtracted from the EPSP magnitudes. Computation of the regional ISA activity for simulation of fMRI signal integrates the magnitudes of IPSP and EPSP; hence the IPSP contributes to the instantaneous increase of BOLD signal in fMRI simulation (Tagamets et al. 2001; Logothetis 2003).

We hypothesize that with the proposed modeling approach, we can simulate the DMS-specific suppression of AER and BOLD signal changes simultaneously, where the relative greater inhibition of the specific memory units to the non-specific auditory regions during the DMS task can account for the patterns of neural activity that have been observed in neuroimaging experiments.

4.2 Materials and Methods

4.2.1 The neurobiologically realistic large-scale neural network model

Computational neural model

Simulation of the neuronal activity in human cortical regions related to the task performances in this study is based on an expansion of a large-scale neurobiologically realistic network model for auditory object processing (Husain et al. 2004). The expanded model (Horwitz et al. 2005) includes duplicated 'specific' and 'non-specific' subsystems (Fig. 4-1A). The specific subsystem is correlated to the task-relevant processing of the tested acoustic stimuli (Tones and Tonal contours), whereas its non-specific counterpart processes background noise. The structure of each subsystem is adapted from the original model, which consists of five regions that roughly simulates the medial geniculate nucleus (MGN), the primary (Ai) and secondary (Aii) auditory cortices, the superior temporal (ST) regions, and the prefrontal cortex (PFC), respectively. Following the architecture in the original model, each region is composed of sub-modules that reflect a characteristic physiological function, and each sub-module consists of 81 basic units that have same parameters of neuronal activity and internal connection strengths (see detailed description in Husain et al. 2004 and Tagamet and Horwitz 1998). For each subsystem, MGN is the input stage with one sub-module, within which each unit represents a filter with a characteristic frequency (CF). Ai contains two sub-modules with selectivity of either the upward frequency modulated (FM) sweeps (Aiu) or the downward FM sweeps (Aid), within each sub-module the units receive tonotopic

inputs from the corresponding MGN units. Moreover, in each of the Ai sub-modules the selectivity of FM sweeps are obtained by lateral inhibitory connections between the units such as that the upward selection is materialized by stronger inhibition to the units with lower CF, and the downward selection is obtained by stronger inhibition to the units with higher CF. Therefore, the Ai region simulates two functions of the core and belt auditory cortices: the response to the CF by each unit and the selectivity to the FM sweep by the sub-modules. Aii is composed of three functional sub-modules with longer integration time window than the units in Ai, two of them have the same architectures and FM sweep selectivity to Aid and Aiu (Aiiu and Aiid, respectively) and receive tonotopic inputs from the corresponding Ai units. The other one has contour-selectivity – the selectivity to direction change of the sweeps (Aiic) -- and integrates the inputs from both Aid and Aiu. ST has one sub-module that integrates the inputs from all three sub-modules in the Aii region, which models the abstract representation of sound stimuli. The PFC region consists of four sub-modules (C, D1, D2, and R) that simulate the short-term memory (STM) and decision making related functional neuronal groups in the frontal cortical areas, in which the 'cue-sensitive' units (marked as 'C' in the figure 4-1 A) responds to the inputs from ST, the 'D1' delayed response units correspond to the neurons displayed increased activity during the delay period of the DMS task (Romanski et al. 1999), the 'D2' delayed response units simulate the neurons that showed increased activity in both delay period and the time windows of stimuli presentation, and the 'response' units demonstrate increased activity for the 'match' condition in the DMS task and represent the frontal decision making regions during the corresponding task performance. Additionally, each

subsystem also contains an 'attention' unit, which provides a gain control to each of the 'D2' units to simulate the modulation of the STM processing within each task condition.

As the basic functional processing ensemble in this modeling structure, each unit (Fig. 4-1B) is composed of an excitatory element and an inhibitory element. First introduced by Wilson & Cowan (1976), this type of configuration models a simplified cortical column, in which the excitatory element represents integrated activity of the excitatory pyramidal neurons and the inhibitory element represents activity of the inhibitory interneurons in the column. Principally, the excitatory and inhibitory activity in each basic unit follows the sigmoidal rule (Husain et al. 2004; Tagamet & Horwitz 1998):

$$\frac{dE_i(t)}{dt} = \Delta\left(\frac{1}{1+\exp(-K_E[w_{EE}E_i(t) + w_{IE}I_i(t) + in_{iE}(t) - \tau_E + N(t)])}\right) - \delta E_i(t) \quad (4\text{-}1)$$

$$\frac{dI_i(t)}{dt} = \Delta\left(\frac{1}{1+\exp(-K_I[w_{EI}E_i(t) + in_{iI}(t) - \tau_I + N(t)])}\right) - \delta I_i(t) \quad (4\text{-}2)$$

Where $E_i(t)/I_i(t)$ and τ_E/τ_i denote the electrical activities at time t and the input thresholds of the excitatory and inhibitory elements in the ith basic unit, respectively; K_E and K_I represent the steepness of the corresponding sigmoidal functions; Δ is the rate of change; δ is the decay rate; N(t) simulates the spontaneous Gaussian distributed background activity; and w_{EE}, w_{EI} and w_{IE} are the recurrent excitatory-excitatory, excitatory-inhibitory, and inhibitory-excitatory connection weights within a unit, respectively. In addition, $in_{iE}(t)$ and $in_{iI}(t)$ are the total external inputs to the excitatory and inhibitory elements at time t:

$$in_{iE}(t) = \sum_j w_{ji}^E E_j(t) + \sum_j w_{ji}^I I_j(t) \quad (4\text{-}3)$$

$$in_{iI}(t) = \sum_k w_{ki}^E E_k(t) + \sum_k w_{ki}^I I_k(t) \quad (4\text{-}4)$$

in which w_{ji}^E / w_{ji}^I or w_{ki}^E / w_{ki}^I are the weights of the excitatory and inhibitory inputs from an external source j or k to the excitatory or inhibitory element in the ith unit, respectively. The electrical activities of the elements are set between 0 and 1 and can be viewed as the proportion of activated neurons in the local population represented by this unit. The parameters of the basic unit elements in each region are from the original model and are identical for both subsystems. Table 4-1 lists these values (replicated from table 1 of Husain et al. 2004).

Besides the simulation parameters of the basic units, the response properties of each region were also determined by the intraregional and interregional connections. For example, alignment of the intraregional lateral inhibitions between the units in Ai and Aii regions determines the selectivity of upward, downward and contour-pattern sweeps of the sub-modules. The upward selective units have inhibitory connections to the adjacent lower frequency counterparts, while the downward selective units have inhibitory connections to the higher frequency units. The intraregional inhibitory connections in the contour-selective units are bilateral. Being simulated in the same way across the whole model, the lateral inhibitions between the units are represented by excitatory projection from the excitatory elements in the source units to the inhibitory elements in the target units. In this method, the connection weights are aligned in a Gaussian manner with weaker connections to distant ones in Ai and Aii regions (Fig. 4-1 C). In addition to the

intraregional connections, interregional connections simulate the feedforward and feedback connectivity between the corresponding cortical areas. Among them, all feedforward connections are excitatory, whereas the recurrent and feedback connections are either excitatory or inhibitory (Fig 4-1 A). Particularly, the D2 → ST, D2 → Aii and ST → Aii excitatory feedback connections within the specific subsystem simulate their involvement in the maintenance of the STM trace (Pasternak & Greenlee 2005). In contrast, the feedback inhibitory projections from the specific D2 units to the non-specific Ai and Aii regions simulate the top-down inhibitory modulation of the task-irrelevant auditory information processing. In this manner, the interregional feedback connections simulate both the strengthening of the task-specific processing of the relevant acoustic stimuli and the suppression of the back-ground noise processing in the task-irrelevant pathway. Similar to the intraregional inhibition, the inter-regional inhibition is accomplished by excitatory projections from the source excitatory elements to the target inhibitory elements. In addition to the within system connections and those cross-system inhibitory connections depicted in figure 4-1 A, potential connections were pooled between every unit in the specific and non-specific subsystems. In each simulated trials, 50% of these potential connections were randomly activated to simulate the noisy communication between the neuronal groups. Table 4-2 listed the weights of the intraregional and interregional connections within each subsystem (Values are replicated from table A1 and A2 in Husain et al. 2004). Table 4-3 listed the weights of the cross-subsystem connections between the units.

Simulation protocol

In this study, we use different protocols for simulations of MEG and fMRI signals to make them compatible to the experimental measurements. Consistent with the MEG experiment illustrated in chapter 3, modeling of the MEG signal applies an event-related design. In this design, two types of tasks are simulated in two separate sessions, where the task type is determined by the 'attention' gain value to specific D2 units there is a corresponding attention gain value during stimuli presentation and the delay period. The passive listening (PSL) task uses a lower value (0.05), whereas a higher value (0.15 for tones, 0.30 for tonal contours) is set for the delayed-match-to-sample (DMS) task. The stimuli (Fig. 4.2A) included pure tones (Tone, 70 time steps in duration, represented by activation of two MGN units throughout) and tonal contours (TC, 70 time steps in duration, represented by two 25 time steps FM sweeps interleaved by a 20 time steps tone). Each simulation session consists of 20 consecutive trials (10 for each type of stimuli) with the same task condition (PSL or DMS). Each trial contains a baseline period of 100 time steps, followed by a pair of stimuli (S1 and S2, respectively) separated by a 200 time steps delay period, and a 300 time steps inter-trial-interval (ITI) (Fig. 4.2B). Each time step corresponds to 5 ms in the experimental condition. For the baseline, delay and ITI periods, input to the system includes only random noise to the non-specific part, whereas during the time windows of stimuli presentation, both tested stimuli and noise were input to the specific and non-specific parts, respectively. Within each simulation, match (identical sounds in the pair) and non-match (different sounds in the pair) trials with either Tone or TC stimuli were randomly mixed and counter-balanced. Therefore, each simulation

session has 5 trials for each trial type (match or non-match) by sound type (Tone or TC) combination.

For the simulation of fMRI signal, each simulation session is composed of a 'task' block and a 'control' block for one type of sound stimuli (Tones or TC). These conditions correspond to the blocks of the DMS and Rest conditions in the experiment (Husain et al. 2004), respectively. Each block contains three trials, and each trial had the same timeline to the ones used in simulation of the MEG signal. The three trials in each block followed the order of 'match' → 'non-match' →'match'. Also similar to the MEG simulation, during the 'task' trials, inputs to the specific part were test stimuli with a certain pattern resembling either Tones or TC during the time window of stimuli presentation, while inputs to the non-specific part resemble the background noise. In contrast, for the 'control' trials, the inputs to both specific and non-specific parts were random noise. In addition, the attention gain values to the D2 units in the specific part were set to either higher (0.30, 0.29, 0.28, 0.27, 0.26) values during the stimulus presentation and delay period of the 'task' trials to simulate the virtual DMS task or lower (0.05) values in the 'control' tasks to simulate the Rest condition, respectively. For the non-specific part D2 units, the gain value is 0.20 during presentation of stimuli, and 0.10 during the baseline, delay period and ITI.

4.2.2 Simulation of ECD, MEG and BOLD signals

Further simulation of brain imaging signals depends on integration of the simulated post-synaptic activity across the basic units for each region, where the algorithms and time windows of integration are different from MEG to fMRI. For

each unit, the post-synaptic activity is represented by summation of the weighted inputs, and integration of the post-synaptic activity across the units in each region produces the integrated synaptic activity (ISA). The ISA of the simulated regions are then applied to the forward models to simulate either MEG or fMRI signals.

Simulation of the source activity and sensor space MEG signal

For simulation of MEG, the integrated synaptic activity (ISA) of each unit is computed by summing up the weighted inputs to the excitatory element, where the summation is taken for every time step:

$$ISA_{MEG,\,i}(t) = w_{EE}E_i(t) + w_{EI}E_i(t) + w_{IE}I_i(t) \qquad (4\text{-}5)$$

It should be noted that in above equation the weighted inhibitory input is integrated with a negative sign to the excitatory counterparts (David & Friston 2003). The computed ISA values are then integrated across the specific and non-specific sub-modules for each region to represent the moment strength of the equivalent current dipole (ECD) that locates in this region. These simulated ECD moment values are then input into the MEG forward model (Appendix A, Huang et al. 1999) for further simulation of the sensor space MEG signals, where other parameters for the forward simulation are obtained from the experimental study described in Chapter 3: The orientation of the ECDs and source-sensor relationship denoted as the lead fields are determined by the experimental measurements from a representative participant (participant #4), and the location of the ECDs are adapted from the original model for each corresponding region (Table 4.4, adapted from the table 2 in Husain et al. 2004). Four ECDs are used for forward simulation of the sensor space MEG signal while the activity of each ECD are from the corresponding simulated region: the ECD locates at

primary auditory cortex is simulated by Ai, the ECD locates at secondary auditory cortex is modeled by Aii, the ECD locates at anterior superior temporal gyrus is simulated by ST, and the ECD locates at prefrontal cortex is simulated by integrated ISA across the four regions in PFC.

Simulation of the BOLD signal

In contrast to simulation of MEG signal, by assuming that the increases of both excitatory and inhibitory activity contribute to the instantaneous increase of regional cerebral blood flow (rCBF) and BOLD signals (Tagamets and Horwitz, 1998; Horwitz and Tagamets, 1999; Logothetis 2003), the ith unit's ISA for simulation of BOLD signals is computed by integrating the weighted inputs to both excitatory and inhibitory elements. The integration is computed by every 10 time steps to accommodate the experimental temporal resolution of the fMRI measurements.

$$ISA_{fMRI,\,i}(t) = w_{EE}E_i(t) + w_{EI}E_i(t) + \left|w_{IE}I_i(t)\right| + \sum_{k,i} w_{ki}E_k(t) + \sum_{m,i}\left|w_{mi}I_m(t)\right| \qquad (4\text{-}6)$$

The simulated BOLD signal for each region is then computed by convolving the integrated ISA with a Poisson distribution function $h(t)$, which represented the hemodynamic response function mediating the integrated synaptic activity and the fMRI signals (Logothetis et al. 2001, Friston et al. 1994, Horwitz & Tagamets1999).

$$fMRI(t) = \int \sum_{i,t} ISA_i(t-\tau)h(\tau)d\tau \qquad (4\text{-}7)$$

in which the integrated time interval for each simulated fMRI signal was 3 sec, which equals to the scan time (TR) in the fMRI experiment (Husain et al. 2004). Futhermore, the hemodynamic response function $h(\tau)$ is

$$h(\tau) = \frac{\lambda^{\tau} e^{-\lambda}}{\tau!} \tag{4-8}$$

where τ was the delay time, and the parameter λ characterized the width and height of $h(\tau)$.

4.2.3 Analysis of the simulation results

The simulated source ECD activity, sensor space MEG signal, and fMRI signals were analyzed in similar ways to the corresponding experimental measurements to test the hypothesis that with the same modeling architecture and parameters for simulation of neuronal activity and functional connectivity, we can simultaneously replicate the findings in experimental MEG and fMRI studies correlated to task-specific cognitive modulation of the human auditory cortex.

Analysis of the simulated MEG signal in both source and sensor spaces

The integrated ISA of Ai and Aii regions were summed up for each time step to simulate the corresponding neuronal activity index of the representative ECD in auditory cortex. Since during the simulation, each time step corresponds to 5 ms in experimental condition, the simulated single-trial auditory ISA was interpolated to fit the timeline of the trials in the experiment. Therefore, for each trial, the simulated auditory source activity was a 1x2220 vector, which corresponded to a 3.7 second epoch with the sampling frequency of 600 Hz. Consistent with the experimental results, this epoch includes a 0.5 second baseline, two 0.35 second time windows corresponding to the presentation of S1 and S2, a one second delay period between two stimuli, and a 1.5 second inter-trial interval (ITI). For each task * trial type * sound type condition, an averaged epoch was obtained by taking the means across the

interpolated simulated auditory activity of the five corresponding trials. The magnitude of the auditory evoked response (AER) to each stimulus was computed as the peak simulated auditory activity value with latency ~100 ms after the stimulus onset. Modulation index (MI) values were calculated in the same way that I calculated the MI values from the representative source ECDs in experiment (see section 3.2 for detail) using the simulated AER values and simulated auditory ISA during the baseline period.

Similarly, in sensor space, computation of the evoked responses and the modulation index (MI) values with the simulated MEG signal follows the same methods used in analysis of the experimental MEG signals. Only the left representative sensors from participant #4 are used to calculate the MI values taking into account the task-related hemispheric asymmetry found in experimental data. Two types of simulation for the sensor space MEG signal were conducted. First, only the ECDs in Ai and Aii regions are used as inputs to the forward model to simulate the constrained influence of the auditory cortical activity to the magnetic field, which is correspondent to the remapped MEG signal using the M100 related ICs (see chapter 2 for the detail method of categorizing the ICs and remapping of the MEG signal). Second, all four ECDs are used as inputs to the forward model, which is used to simulate the integrated influence by all the sources to the magnetic field and corresponds to the RMS values computed from the raw MEG signals in experimental condition;

Analysis of the simulated BOLD signal

Using the simulated fMRI signals, the percent signal change (PSC) values are computed using the same methods from the experimental analysis (Husain et al. 2004) to assess the DMS-specific BOLD changes. (1) the averaged BOLD signal across the simulations are first calculated for the two task conditions (PSL and DMS), the stimuli (Tones and TC), and the rest condition, so one averaged value is obtained by taking the means across the block for each task * sound type condition to match the experimental analysis; (2) the averaged BOLD signal for each region is normalized by the Rest condition to obtain the values of nTC [nTC = (TC _Rest)/Rest] and nTones [nTones = (Tones _ Rest)/Rest)]; and (3) the PSC value is computed by calculating the signal change of nTC relative to nTones [PSC = (nTC _nTones)/nTones]. In this study, we compared the simulated PSC values to experimental findings, in which the signal change is greater for TC than for Tones in DMS task (Husian et al. 2004).

Table 4-1 Parameters for the sigmoidal functions that determine the neuronal activity of the excitatory and inhibitory elements in the basic units of each sub-module [(1)].

	Units	Δ	δ	K	τ	$N(t)$
Excitatory elements	Aiu, Aid	0.7	0.7	8.0	0.30	0.05
	Aiiu, Aiid	1.7	1.7	9.0	0.35	0.10
	Aiic	1.3	1.3	8.0	0.34	0.10
	ST	0.8	1.2	7.5	0.35	0.10
	PFC-C	0.5	0.5	9.0	0.30	0.05
	PFC-D1	0.5	0.5	9.0	0.30	0.05
	PFC-D2	0.5	0.5	9.0	0.30	0.05
	PFC-R	0.89	1.0	9.0	0.30	0.05
Inhibitory elements	Aiu, Aid	2.0	1.0	17.0	0.20	0.05
	Aiiu, Aiid	0.2	1.6	18.0	0.35	0.10
	Aiic	0.2	0.8	17.0	0.30	0.10
	ST	1.0	1.0	19.0	0.30	0.10
	PFC-C	0.5	0.5	20.0	0.10	0.05
	PFC-D1	0.5	0.5	20.0	0.10	0.05
	PFC-D2	0.5	0.5	20.0	0.10	0.05
	PFC-R	0.5	0.5	20.0	0.10	0.05

(1). the table was replicated from table 1 in Husain et al. 2004 for the reader's convenience.

(2). the parameters are applied to equations (4-1) and (4-2).

(3). see text for the detail description of the abbreviations.

Table 4-2 Intraregional and interregional connections among the units for each subsystem (E→E connections unless specified) [(1)].

From	To	Fan out	Mean value and variability	Percent to create [(2)]	Net total afferents	Comments
MGN	Ai	1 → 3	1 @ 0.05 ± 0.003 1 @ 0.10 ± 0.002 1 @ 0.0 ± 0.002	100 1D → 1D	0.06	Highest value in the center, values oriented either descending or ascending
Ai	Ai	1 → 9	4 @ 0.0 ± 0.0 2 @ 0.05 ± 0.0 1 @ 0.15 ± 0.0 1 @ 0.25 ± 0.0 1 @ 0.35 ± 0.0	100 1D → 1D	0.8	Inhibitory connections that oriented either descending (Aiu) or ascending (Aid), see text and Fig. 4.1 C for detail
Ai	Aii	1 → 3	1 @ 0.05 ± 0.01 1 @ 0.1 ± 0.01 1 @ 0.0 ± 0.0	100 1D → 1D	0.15	Weights oriented either descending or ascending
Ai	Aiic	1 → 3	2 @ 0.05 ± 0.01 1 @ 0.1 ± 0.01	100 1D → 1D	0.15	Highest value in the center
Aii	ST	1 → 5	5 @ 0.08 ± 0.002	100 1D → 2D	0.4	
ST	PFC-C	1 → 1	1 @ 0.02 ± 0.002	100 2D → 2D	0.2	
PFC-D2	Aii	1 → 5	5 @ 0.0014 ± 0.0007	100 2D → 1D	0.007	
PFC-D1	ST	1 → 1	1 @ 0.03 ± 0.001	100 2D → 2D	0.03	Inhibitory connections
PFC-D2	ST	1 → 1	1 @ 0.01 ± 0.002	100 2D → 2D	0.01	
ST	Aii	1 → 4	4 @ 0.00125 ± 0.0006	100 2D → 1D	0.005	
PFC-C	PFC-D2	1 → 1	1 @ 0.07 ± 0.0		0.07	
PFC-C	PFC-R	1 → 1	1 @ 0.05 ± 0.0		0.05	
PFC-D1	PFC-R	1 → 1	1 @ 0.06 ± 0.0		0.06	
PFC-D1	PFC-D2	1 → 1	1 @ 0.105 ± 0.0		0.105	
PFC-D2	PFC-D1	1 → 1	1 @ 0.10 ± 0.0		0.10	
PFC-D1	PFC-C	1 → 1	1 @ 0.02 ± 0.0		0.02	Inhibitory connections
PFC-C	PFC-D1	1 → 1	1 @ 0.05 ± 0.0		0.05	Inhibitory connections
PFC-R	PFC-D1	1 → 1	1 @ 0.03 ± 0.0		0.03	Inhibitory connections
PFC-R	PFC-D2	1 → 1	1 @ 0.065 ± 0.0		0.065	Inhibitory connections

(1). the values are adapted from table A1 and A2 in Husain et al. 2004.

(2). this parameter indicates the percentage of the connections that has been activated, and the connection pattern between the sub-modules (1D: one-dimensional; 2D: two-dimensional).

(3). See text and Fig. 4-1 A for the detail illustration.

Table 4-3 Cross subsystem connections.

From	To *	Fan out	Mean value and variability	Net total afferents	Comments
Specific PFC-D2	Non-Spec Ai	1 → 81	81 @ 0.0005 ± 0.00025	0.0405	Inhibitory connections
Specific PFC-D2	Non-Spec Aii	1 → 81	81 @ 0.0005 ± 0.00025	0.0405	Inhibitory connections
All other potential cross subsystem connections		1→5	5 @ 0.0002 ± 0.0001	0.001	Excitatory or inhibitory

* The connections are to all sub-modules in the target region.

Table 4-4 Location of source ECD in forward simulation of sensor space MEG signals [1].

Region [2]	**Tx** [3]	**Ty**	**Tz**
Ai	-45	-31	15
Aii	-59	-26	10
aSTG	-59	-17	4
PFC	-54	9	8

(1). the values are adapted from table 2 in Husain et al. 2004.

(2). only regions in left hemisphere were simulated to accommodate the left hemisphere specificity of the observed DMS-specific effect in experiment.

(3). locations are in Talairach (Talairach & Tournoux 1988) coordinates with the unit of millimeter (mm).

Fig 4-1. (A) Diagram of the network model. The model is composed of two duplicated subsystems (parts). Each part consists of same regions (MGN, Ai, Aii, ST, and PFC). Region MGN has one sub-module; region Ai consists of one upward-sweep selective (Aiu) submodule and one downward-sweep selective (Aid) sub-module; in region Aii, besides the upward-sweep (Aiiu) and downward-sweep (Aiid) selective sub-modules, there is also a contour-selective sub-module (Aiic); region ST has one sub-module and; region PFC consists of one cue-sensitive (C), two delay (D1 and D2), and one response (D) sub-modules. Each sub-module is composed of 81 basic units. For both parts, the MGN region represents the input stage of the model, in which the basic units are aligned tonotopically and each unit is sensitive to one simulated characteristic frequency. In specific part, the MGN activity simulates patterned sound stimuli (Tones or tonal contours), whereas in non-specific part, the MGN activity simulates the environmental noise. The arrows depict connections between regions, in which the blue arrows indicate the excitatory connections (excitatory elements to excitatory elements) and the red arrows indicate the inhibitory connections (excitatory elements to inhibitory elements) within each part, respectively. The fixed inhibitory connection from the specific D2 units to the non-specific Ai and Aii units are represented by green arrows (potential cross-subsystem connections are not illustrated here). See text for detail description of the model. (B) A basic unit in the model. Each basic unit consists of one excitatory and one inhibitory element. The arrows depict the external and internal connections with the same color codes in (A). The percentile value on each arrow denotes the weight strength of the connection, which reflects the proportion of synaptic connections made between these elements. (C) Alignment of the basic units and intraregional lateral connections in the Aid sub-module. The units were aligned from left to right with increase of characteristic frequency (CF), where the excitatory and inhibitory elements are represented by blue and red ellipses, respectively. The arrows denote the connections between elements with the same excitatory/inhibitory color codes. Each Aid unit inhibits the higher CF

neighbors via excitatory connections from its excitatory element to the neighbor's inhibitory elements. The weights of these intraregional inhibitory connections decayed in a Gaussian manner with longer distance. In contrast, no inhibition is placed onto the neighbor units with lower CF. Similar alignment and connections were used in the Aiu sub-module with a reversed pattern of the lateral inhibitory connections. Both (B) and (C) were replicated from Husain et al. 2004 (Fig 1 b and Fig A1, respectively).

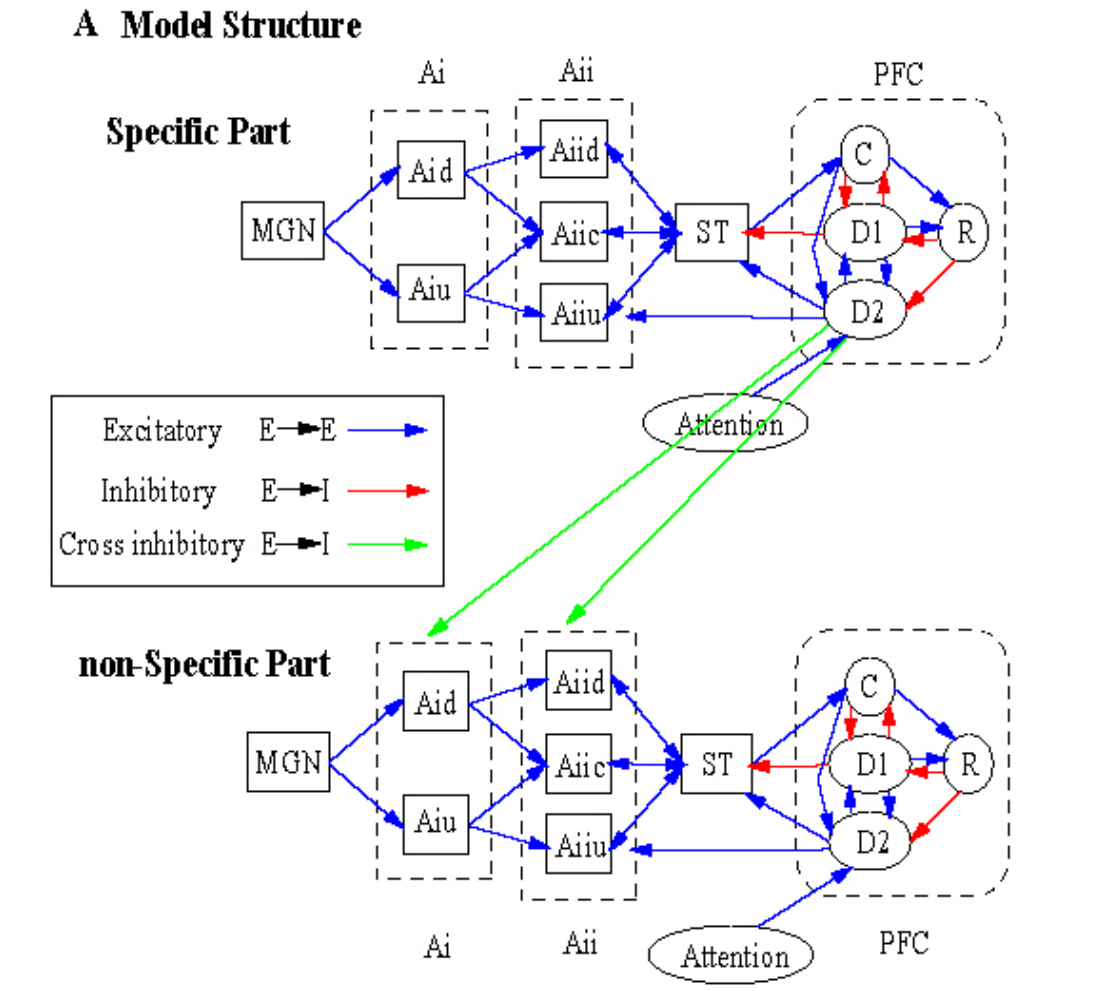
A Model Structure
Ai
Aii
PFC
Specific Part
MGN
Aid
Aiu
Aiid
Aiic
Aiiu
ST
C
D1
R
D2
Attention
Excitatory E→E
Inhibitory E→I
Cross inhibitory E→I
non-Specific Part
MGN
Aid
Aiu
Aiid
Aiic
Aiiu
ST
C
D1
R
D2
Ai
Aii
Attention
PFC

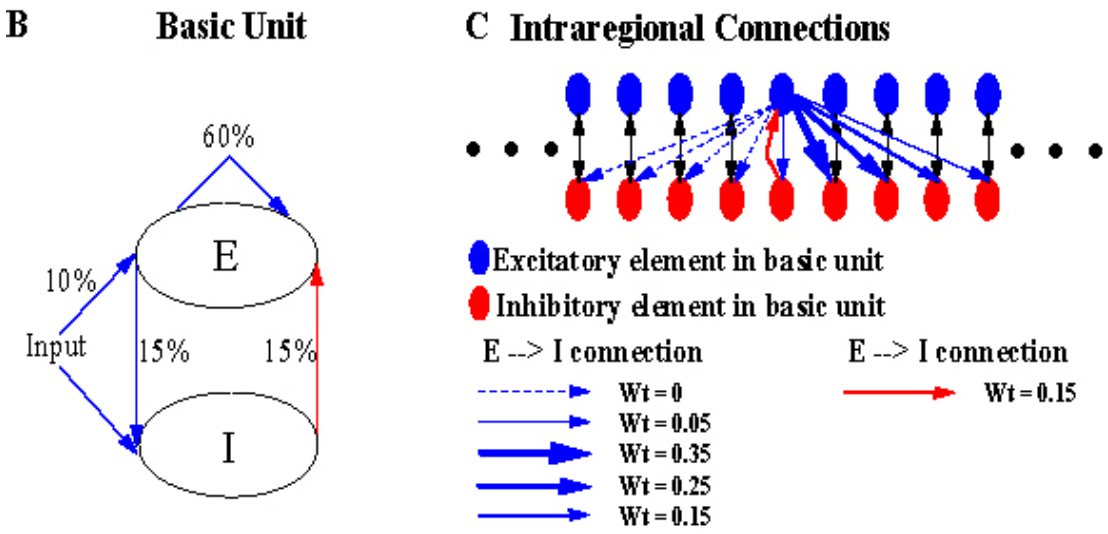
B Basic Unit
60%
E
10%
Input
15%
15%
I
C Intraregional Connections
Excitatory element in basic unit
Inhibitory element in basic unit
E --> I connection
Wt = 0
Wt = 0.05
Wt = 0.35
Wt = 0.25
Wt = 0.15
E --> I connection
Wt = 0.15

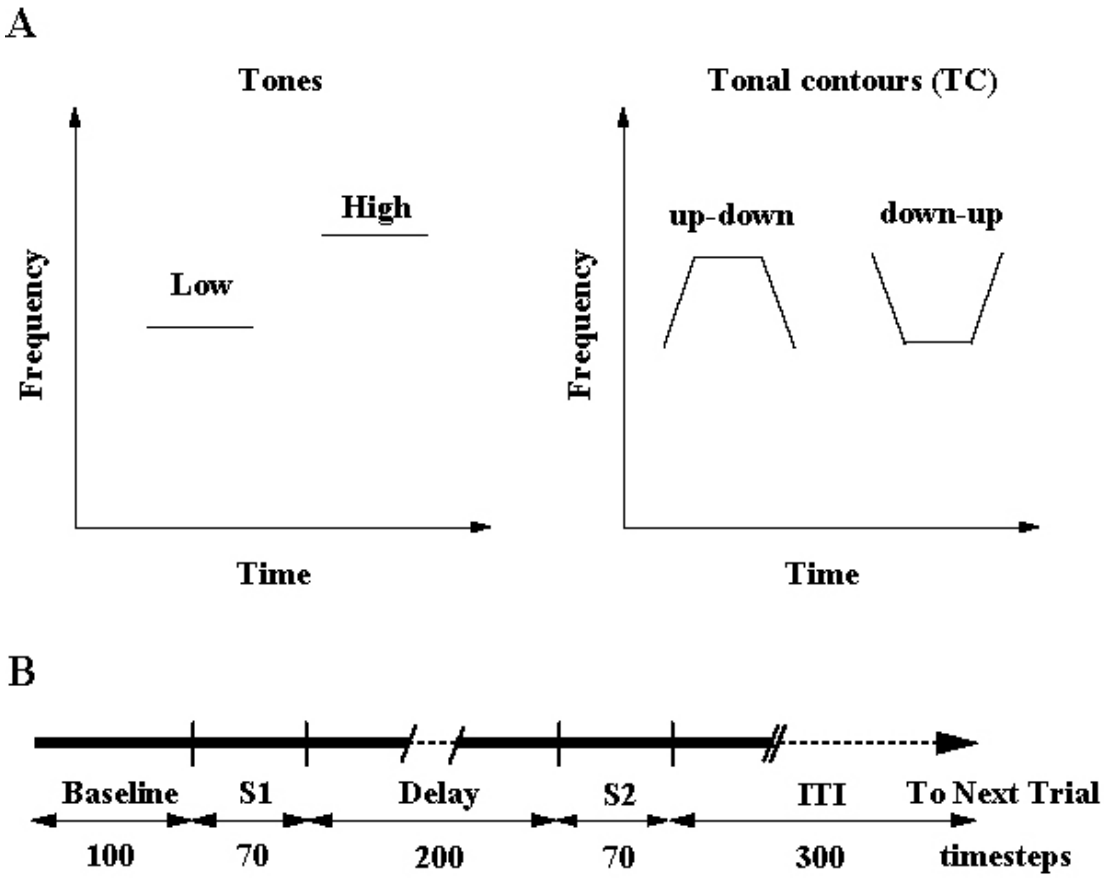

Fig 4-2. (A) Simulated sound stimuli. Each inset represents a spectrogram that depicts the simulated sound stimuli (tones and tonal contours). (B) Timeline of a single trial in the simulation. Each time step reflects 5 ms in the experimental condition.

4.3 Results

In this section, we illustrate the simulated integrated synaptic activity (ISA) and correlated DMS-specific cognitive modulation in auditory regions using a distributed network simulating the neuronal dynamics in both temporal auditory and frontal cognitive regions. We also used the regional ISA for further simultaneous simulation of the synthetic MEG and fMRI signals by forward models. For the simulated ISA and MEG signal, the modulation effect was measured by the modulation index (MI) values by comparing the magnitudes of the AERs/AEFs. For the simulated fMRI data, percentage signal change (PSC) values were compared between conditions to investigate the task-related changes of the BOLD signal. Furthermore, we compare the simulation results to the experimental results of the task-specific modulation of AER (Chapter 3) and BOLD signal change (Husain et al. 2004) to show that (1) this modeling approach can produce the task-related cognitive modulation of the auditory cortices observed in both MEG and fMRI studies; and (2) taking into account co-existence of the top-down enhancement and suppression of the auditory cortex being demonstrated by animal studies (Fritz et al. 2003, 2005, Bartlett et al. 2005) and involve them in the model simulation, we still can observe the DMS-specific suppression of AER, which is mainly caused by the broadly tuned top-down inhibition of the task-irrelevant auditory pathway from the memory processing units in frontal cortices of the specific part.

4.3.1 Simulation of the auditory evoked responses and the DMS-specific modulation

Fig. 4-3 illustrates the integrated auditory ISA (Fig 4-3 A) and auditory evoked responses (Fig 4-3 B) averaged across the matched trials with TC stimuli (TC_M) in both tasks and the simulated ISA (Ai + Aii across the subsystems) in each of the auditory regions (Ai, Aii, in specific and nonspecific subsystems, Fig 4-3 CDEF, respectively), where the integrated auditory ISA corresponds to the auditory source activity observed in the MEG experiment (Chapter 3, see analysis in source space). DMS-specific suppression of the AER to S2 is displayed (Fig. 4-3 A and B): AER magnitudes to S1 are similar between the PSL and DMS tasks, whereas the AER magnitude to S2 is smaller in DMS task than in PSL task. Furthermore, suppression of auditory ISA in DMS task comparing to the PSL condition can be seen as early as the late phase of S1 presentation and lasts through the delay period and early phase of S2 presentation (Fig 4-3 A). In depth examination of the ISA in each auditory region showed that AERs to S1 and S2 are similar in specific Ai (Fig 4-3 C), whereas in specific Aii region the ISA increases after presentation of S1 and the increase keeps through the delay period (Fig 4-3 D). Furthermore, slightly suppressed ISA in nonspecific Ai (Fig 4-3 E), and stronger suppression in nonspecific Aii (Fig 4-3 F) regions during the delay period and early phase of S2 presentation in DMS task was depicted. Therefore, the observed DMS-specific suppression of AER in auditory ISA was mainly contributed by the non-specific Ai and Aii regions, where the specific Aii region exerted an opposite influence. Besides the TC_M conditions, MI values also demonstrated similar DMS-specific suppression of AER and contributions

among the simulated auditory regions in TC_N conditions (Table 4-5, the values listed with bold font). Furthermore, comparing to the experimental results showed by the left representative ECD in the representative participant (participant #4), the MI values computed from the integrated auditory ISA in TC conditions (TC_M and TC_N) displayed consistent, yet weaker DMS-specific suppression to AER, whereas the simulated MI values with Tone stimuli were not different between the PSL and DMS tasks. This simulation result does not consist with the experimental findings in this participant, in which DMS-specific suppression of AER was also observed in Tone conditions (Table 4-3 and Fig 4-4).

4.3.2 Simulation of MEG signal and task-related modulation of the M100 response

Fig. 4-5 illustrates the RMS waveforms of the simulated auditory evoked field (AEF) averaged across the left representative sensors from experimental measurements of the representative participant. The data are from the matched trials of TC stimuli (TC_M) for PSL and DMS tasks. Subplots (A), (C) and (E) depict the simulated AEF aligned to the stimulus onset for PSL (upper inset) and DMS (lower inset) tasks, where the simulated MEG signal were obtained with auditory ECDs (ECDs in Ai and Aii regions), all ECDs (ECDs in Ai, Aii, ST, and PFC regions), and PFC ECD (only the ECD in PFC region), respectively. Simulation with auditory ECDs showed greater suppression of the AEF to S2 in the DMS task (MI=11.1%) than the PSL condition (MI=2.3%), which was comparable to the experimental results from this participant (DMS: MI=16.08%; PSL: MI=2.31%) computed from remapped MEG signal using the clustered M100 related ICs (Fig. 4.5 B, see chapter 2 for detail

description of the IC clustering and remapping of MEG signal), while the modulation effect computed using the noise-reduced and artifact-cleaned raw MEG signal showed similar pattern but greater suppression effect of AEF in both PSL and DMS tasks (Fig 4-5 D; DMS: MI=23.99%; PSL: MI=6.59%) In contrast, simulated AEF to S2 with all ECDs showed little difference between the task conditions (Fig. 4-5 C). This simulation result is consistent with the experimental results obtained across all subjects, where no task effect was observed, but not with the pattern showed by the representative participant, whose results showed stronger suppression of the AEF to S2 in DMS task than in PSL task (Fig 4-5 D). By listing out the contribution of each ECD to the simulated AEF, we showed that it is the contribution of the ECD in PFC region caused the lack of difference between tasks in the simulation results with all ECDs by generating stronger MEG signal during the delay period and presentation of S2 in DMS task than PSL task (Fig 4-5 F), which exerted an opposite influence to the AEF comparing to the contribution of auditory ECDs.

Similarly, in other conditions, simulation with auditory ECDs also showed greater suppression of the AEF to S2 (correspondently, greater MI values) in DMS tasks than PSL conditions (Table 4-6 A), which were comparable to the experimental results computed from the remapped MEG signal with the identified M100-related ICs (Table 4-6 B). On the other hand, the DMS-specific modulation of AEF was not observed in the simulated results with all ECDs, which was inconsistent to the experimental findings (Fig 4-6 B), and the PFC ECDs consistently generate enhanced MEG signals in DMS conditions (Table 4-6 A), which we believe is the cause for the lack of suppression of the AEF to S2 in the simulation results with all ECDs.

4.3.3 Simulation of BOLD signal

As mentioned in section 4.2, the regional ISA values used for BOLD simulation is computed differently from the simulation of MEG signal – the increase of excitatory and inhibitory synaptic activity both contribute to increase of the simulated ISA for fMRI simulation. As illustrated in Fig 4-7, the PSC from the simulated BOLD signal showed comparable values to the ones found experimentally (Husain et al. 2004) in both auditory and frontal regions except ST, in which the simulation result showed higher PSC (94.3%) value than the experimental results (Left: 28.8%; Right: 45.4%; also see table 4-7). Furthermore, the signal change in each region is also comparable to the experimental results (Table 4-7). In contrast to the MEG simulation results that being comparable to the experimental results in left auditory cortex, the simulated BOLD signal changes fit better to the experimental results in the right hemisphere than the left hemisphere (Fig. 4-7).

Table 4-5 Modulation index values [(1)] computed by the simulated auditory ISA.

		PSL				DMS			
		Tone_M (%)	Tone_N (%)	TC_M [(2)] (%)	TC_N (%)	Tone_M (%)	Tone_N (%)	TC_M (%)	TC_N (%)
Specific Part	Ai	-0.08	-9.58	-0.41	-8.20	0.35	-16.29	6.79	3.66
	Aii	-17.19	-13.25	-16.25	-18.68	-16.4	-16.02	-19.21	-14.94
	Ai + Aii	-35.24	-15.92	-31.93	-32.4	-32.03	-15.52	-50.90	-40.10
non-Specific Part	Ai	1.63	4.44	7.02	13.93	-1.91	-1.73	15.06	28.30
	Aii	-7.91	5.03	2.48	7.37	6.36	-3.52	8.39	9.71
	Ai + Aii	-5.52	3.79	3.80	8.81	-1.12	-4.05	9.57	14.10
Ai (Total)		0.65	8.09	21.1	5.49	10.46	-1.84	29.72	41.02
Aii (Total)		-6.39	3.03	0.16	1.98	-4.78	-4.76	3.96	5.91
Ai + Aii (Total)		-4.59	2.70	3.59	2.94	-2.73	-4.38	8.27	9.74
Left representative ECD [(3)]		-1.82	-4.51	0.0	-0.60	27.09	20.00	23.81	24.42

(1) The MI values were computed following the equation (3-1) in chapter 3. The AER and baseline values were replaced by the corresponding auditory ISA values in each simulated region.

(2) The abbreviations for simulated conditions are: Tone_M: Match trials with pure tone stimuli; Tone_N: non-match trials with tone stimuli; TC_M: match trials with TC stimuli; TC_N: non-match trials with TC stimuli.

(3) The experimental MI values were from participant #4 (Chapter 3), each was computed using the source activity of the left representative ECD in corresponding condition.

Table 4-6 A. Modulation index values (%) [1)] computed by the simulated MEG signals

Simulation [(2)]	Stimuli	PSL		DMS	
		Match	nonMatch	Match	nonMatch
With all ECD	Tone	-4.9	-1.5	-6.1	-6.8
	TC	-1.3	-2.7	-6.1	-6.1
With AUD ECDs	Tone	-4.0	0.2	1.0	8.6
	TC	**2.3**	-1.3	**11.1**	6.9
With PFC ECD	Tone	-43.0	-35.7	-9.0	-13.5
	TC	-42.0	-37.4	-17.3	-14.4

(1) The MI values were computed following the equation (3-1) in chapter 3. The auditory evoked field (AEF) and baseline values were replaced by the corresponding RMS values of the simulated magnetic field averaged across the left representative sensors.

(2) The MEG signals in sensor space were obtained with three different simulations: (i) All 4 ECDs were used to simulate the magnetic field to model the influence of multiple sources to the MEG signal and the AEF; (ii) Only the ECDs in simulated regions Ai and Aii were used to simulate the magnetic field to model the influence of the auditory activity to the MEG signal and the AEF; and (iii) Only the PFC ECD was used in simulation to investigate the influence of the frontal sources to the MEG signal and the AEF.

Table 4-6 B. Experimental modulation index (MI) values (%) * in sensor space.

Datasets	Stimuli	PSL		DMS	
		Match	nonMatch	Match	nonMatch
Raw MEG	Tone	6.95	-3.22	22.88	3.79
	TC	**6.59**	**6.03**	**23.99**	**18.94**
Remapped MEG with AEF ICs	Tone	9.72	-6.04	21.10	-1.96
	TC	**2.31**	**4.54**	**16.08**	**12.80**

* The MI values were computed using the sensor space MEG data from participant #4 in the MEG experiment (see detail in chapter 3). Two dataset were used to compute the MI values: (i) The noised-reduced and artifact-cleaned raw MEG signal; and (ii) The remapped MEG signal by the M100 related ICs (for detail description of the method, see Chapter 2). The auditory evoked field (AEF) and baseline values were replaced by the corresponding RMS values of the magnetic field averaged across the left representative sensors.

Table 4-7 Percentage signal change (PSC) of the simulated (1) and experimental (2) BOLD values for DMS task with two types of sound stimuli (Tones and TC), relative to Rest condition.

Region	Experimental BOLD (Left Hemisphere)			Experimental BOLD (Right Hemisphere)			Simulated BOLD		
	TC-Rest (%)	Tone-Rest (%)	nTC-nTone (%)	TC-Rest (%)	Tone-Rest (%)	nTC-nTone (%)	TC-Rest (%)	Tone-Rest (%)	nTC-nTone (%)
Ai	0.32	0.27	18.5	0.26	0.20	30.0	0.36	0.27	33.3
Aii	0.52	0.37	40.5	0.48	0.34	41.2	0.41	0.27	51.9
ST	0.67	0.52	28.8	0.61	0.42	45.2	2.37	1.22	94.3
PFC	0.28	0.24	16.7	0.24	0.13	84.6	12.0	6.11	96.4

(1) See the method part of this chapter for detail description of the simulation setup and the definition of PSC.

(2) The experimental results were from Husian et al. (2004) table 4a.

Fig. 4-3 Simulated auditory ISA and modulation of AER. Data are from the matched trials with TC stimuli (TC_M). In (A), (C), (D), (E) and (F), each waveform represents a 3.7 sec averaged epoch with time zero at the onset of S1. The blue waveforms represent the averaged epoch obtained from the simulated PSL task, and the red waveforms represent the averaged epoch obtained from the simulated DMS task. (A) Averaged epochs of the auditory ISA, which is computed by integrating the ISA across the Ai and Aii regions in both subsystems. The time windows of stimuli presentation (S1 and S2) are illustrated by the black bars. (B) Auditory evoked responses (AERs) to S1 and S2. The upper inset illustrates the AERs to S1 and S2 in simulated PSL task, and the lower inset illustrates the AERs in DMS task. Each waveform represents a 300 ms epoch (-50 ms ~ 250 ms) timelocked to the stimulus onsets, where the blue traces depict the AERs to S1 and the red traces depict the AERs to S2. The epochs were extracted from the dataset depicts in (A). (C) The ISA of specific Ai region. (D) The ISA of specific Aii region. (E) The ISA of non-specific Ai region. (F) The ISA of non-specific Aii region. Integration of the ISA depicted in (C), (D), (E) and (F) produces the dataset depicted in (A).

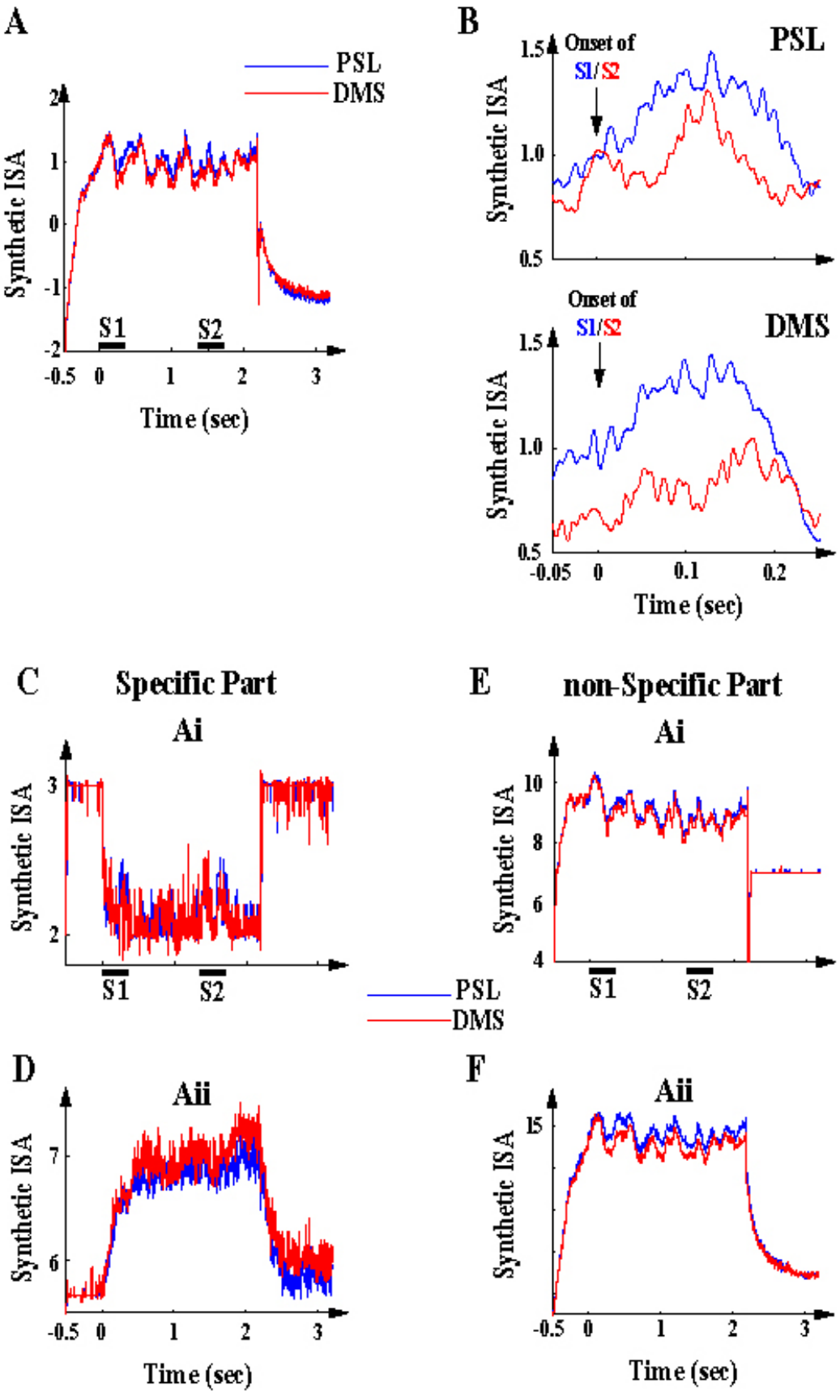
A
PSL
DMS
Synthetic ISA
S1
S2
Time (sec)
B
Onset of
S1/S2
PSL
DMS
Synthetic ISA
Time (sec)
C
Specific Part
Ai
Aii
E
non-Specific Part
Ai
Aii
D
F
Synthetic ISA
Time (sec)

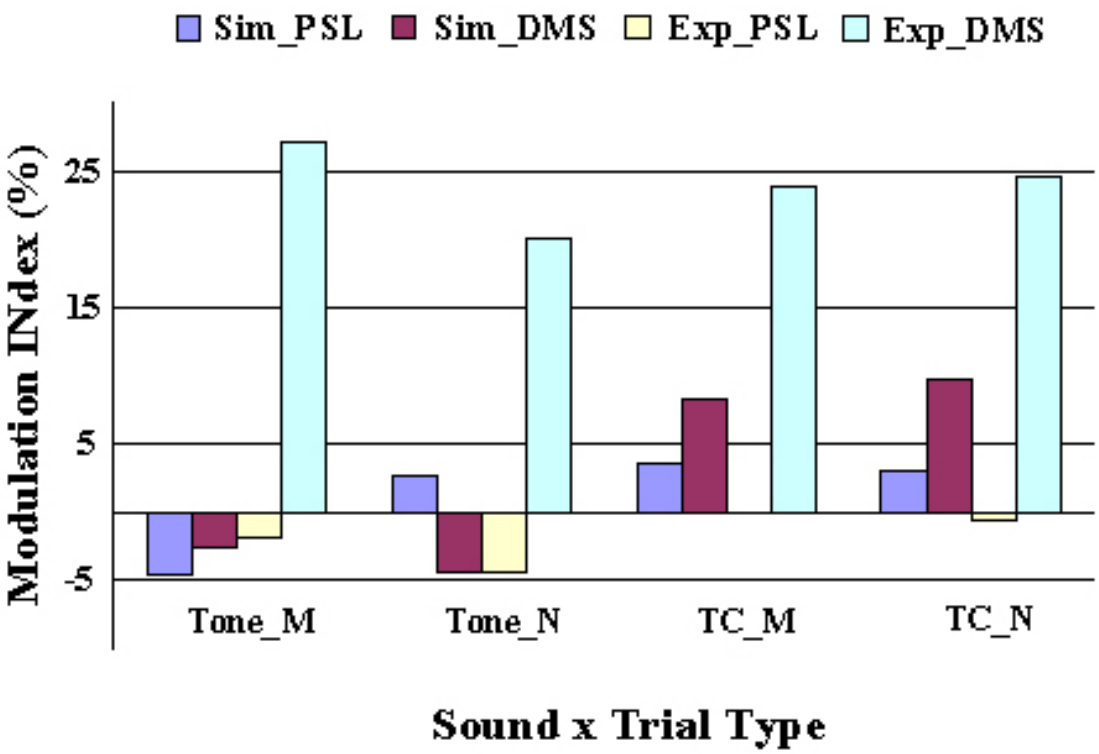

Fig. 4-4 Simulated and experimental modulation index (MI) values in source space. The simulated MI values were computed with the integrated auditory ISA (Ai+Aii). The experimental values were from the source activity of the left representative ECD of participant #4 in the MEG experiment (see Chapter 3 for detail of the experimental analysis).

Fig. 4-5 Root mean square (RMS) values of the simulated auditory evoked field (AEF) and corresponding experimental AEF averaged across the left representative sensors. All data came from the matched trials with TC stimuli (TC_M). For each plot, the upper inset(s) depict the PSL task, and the lower inset(s) depict the DMS task. The experimental data were obtained from participant #4 (see chapter 3 for detail). For all plots, each waveform represents a 300 ms epoch with time zero at the stimuli onset. The red waveforms represent the AEF to S1 and the blue waveforms represent the AEF to S2. (A) Insets in left column depict the simulated AEF waveforms obtained from forward simulation based upon the ECDs in Ai and Aii. Insets in the right column are the corresponding field contour maps at the peak latency of the AEFs (~100 ms). (B) The experimental results corresponding to the conditions showed in (A). The data were from the remapped MEG signals using the M100-related independent components (AEF ICs; see text in chapter 2 and this chapter for detail description). (C) The RMS waveforms of the simulated AEFs obtained from forward simulation using all ECDs. (D) The RMS waveforms of the experimental AEFs obtained from the noise-reduced and artifacts-removed raw MEG signal. (F) The RMS waveforms of the simulated AEFs obtained from forward simulation using PFC ECDs.

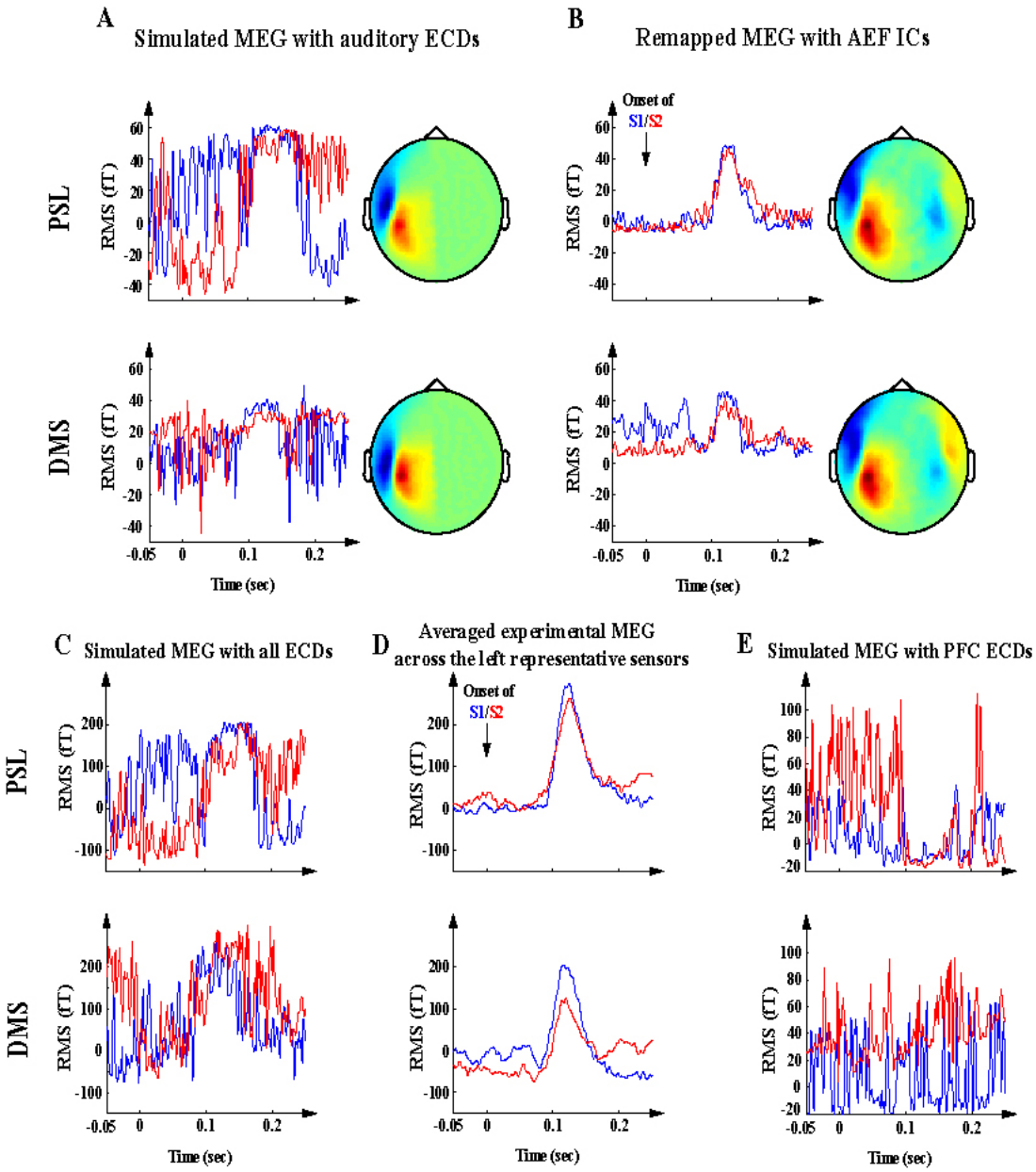
A
Simulated MEG with auditory ECDs
B
Remapped MEG with AEF ICs
PSL
DMS
RMS (fT)
Onset of
S1/S2
Time (sec)
C
Simulated MEG with all ECDs
D
Averaged experimental MEG
across the left representative sensors
E
Simulated MEG with PFC ECDs

Fig 4-6 Simulated and experimental modulation index (MI) values in sensor space. All MI values were computed using the RMS values of the magnetic fields averaged across the left representative sensors. The experimental data were from the participant #4 in MEG experiment (Chapter 3). (A) The simulated MEG signals were computed by using the auditory sources (ECDs in Ai and Aii regions) in the forward model. The experimental values were from the RMS of the remapped magnetic field averaged across the left representative sensors, where the remapping was taken with clustered AEF-related ICs (Chapter 2). (B) The MEG signals simulated with all source ECDs (Ai, Aii, ST and PFC), where the experimental values were computed from the noise-reduced and artifact-cleaned raw MEG signal.

A

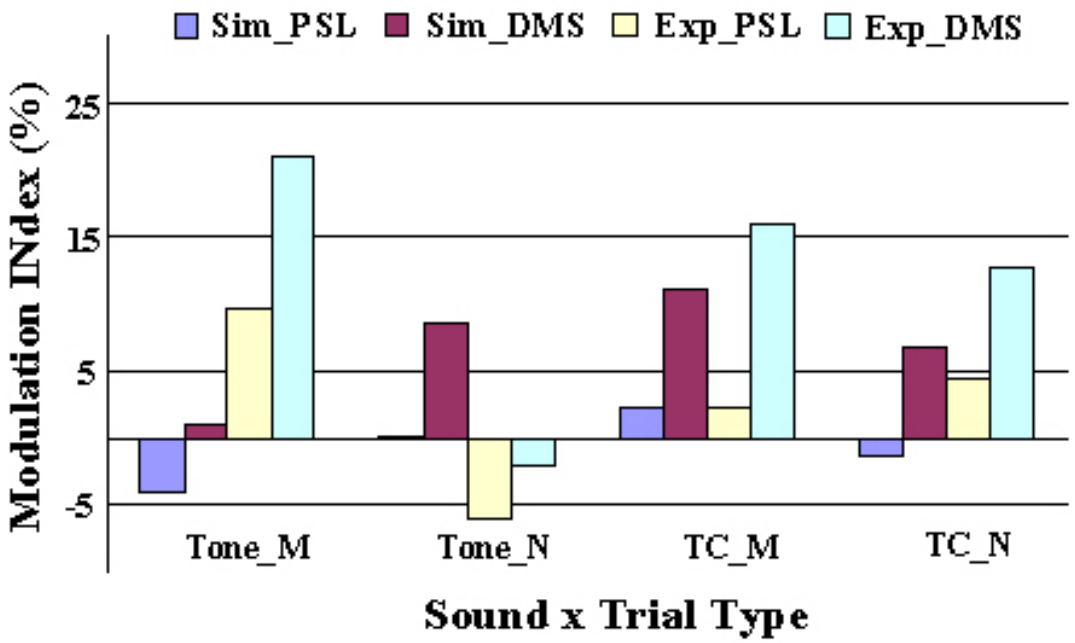
Sim_PSL
Sim_DMS
Exp_PSL
Exp_DMS
Modulation INdex (%)
25
15
5
-5
Tone_M
Tone_N
TC_M
TC_N
Sound x Trial Type

B

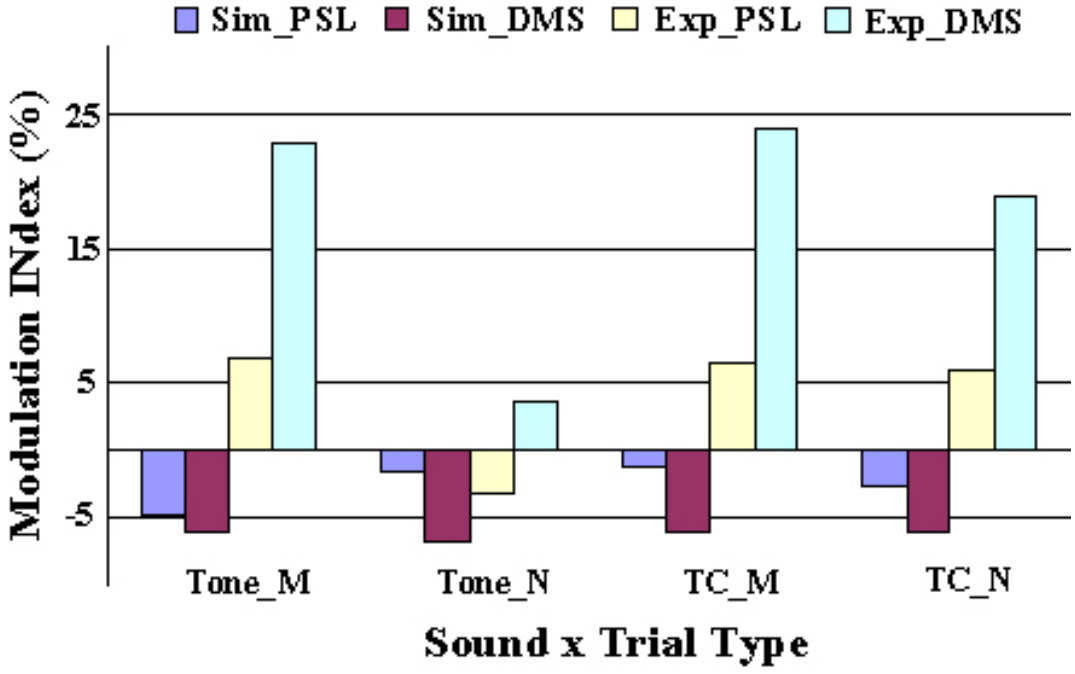
Sim_PSL
Sim_DMS
Exp_PSL
Exp_DMS
Modulation INdex (%)
25
15
5
-5
Tone_M
Tone_N
TC_M
TC_N
Sound x Trial Type

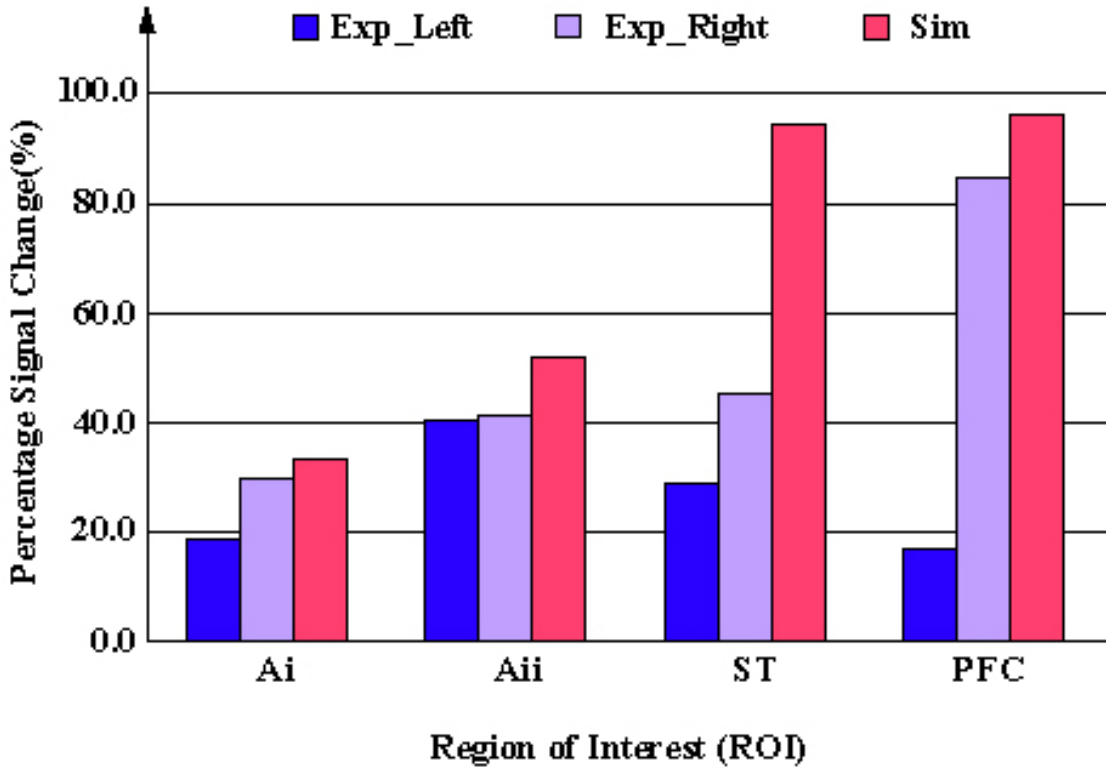

Fig. 4-7 Percentage signal change (PSC) of the simulated and experimental BOLD signals in the regions of interest (ROIs). The experimental PSC values of the ROIs in left (blue) and right (purple) hemispheres and the simulated PSC values in corresponding regions (red) were plotted. The values are listed in table 4.7

4.4 Discussion

This chapter presents a methodological approach to simultaneously simulate the system-level neuronal activity, MEG and fMRI signals correlated to performing the DMS task. The simulation results are integrated with the experimental findings to investigate the DMS-specific modulation of human auditory cortex and underlying neural dynamics. Incorporating the knowledge of the electrophysiological and the hemodynamic activities in auditory cortex from studies employing the delayed response paradigms, a large-scale network model including temporal auditory and frontal cognitive regions is used to simulate the neuronal activity and integrated synaptic activity (ISA) in each region during task performance, where the further simulation of MEG and fMRI signals were taken by using the regional ISA as inputs to the corresponding forward models. Both simulated MEG and fMRI signals demonstrated DMS-specific dynamics comparable to the experimental observations, where the increased inhibitory influence by the specific frontal memory processing unit to the non-specific auditory regions could account for the demonstrated DMS-specific suppression of AER. These findings support our hypothesis that the task-specific dynamics observed in MEG and fMRI experiments during performance of the DMS task can be interpreted by a united underlying network and corresponding physiological processes.

4.4.1 Task-specific top-down modulation of the auditory cortex

Task-specific feedback modulation to the sensory cortices has been found play multiple roles in human cognitive function, such as executive control (Miller &

Cohen 2001), memory maintenance and manipulation (Pasternak & Greenlee 2005), and inhibitory filter of the task-irrelevant information (Fritz et al. 2007). One well accepted hypothesis about the top-down control is facilitating the sensitivity of the goal-relevant stimuli by enhancing the processes of relevant information and at the same time suppress the irrelevant circuits (Fritz et al. 2007). Supportive evidences about the suppression part have been observed in gaze-control network in barn owls (Winkowski & Knudsen, 2007) and the tactile discrimination network in human being (Machens et al. 2005). Furthermore, a recent computational model successfully simulated the inhibitory top-down modulation from the frontal regions to the somatosensory cortex instantiated by the memorized component during performance of a tactile DMS task (Miller & Wang, 2006). In this model, two parallel subsystems were included to simulate the neuronal groups that involves in performance of the auditory DMS task: the subsystem correlated to perception of tested pattern stimuli (specific part) and the groups that correlate to task-irrelevant processing (non-specific part), respectively. For each part, both temporal auditory and frontal cognitive regions were simulated, where the fronto-temporal connections modeled the top-down cognitive control: The connections between the frontal memory processing units to the superior temporal region and secondary auditory cortices in the specific part simulated the distributed network of the STM maintenance and top-down enhancement of the processing correlated to task-performance; whereas the top-down suppression of the task-irrelevant processing was simulated by the cross-subsystem fronto-auditory inhibitory projections. Furthermore, we simulated the enhanced top-down modulation in a narrowly-tuned manner (1:5 fan out) and the inhibitory top-

down modulation in a broadly-tuned manner (1:81 fan out) to accommodate the experimental findings that 2/3 of the primary auditory neurons showed decreased response when there was a similar sound stimuli presented at one second before (Bartlett et al. 2005). Therefore, increased memory unit activity during DMS task should correlate to both enhancement of the Aii region activity in the specific subsystem and suppression of the non-specific Ai and Aii regions, and the net DMS-related effect could be simulated as suppression of AER to S2 with appropriate parameter set. As predicted, the simulation results demonstrated stronger suppression of the auditory evoked responses (AER) in the DMS tasks than PSL tasks with TC stimuli, which is consistent with the findings in MEG experiment (Lu et al. 1992, Luo et al. 2005; also see chapter 3 of this dissertation). Examination of ISA in each region do showed increased activity to the specific Aii region and decreased ISA in the non-specific Ai and Aii regions.

Furthermore, the forward MEG simulation with the source equivalent current dipoles (ECD) in auditory regions also showed stronger suppression of the M100 response in DMS task than PSL conditions, which agrees with the analysis of the remapped MEG measurements using the clustered M100 related independent components (Table 4-6 A B; Fig 4-6 A). In contrast, forward MEG simulation using all ECDs didn't show different modulation of the AEF between the tasks, which was consistent with the experimental results averaged across all participants but not with the data from the representative one, from whom the spatial information of the source ECDs and source-sensor relationship for forward MEG modeling were obtained. In depth examination showed that this discrepancy between the experimental

observations and the simulation results with all ECDs might come from the contribution of the frontal source ECD in the simulation, which causes increase of the magnitude of the M100 response to S2 during the DMS task, and this effect canceled the suppression by the auditory ECDs. Further simulation to address this problem can include the mutual inhibition between the memory processing units of the two subsystems, as being modeled in simulating the neuronal dynamics during performance of the tactile discrimination task (Machens et al. 2003; Miller & Wang, 2006).

4.4.2 DMS-related increase of BOLD signal in auditory cortices originates from the enhanced top-down inhibitory modulation

In addition, forward simulation of the BOLD signal demonstrated close to experimental signal change (Husain et al. 2004) in the simulated regions, where TC conditions showed increased BOLD signal than Tones during performance of the DMS task. An improvement compared to the original model is that the Ai region also showed increased BOLD signal for TC stimuli than Tones during performance of the DMS task (PSC = 33.3%), which agreed with the experimental findings (Left PSC = 18.5%; Right PSC = 30.0%) but hasn't been shown by the simulation with original model. Furthermore, the signal changes for DMS task compared to the rest condition showed values close to the experimental findings (table 4-7).

4.4.3 Conclusion

In summary, we used an integrated modeling approach to address the problem of finding a common underlying physiological mechanism for the DMS-specific

auditory dynamics observed in DMS and fMRI experiments, which was validated by comparing the simulation results to the experimental findings. Moreover, this approach provides a framework for linking the physiological, the hemodynamic and the EEG/MEG studies of the auditory regions and allows further simulation of the neuronal dynamics correlated to the auditory object processing and corresponding cognitive functions.

CHAPTER 5: GENERAL DISCUSSION AND CONCLUSION

In this dissertation I propose an integrated approach for combining neural modeling and MEG methods, in order to investigate the task-specific cognitive modulation of human auditory cortex during the performance of an auditory delayed-match-to-sample (DMS) task. The results demonstrated that: (1) the suppressive modulation of the evoked responses in auditory cortex observed in DMS task is task-specific, and is due to increased top-down fronto-temporal inhibitory functional connectivity during task performance; (2) the phenomenon can be replicated by a biophysically realistic, large-scale neural network model for auditory object perception, which specifies inhibitory connections between the frontal memory processing units and the auditory regions; and (3) In addition to the suppressive effect in modulation of auditory evoked responses (AERs), simulated task-related inhibition from frontal memory processing units to the auditory regions can also account for the increased BOLD signal in auditory cortex and the selectivity for tonal contour stimuli that were reported in a previous fMRI study (Husain et al. 2004).

Furthermore, in this dissertation I present a novel signal processing method using independent component analysis (ICA) to process and analyze MEG signals. This method is proven to be very effective for both artifact removal and the analysis of functional neural circuits.

5.1 Integrated approach for investigation of human cognitive function

The integrated approach taken in this dissertation was multidisciplinary, and multilevel: First, system-level neural dynamics, including regional neuronal activity and integrated synaptic activity (ISA) related to the processing of auditory objects, were simulated by a large-scale neural network model based on the known electrophysiological properties of the brain regions involved. The model included both a 'specific' subsystem correlated to task-relative processing and a 'non-specific' subsystem that represented computations in (common) task-irrelevant pathways. Second, the synthetic ISA was used as input to forward models to simulate both magnetoencephalography (MEG) and functional magnetic resonance imaging (fMRI) signals. Third, MEG signals were measured from human participants to investigate the modulation of human auditory evoked responses (AER) induced by the overt processing of auditory short-term memory (STM) using a delayed-match-to-sample (DMS) task. The DMS task was compared to two control tasks - passive listening (PSL) and counting (CNT). Finally, the experimental and simulation results were integrated at both 'mesoscopic' (synaptic activity integrated over networks of neurons) and 'macroscopic' (MEG and fMRI measurements) levels (Riera et al. 2005). This integration increased our understanding of the underlying neural mechanism of the observed task-specific modulation effect: at the mesoscopic level, the simulated auditory ISA was compared with the dynamics of neuronal populations inferred by measurement of MEG. Simultaneously, at the macroscopic level, the synthetic MEG signals produced by the forward models were compared with the

measured MEG signals recorded in the experiments. The synthetic fMRI signals were also compared with the experimental results from a previous study involving the DMS task (Husain et al. 2004). With these independent approaches and the integration of their results, I was able to infer a biologically-plausible yet hypothesis-driven interpretation of the experimental findings on cognitive modulation of auditory evoked responses in humans.

Comparison between simulated and experimental results showed that this approach can bridge the gaps between the knowledge of the task-related neural circuits obtained from brain imaging techniques and the knowledge from microscopic electrophysiological recordings in either non human animals or neurosurgical patients. In addition this approach can also address the poorly understood relationships between different brain imaging methods.

The first major finding supporting this approach is that simulated memory-related frontal modulation of auditory units (including both excitatory feedback to the specific regions and inhibitory modulation to the non-specific regions), can reproduce the DMS-specific suppression of the AER observed in experimental results. The MEG experimental results in Chapter 3 showed suppressive modulation to the AER confined to the performance of the DMS. However, previous electrophysiological recordings in ferret and marmoset monkey auditory cortex have reported both enhancement and suppression modulation effects on auditory neuronal activity (Fritz et al. 2003, Bartlett et al. 2005). Furthermore, in human studies manipulating attention, enhanced evoked responses were also demonstrated (Hillyard et al. 1973; Woldorff et al. 1993). This suggests that both excitatory and inhibitory modulation

pathways should exist between the frontal cognitive and temporal auditory regions. In an effort to account for these pathways, we applied both narrowly-tuned excitatory feedback to the auditory regions in the specific subsystem and broadly-tuned inhibitory modulation to the non-specific auditory regions. This method is consistent with the experimental evidence indicating that the majority of auditory neurons (~60%) showed reduction of activity in a similar behavior paradigm (Bartlett et al. 2005). With this methodology, the current study successfully simulated the suppression of AER in the DMS task and the absence of this effect in the passive listening condition, which is consistent with the experimental findings. Furthermore, examination of the simulated ISA in each region of interest demonstrated increased evoked response in specific Aii units and decreased ISA in non-specific auditory regions. This finding is consistent with the broadly accepted view of top-down cognitive control that posits that enhancement of the task-relevant pathway and the suppression of the task-irrelevant pathway should be co-existing to increase the sensitivity to task-relevant stimuli (Miller & Cohen 2001). This hypothesized structure of task-related feedback modulation merits additional experimental investigation.

Further evidence in support of this integrated approach can be found in the simulated tonal contour specificity of the BOLD signal changes in the DMS task. This tonal contour specificity is comparable to fMRI experimental findings (Husain et al. 2004) but had not been successfully simulated to date. This modeling approach can relate experimental findings from different types of brain imaging methods (MEG and fMRI) on the task-related modulation of the human auditory cortex. This was

achieved mainly through the top-down inhibition to the non-specific auditory regions from the specific frontal memory processing units, which is consistent with the theory of top-down control and empirical evidences.

While the feasibility of this approach has been successfully demonstrated, discrepancies exist between the experimental and simulation results. First, in the simulation, the top-down modulation was executed through the pre-frontal memory units to the auditory cortices, while in the experimental results, more frontal regions were found to have task-related increase of the functional connectivity with the auditory region. In addition to the memory-related regions, regions related to other cognitive functions --such as executive control (e.g., right inferior frontal gyrus and anterior cingulated cortex) and motor response preparation (e.g. bilateral pre-motor areas) were involved. These findings suggested the participation of multiple cognitive functions in the observed modulation effect, rather than the memory processing units alone. According to the 'network memory' theory (Fuster 1997), memory is stored in a distributed network and the control is through the memorized representation of the stimuli and 'executive rules', whereas the simplified top-down connections between the frontal memory units and the auditory regions in this study were not complicated enough to capture the multiple cognitive modulation observed in the experimental results. More experimental studies with parametric manipulation of the involved cognitive functions are required to determine the functional role of each neural region in the observed modulation effect. Second, though the simulated DMS-specific modulation of AER and tonal contour specificity is consistent with the experimental findings in source space, only the simulated auditory ECDs of MEG signals showed

similar task-specific dynamics comparable with the experimental MEG results (MEG remapped with M100-related independent components –ICs). The simulated sensor space MEG signals with all ECDs showed enhancement of AER to S2 rather than the suppression observed in experiment. Examination of the contribution of each ECD to the synthetic MEG data showed that the PFC ECD contributed to the increase. Thus, further simulations which include gain control of the PFC influence over the MEG signal on temporal sensors (or a constraint in the increase of PFC activity during the delay period) might be helpful in solving this discrepancy. For the latter approach, a potential solution would be to include mutual inhibition between the memorized components (Machens et al. 2003). This approach would result in a more focal, decreasing influence of PFC activity, as has been demonstrated in the modeling of a somatosensory DMS task.

5.2 Task-specificity of the cognitive modulation of auditory evoked responses

The suppressive modulation of the auditory evoked response (AER) during performance of the auditory DMS task has also been observed in previous studies (Luo et al. 2005, Lu et al. 1992). However, it has not been determined whether this effect is specifically correlated to performance of DMS task, or it is due to the pre-attentive adaptation to stimulus presentation (Näätänen et al. 2001). By comparing the DMS task to two control tasks (passive listening and counting), the current study demonstrated not only the DMS-specificity of the observed suppressive modulation effect, but also the involvement of multiple cognitive functions (including memory, executive control and motor response preparation). The increased memory storage

during DMS task performance corresponded with an increase of the modulatory influences to the task-irrelevant pathways exerted by correlated frontal regions to the auditory cortex. This correspondence can account for the observed task-specificity. This interpretation partially supports the 'predictive coding' theory (Friston et al. 2005) regarding the involvement of memory storage, but diverges from it in regards to the mechanisms for memory formation and the targets of inhibitory modulation. In the modeling the evoked responses of EEG/MEG in the oddball paradigm using dynamic causal modeling (DCM), the 'predictive coding' theory suggests that the memory trace is formed gradually, based on the statistical inference of the sensory experience (Kiebel et al. 2006). Because of this, an intrinsic rather than extrinsic mechanism should underlie the observed adaptation effect in the oddball paradigm (David et al. 2003, 2006). According to this theory, the DMS and PSL tasks should have shown similar modulation effect to AER, since both tasks employed sensory experience of the same stimuli. In contrast, the experimental results in this dissertation show that performing the DMS task induced significantly stronger suppression to the AER than PSL condition. This indicates that the explicitly-formed memory storage initiated during the delay period when performing DMS task has a stronger influence than the implicitly-formed memory storage that occurs during passive conditions (such as PSL). Furthermore, performing the DMS task requires online refreshment of the short-term memory of the stimuli to avoid the interference from other sensory events (Postle 1999). In the model, this online refreshment procedure was incorporated by the manipulation of the attention gain to the memory

processing unit, based on striatal and midbrain dopamine modulation (Chadderdon & Sporns 2006).

In addition to task-specificity, the experimental results also demonstrated lateralization to left hemisphere and tonal contour stimulus specificity of the modulation effect. Similar task-specific hemispheric asymmetry and stimuli selectivity have been shown in both MEG (Poeppel et al. 1996, Chait et al. 2004) and fMRI (Brechmann et al. 2007) studies. Both hemispheric functional specificity (Grimm et al. 2006, Brechmann et al. 2005, Zatorre, et al. 2002) and temporal scale sensitivity (Poeppel 2003, Boemio et al. 2005) can be used to interpret these findings. Whether the right auditory cortex's selectivity for the direction of frequency modulation (Brechmann et al. 2005), or its temporal sensitivity of the acoustic changes drives the effect, our finding of the asymmetric modulation to the auditory cortex is compatible with the hypothesis that the short-term memory (STM) processing of the task-related stimuli suppressed the irrelevant processing in the left auditory cortex.

5.3 Enhancing the ability to detect biological events in MEG signals using a clustering method and independent component analysis (ICA)

The current study also presents an automatic clustering method to categorize the independent components (IC) derived from MEG measurements using ICA decomposition. This method also correlates the ICs to certain biological events, including artifacts and auditory evoked field (AEF). Validation of this method for

artifact removal has been successfully undertaken with two MEG datasets, which suggested the feasibility of using this method in analyzing MEG data. Furthermore, with categorized AEF related ICs, M100 response in the remapped MEG signal showed clear DMS-specific modulation effect in a single participant. This indicates that this method is useful in analyzing cognitive function not only among multiple subjects, but also in individuals.

ICA decomposition has been proved to be a powerful method for isolating both artifacts (Makeig et al. 1996, Vagario et al. 2000) and function-related signals from the EEG/MEG measurements (Makeig et al. 1997, 2004). However, for multi-channel systems (such as a MEG scanner), to analyze the hundreds or thousands of ICs obtain by ICA decomposition poses a significant problem. Therefore, an automatic IC categorization method can greatly simplify the subsequent analyses. The categorization method presented here takes into account not only the IC's statistical aspects (such as kurtosis and entropy used during the algorithm estimation), but also the spatial and spectral characteristics of the ICs. This increases the method's ability to detect ICs that can not be identified using the statistical criteria alone. In this method, two steps require user input: the selection of template and the selection of criteria for each feature. During the analysis of AEF ICs, the template selection was automated by taking the contour map at the peak latency of the M100 response, which further improved the applicability of this method.

5.4 General Conclusion

This dissertation presents an integrated approach to investigating the task-specificity of cognitive modulation to human auditory cortex. For this purpose, task-

related brain activity was measured with whole-head MEG, and the task-specific modulation effect to auditory evoked responses was investigated. This effect was also simulated with a distributed neural network model that reproduced the neuronal dynamics in the temporal, auditory and frontal regions. By integrating the experimental and simulation results, this study demonstrated that this approach can not only connect brain imaging measurements with underlying neuronal activities and interregional connectivity patterns, but can also relate data from different types of brain imaging techniques, in order to infer the neuronal dynamics correlated to human cognitive functions. The results of this dissertation have demonstrated that this approach is both feasible and applicable to the study of human cognitive neuroscience. Because of the novelty of the current study's methodology, additional research will be needed to improve our understanding of the cognitive modulation of human auditory cortex by performance of specific cognitive tasks, and its mechanisms and computations.

Appendices

Appendix A. The MEG forward solution

The forward solution of neuromagnetism follows the Maxwell equations:

$$\nabla \cdot \mathbf{E} = \frac{\rho}{\varepsilon_0} \tag{A-1}$$

$$\nabla \times \mathbf{E} = -\frac{\partial \mathbf{B}}{\partial t} \tag{A-2}$$

$$\nabla \cdot \mathbf{B} = 0 \tag{A-3}$$

$$\nabla \times \mathbf{B} = \mu_0 (\mathbf{J} + \varepsilon_0 \frac{\partial \mathbf{E}}{\partial t}) \tag{A-4}$$

where the equations (1), (2) and (3), (4) denote the divergence and curl of the electric field $\mathbf{E}$ and the magnetic field $\mathbf{B}$, respectively. $\mathbf{J}$ and ρ are the total current density and charge density, and ε_0 and μ_0 are the electric permittivity and magnetic permeability of free space, respectively (Jackson 1999). With the quasi-static assumption in neuro-electromagnetism (Hämäläinen et al. 1993), the derivatives of the electric and magnetic fields are close to zero, thus the equations (1) ~ (4) are transformed to

$$\nabla \cdot \mathbf{E} = \frac{\rho}{\varepsilon_0} \tag{A-5}$$

$$\nabla \times \mathbf{E} = 0 \tag{A-6}$$

$$\nabla \cdot \mathbf{B} = 0 \tag{A-7}$$

$$\nabla \times \mathbf{B} = \mu_0 \mathbf{J} \tag{A-8}$$

in which the total current density $\mathbf{J}(\mathbf{r})$ at location $\mathbf{r}$ can be separated linearly into primary current $\mathbf{J}^{\mathbf{P}}(\mathbf{r}')$ and volume current $\mathbf{J}^{\mathbf{V}}(\mathbf{r})$. $\mathbf{J}^{\mathbf{P}}(\mathbf{r}')$ represents the intracellular source current at the location $\mathbf{r}'$, and the volume current $\mathbf{J}^{\mathbf{V}}(\mathbf{r}) = \sigma(\mathbf{r})\mathbf{E}(\mathbf{r})$ is determined by the electric field and the electric conductivity σ. With the quasi-static assumption, the electric field can be expressed with scalar potential Φ as

$$\mathbf{E} = -\nabla\Phi \tag{A-9}$$

where ∇ is the operator of spatial gradient, thereby the volume current turns into

$$\mathbf{J}^{\mathbf{V}}(\mathbf{r}) = \sigma(\mathbf{r})\mathbf{E}(\mathbf{r}) = -\sigma(\mathbf{r})\nabla\Phi(\mathbf{r}) \tag{A-10}$$

Thus, the current density at position $\mathbf{r}$ is

$$\mathbf{J}(\mathbf{r}) = \mathbf{J}^{\mathbf{P}}(\mathbf{r})\delta(\mathbf{r}-\mathbf{r}') + \mathbf{J}^{\mathbf{V}}(\mathbf{r}) = \mathbf{J}^{\mathbf{P}}(\mathbf{r}') - \sigma(\mathbf{r})\nabla\Phi(\mathbf{r}) \tag{A-11}$$

where $\delta(\mathbf{r}-\mathbf{r}')$ is the Dirac delta function.

According to the Biot-Savart law, $\mathbf{B}(\mathbf{r})$ is determined by

$$\mathbf{B}(\mathbf{r}) = \frac{\mu_0}{4\pi}\int \frac{\mathbf{J}(\mathbf{r})\times(\mathbf{r}-\mathbf{r}')}{\left|\mathbf{r}-\mathbf{r}'\right|^3} dv' \tag{A-12}$$

where $\left|\mathbf{r}-\mathbf{r}'\right|$ is the norm of the spatial vector pointed from the source location $\mathbf{r}'$ to the observation point $\mathbf{r}$. Substitute the spatial vector $\mathbf{r}-\mathbf{r}'$ with $\mathbf{R} = \mathbf{r}-\mathbf{r}'$. The equation (A-12) becomes

$$\mathbf{B}(\mathbf{r}) = \frac{\mu_0}{4\pi}\int \frac{\mathbf{J}(\mathbf{r})\times\mathbf{R}}{R^3} dv' \tag{A-13}$$

where $R = \left|\mathbf{r}-\mathbf{r}'\right|$ is the magnitude of the vector $\mathbf{R}$. According to the vector identities $\frac{\mathbf{R}}{R^3} = -\nabla\frac{1}{R} = \nabla'\frac{1}{R}$ and $\mathbf{J}\times\nabla'\frac{1}{R} = \frac{(\nabla'\times\mathbf{J})}{R} - \nabla'\times\frac{\mathbf{J}}{R}$, equation (A-13) is transformed into

$$\mathbf{B}(\mathbf{r}) = \frac{\mu_0}{4\pi}[\int \frac{\nabla' \times \mathbf{J}^{\mathbf{P}}(\mathbf{r}')}{R} dv' - \int \frac{\nabla' \sigma \times \nabla' \Phi}{R} dv'] \tag{A-14}$$

in which ∇' means the operation is at location $\mathbf{r}'$ and the integral is across the volume v' that contains the source current. The first term in the right side of equation (A-14) denotes the magnetic field $\mathbf{B}_\infty(\mathbf{r})$ of the infinite homogeneous medium

$$\mathbf{B}_\infty(\mathbf{r}) = \frac{\mu_0}{4\pi} \int \frac{\nabla' \times \mathbf{J}^{\mathbf{P}}(\mathbf{r}')}{R} dv' = \frac{\mu_0}{4\pi} \int \mathbf{J}^{\mathbf{P}}(\mathbf{r}') \times \frac{\mathbf{R}}{R^3} dv' \tag{A-15}$$

Hereby the equation (A-14) is transformed to

$$\mathbf{B}(\mathbf{r}) = \mathbf{B}_\infty(\mathbf{r}) - \frac{\mu_0}{4\pi} \int \frac{\nabla' \sigma \times \nabla' \Phi}{R} dv' \tag{A-16}$$

Equation (A-16) suggests that generally, the magnetic field at the location $\mathbf{r}$ generated by a single current source at the location $\mathbf{r}'$ is determined by linear combination of the contributions from both primary and volume currents. The contribution from the primary current determines the head geometric independent item $\mathbf{B}_\infty(\mathbf{r})$, whereas the volume current contributes to the head geometric dependent second term. Thereby, to solve the forward problem of MEG, we need to have the information of the primary current $\mathbf{J}^{\mathbf{P}}(\mathbf{r}')$, and the distribution of the scalar potential Φ across the space.

As a special case, human head can be modeled as a volume conductor composed of a single compartment or multiple compartments separated by the boundaries between them. The compartments include brain tissue, cerebro-spinal fluid, skull and scalp with different conductivities. With the approximation of a homogenous, isotropic medium with constant conductivity $\sigma(\mathbf{r})$ within each compartment, distribution of the scalar potential Φ on the surface of each boundary

can be obtained by following steps if the geometric and conductivity information of each compartment are available. First, take divergence for both sides of the equation (A-11)

$$\nabla \cdot \mathbf{J}(\mathbf{r}) = \nabla \cdot \mathbf{J}^{\mathbf{P}}(\mathbf{r}') - \nabla \cdot (\sigma(\mathbf{r}) \nabla \Phi(\mathbf{r})) \tag{A-17}$$

Since with quasi-static approximation, $\nabla \cdot \mathbf{J} = 0$, thereby the potential $\Phi(\mathbf{r})$ at any point in the electric field is determined by

$$\nabla \cdot (\sigma(\mathbf{r}) \nabla \Phi(\mathbf{r})) = \nabla \cdot \mathbf{J}^{\mathbf{P}}(\mathbf{r}') \tag{A-18}$$

The solution of above equation comes from the second identity of the Green's theorem (Jackson 1999)

$$\int_G (\phi \nabla^2 \psi - \psi \nabla^2 \phi) d^3 v = \oint_S [\phi \nabla \Psi - \psi \nabla \phi] dS \tag{A-19}$$

where ϕ and ψ are arbitrary scalar fields. Substitute ψ and ϕ with $\frac{1}{R}$ and $\Phi(\mathbf{r})$, make use of the vector identity $\nabla^2 \frac{1}{R} = -4\pi\delta(\mathbf{r} - \mathbf{r}')$, the general solution of the scalar potential on the surface of each boundary is

$$\Phi(\mathbf{r}) = \frac{1}{4\pi\sigma(\mathbf{r}')} \int_{G'} \frac{\nabla \cdot \mathbf{J}^{\mathbf{p}}(\mathbf{r}')}{R} dv' + \frac{1}{4\pi} \oint_{S'} \left[\frac{1}{R} \frac{\partial \Phi(\mathbf{r}')}{\partial (\mathbf{n}(\mathbf{r}'))} - \Phi(\mathbf{r}') \frac{\partial}{\partial (\mathbf{n}(\mathbf{r}'))} \frac{1}{R} \right] dS' \tag{A-20}$$

where G' is the volume compartment enclosed by the boundary S', $\sigma(\mathbf{r})$ is the conductivity within the compartment, and **n(r')** is the outward unit norm of the surface S'. The single or multiple compartment model of human head suggests homogeneity within each compartment and different medium on each side of the boundary, thus if we model the head as a volume conductor with different inside and outside conductivity σ_i^- and σ_i^+ (i=1..m) across the surface S_i between the adjacent

compartments, the surface distribution of the potential $\Phi(\mathbf{r})$ can be obtained with transforming the equation (A-20) into (Geselowitz 1970)

$$\Phi(\mathbf{r}) = \frac{2\sigma_m}{\sigma_i^- + \sigma_i^+}\Phi_\infty(\mathbf{r}) + \frac{1}{2\pi}\sum_{i=1}^{m}\frac{\sigma_i^- - \sigma_i^+}{\sigma_i^- + \sigma_i^+}\oint_{S_i}\Phi_i(\mathbf{r}')\mathbf{n}_i(\mathbf{r}')\cdot\frac{\mathbf{R}}{R^3}dS' \qquad \text{(A-21)}$$

where $\Phi_\infty(\mathbf{r})$ is the electric potential in infinite homogenous medium

$$\Phi_\infty(\mathbf{r}) = \frac{1}{4\pi\sigma_0}\int_G \frac{\nabla\cdot\mathbf{J^p(r')}}{R}dv' = \frac{1}{4\pi\sigma_0}\int_G \mathbf{J^p(r')}\cdot\frac{\mathbf{R}}{R^3}dv' \qquad \text{(A-22)}$$

Once the distribution of the potential $\Phi(\mathbf{r})$ is obtained for each surface, the general forward solution of magnetic field can be computed by (Geselowitz 1967, 1970)

$$\mathbf{B}(\mathbf{r}) = \mathbf{B}_\infty(\mathbf{r}) + \frac{\mu_0}{4\pi}\sum_{i=1}^{m}(\sigma_i^- - \sigma_i^+)\cdot\oint_{S_j}\Phi(\mathbf{r}')\mathbf{n}_i(\mathbf{r}')\times\frac{\mathbf{R}}{R^3}dS' \qquad \text{(A-23)}$$

Practically, the primary current was usually modeled by an equivalent current dipole (ECD) as $\mathbf{J^p}(\mathbf{r}') = \mathbf{Q}\delta(\mathbf{r}-\mathbf{r}')$, where $\mathbf{Q}$ is the moment of the dipole current denotes both current strength and orientation.

As being demonstrated, the head model's geometric properties are necessary for MEG forward solution if the volume current is taking into account. Among the well-accepted head models such as the single sphere model (Cuffin & Cohen 1977), the concentric multiple sphere model (Mosher et al. 1999), and the realistic head shape model (Hämäläinen and Sarvas 1989) using the boundary element method (BEM), the single sphere one is fastest to compute but least accurate, whereas the BEM approach has the advantage of yielding accurate results with the limit of lengthy computation time. In this dissertation, the forward solution of MEG was based on a sensor-weighted multiple local spheres model (Huang et al. 1999). With computing

over-lapped approximate single-shell spheres for the MEG sensors by minimizing the deviant between the volume current contribution term from the local sphere and the real head shape, this model has the advantages of relative high accuracy and less computational load, where the anatomical map of the surfaces were obtained by anatomical magnetic resonance scan.

Thereby, if the information of the source current (i.e., location and moment for a dipole) is available, with the selected head model established based on the information obtained from the anatomical magnetic resonance (MR) scan, the MEG signal in sensor space can be simulated using the forward model. Furthermore, above derivation suggests that the forward solution of the external magnetic field can be written as a function linearly depends on the source current density

$$\mathbf{B}(\mathbf{r}) = \mathbf{L}(\mathbf{r}, \mathbf{r}') \cdot \mathbf{J}^{\mathbf{P}}(\mathbf{r}') \tag{A-24}$$

where $\mathbf{L}(\mathbf{r}, \mathbf{r}')$ is called the lead field and denotes the sensitivity of the sensors to source currents, which is determined by the geographic alignment of the sensors and the sources from the selected head models with known conductivity across the compartments in brain, also the contribution of individual source can be linearly superimposed to generate a forward solution for multiple sources.

Appendix B. The MEG inverse solution

In contrast to the forward solution of MEG, the inverse solution of MEG takes the opposite approach, where the sources are estimated with a specific lead field from the measurement of MEG sensors. The lead field is determined by the selected head model. Take the noise into account, the MEG measurement on the sensors generated by the sources inside the brain can be written as

$$\mathbf{B}(\mathbf{r}) = \mathbf{L}(\mathbf{r}, \mathbf{r}') \cdot \mathbf{s}(\mathbf{r}') + N \tag{B-1}$$

where $\mathbf{B}(\mathbf{r})$ is the $K \times T$ matrix of the MEG signals recorded from K sensors with T samples of each sensor, $\mathbf{s}(\mathbf{r}')$ is the $M \times T$ matrix denotes the source activity from M sources that generate the observed magnetic field, $\mathbf{L}(\mathbf{r}, \mathbf{r}')$ is the $K \times M$ matrix denotes the lead field, and N is the Gaussian distributed noise matrix. The inverse solution is to compute an approximate estimation of the source matrix $\hat{\mathbf{s}}(\mathbf{r}')$.

$$\hat{\mathbf{s}}(\mathbf{r}') = \mathbf{W}^{\mathrm{T}}(\mathbf{r}, \mathbf{r}')\mathbf{B}(\mathbf{r}) \tag{B-2}$$

There isn't a single solution of this equation since the ill-posed inverse problem. Methods have been developed to estimate the source activities, such as the least square methods with fixed number of sources, 'Bayesian' approaches with a priori knowledge of the weights among sensors, and spatial filtering beamformer methods, by which the source activity outside the spatial range of interest was minimized (for a review, see Baillet et al. 2001). In this dissertation, a locally constraint minimum variant (LCMV) beamformer approach was taken to estimate the dipole sources (van Veen et al. 1997), where the approximation of the transform

matrix $\mathbf{W}^{\mathbf{T}}(\mathbf{r},\mathbf{r}')$ is to minimize the variance of the spatially filtered output at the location of interest given the constraint of unity gain. For instance, for a location of interest $\mathbf{r}_q$ within the volume of the brain, the constraint of the transform matrix $\mathbf{W}^{\mathbf{T}}(\mathbf{r},\mathbf{r}')$ is to define a short distance δ, where for all sources at the location $\mathbf{r}'$ (also within the volume of the brain), the contribution to the sensor at location $\mathbf{r}$ is gained by a unity if the distance between $\mathbf{r}'$ and $\mathbf{r}_q$ is shorter than δ, while the contribution is null if the distance is out of range:

$$\mathbf{W}^{\mathbf{T}}(\mathbf{r},\mathbf{r}_q)\mathbf{L}(\mathbf{r},\mathbf{r}') = \begin{cases} \mathbf{I} & \left|\mathbf{r}_q - \mathbf{r}'\right| \le \delta \\ 0 & \left|\mathbf{r}_q - \mathbf{r}'\right| > \delta \end{cases} \tag{B-3}$$

Thus with the MEG measurements $\mathbf{B}(\mathbf{r})$ across the sensors, the estimation of each source $\hat{\mathbf{s}}(\mathbf{r}')$ can be obtained by equation (A-26) if the transform matrix $\mathbf{W}^{\mathbf{T}}(\mathbf{r},\mathbf{r}')$ is obtained, note that $\hat{\mathbf{s}}(\mathbf{r}')$ can be either a $1\times T$ vector to denote the power of the sources or a $3\times T$ matrix to represent the moments of the dipoles. With the approximation constraint of this method, the power $\left[\mathbf{W}^{\mathbf{T}}(\mathbf{r},\mathbf{r}')\mathbf{B}(\mathbf{r})\right]^2$ of each source need to be minimized, with matrix transformation, it turns into minimization of the cost function

$$\mathbf{W}^{\mathbf{T}}(\mathbf{r},\mathbf{r}')\mathbf{C}\mathbf{W}(\mathbf{r},\mathbf{r}') \tag{B-4}$$

subject to the constraint of the unity gain for the sources at the location of interest.

$$\mathbf{W}^{\mathbf{T}}(\mathbf{r},\mathbf{r}')\mathbf{L}(\mathbf{r},\mathbf{r}') = \mathbf{I} \tag{B-5}$$

In equation (A-28), the matrix $\mathbf{C}$ is the covariance matrix of MEG measurements. Applying the method of Lagrange multiplier, (28) and (29) can be combined into the cost function

$$\mathbf{W}^{\mathbf{T}}(\mathbf{r},\mathbf{r}')\mathbf{C}\mathbf{W}(\mathbf{r},\mathbf{r}') + \lambda\mathbf{W}^{\mathbf{T}}(\mathbf{r},\mathbf{r}')\mathbf{L}(\mathbf{r},\mathbf{r}') - \lambda \tag{B-6}$$

which needs to be minimized with respect to $\mathbf{W}^{\mathbf{T}}(\mathbf{r},\mathbf{r}')$. It can be solved with the partial differential equation

$$\frac{\partial}{\partial \mathbf{W}^{\mathbf{T}}(\mathbf{r},\mathbf{r}')}[\mathbf{W}^{\mathbf{T}}(\mathbf{r},\mathbf{r}')\mathbf{C}\mathbf{W}(\mathbf{r},\mathbf{r}') + \lambda\mathbf{W}^{\mathbf{T}}(\mathbf{r},\mathbf{r}')\mathbf{L}(\mathbf{r},\mathbf{r}') - \lambda] = 0 \tag{B-7}$$

which turns into solving the equation

$$2\mathbf{C}\mathbf{W}(\mathbf{r},\mathbf{r}') + \lambda\mathbf{L}(\mathbf{r},\mathbf{r}') = 0 \tag{B-8}$$

Combine equations (A-29) and (A-32), the solution is

$$\mathbf{W}(\mathbf{r},\mathbf{r}') = \frac{\mathbf{C}^{-1}\mathbf{L}(\mathbf{r},\mathbf{r}')}{\mathbf{L}^{\mathbf{T}}(\mathbf{r},\mathbf{r}')\mathbf{C}^{-1}\mathbf{L}(\mathbf{r},\mathbf{r}')} \tag{B-9}$$

where $\mathbf{L}(\mathbf{r},\mathbf{r}')$ is the lead field determined by the head model.

In this dissertation, the LCMV algorithms were used to estimate the dipole sources with experimentally measured MEG signal. The power of the source dipoles were normalized by the estimation of the noise to generate the activity index value, which was used as the measurement of the source activity for each dipole. Another method applied similar spatial filtering approach called dynamic imaging of coherent sources (DICS) was also used to estimate the functional interaction between sources, in which the dipole activities were estimated with band passed MEG measurement filtered by certain frequency, and the coherence between the localized sources were used as the measurement of the functional interaction between the corresponding regions (Gross et al. 2001).

Bibliography

Ahveninen J, Jaaskelainen IP, Raij T, Bonmassar G, Devore S, Hamalainen M, Levanen S, Lin FH, Sams M, Shinn-Cunningham BG, Witzel T, Belliveau JW. (2006) Task-modulated "what" and "where" pathways in human auditory cortex. Proc Natl Acad Sci USA. 103:14608-14613.

Alho K, Woods DL, Algazi A. (1994) Processing of auditory stimuli during auditory and visual attention as revealed by event-related potentials. Psychophysiology. 31: 469-479.

Armstrong KM, Fitzgerald JK, Moore T. (2006) Changes in visual receptive fields with microstimulation of frontal cortex. Neuron. 50: 791-798.

Aron AR, Robbins TW, Poldrack RA. (2004) Inhibition and the right inferior frontal cortex. Trends Cogn Sci. 8:170-177.

Aron AR (2007) The neural basis of inhibition in cognitive control. Neuroscientist. 13: 214-228.

Babajani A, Nekooei MH, Soltanian-Zadeh H. (2005) Integrated MEG and fMRI model: synthesis and analysis. Brain Topogr. 18:101-113.

Babajani A, Soltanian-Zadeh H. (2006) Integrated MEG/EEG and fMRI model based on neural masses. IEEE Trans Biomed Eng. 53: 1794-1801.

Baillet S, Mosher JC, Leahy RM. (2001) Electromagnetic Brain Mapping. IEEE Signal Processing Magazine. 18: 14-30.

Baldeweg T (2006) Repetition effects to sounds: evidence for predictive coding in the auditory system. Trends Cogn Sci 10:93-94.

Barbati G, Porcaro C, Zappasodi F, Rossini PM, Tecchio F. (2004) Optimization of an independent component analysis approach for artifact identification and removal in magnetoencephalographic signals. Clinical Neurophysiology 115: 1220-1232.

Bartlett EL, Wang X (2005) Long-lasting modulation by stimulus context in primate auditory cortex. J Neurophysiol. 94: 83–104.

Bell AJ, Sejnowski TJ. (1995) An information-maximazation approach to blind separation and blind deconvolution. Neural computation 7: 1129-1159.

Bergan JF, Ro P, Ro D, Knudsen EI. (2005) Hunting increases adaptive auditory map plasticity in adult barn owls. J Neurosci. 25: 9816-9820.

Binder J, Frost JA, Hammeke TA, Bellgowan PSF, Springer JA, Kaufman JN, Possing ET (2000) Human temporal lobe activation by speech and nonspeech sounds. Cereb Cortex 10:512 ‑ 528.

Blakemore SJ, Rees G, Frith CD (1998) How do we predict the consequences of our actions? A functional imaging study. Neuropsychologia 36: 521--529.

Bodner M, Kroger J, Fuster JM. (1996) Auditory memory cells in dorsolateral prefrontal cortex. Neuroreport. 7: 1905-1908.

Boemio A, Fromm S, Braun A, Poeppel D. (2005) Hierarchical and asymmetric temporal sensitivity in human auditory cortices. Nat Neurosci. 8: 389-395.

Brancucci A, Babiloni C, Babiloni F, Galderisi S, Mucci A, Tecchio F, Zapassodi F, Pizzella A, Romani GL, Rossini PM. (2004) Inhibition of auditory cortical responses to ipsilateral stimuli during dichotic listening: evidence from magnetoencephalography. European Journal of Neuroscience. 19: 2329-2336.

Brechmann A, Scheich H. (2005) Hemispheric shifts of sound representation in auditory cortex with conceptual listening. Cereb Cortex. 15: 578-587.

Brechmann A, Gaschler-Markefski B, Sohr M, Yoneda K, Kaulisch T, Scheich H. (2007) Working memory specific activity in auditory cortex: potential correlates of sequential processing and maintenance. Cereb Cortex. 17: 2544-2552.

Budinger, E., Heil, P., Scheich, H. (2000a) Functional organization of auditory cortex in the Mongolian gerbil (Meriones unguiculatus). III. Anatomical subdivisions and corticocortical connections. Eur. J. Neurosci. 12: 2425–2451.

Budinger, E., Heil, P., Scheich, H. (2000b) Functional organization of auditory cortex in the Mongolian gerbil (Meriones unguiculatus). IV. Connections with anatomically characterized subcortical structures. Eur. J. Neurosci. 12: 2452–2474.

Budinger, E., Heil, P., Hess, A., Scheich, H. (2006) Multisensory processing via early cortical stages – connections of the primary auditory field with other sensory systems. Neuroscience 143: 1065–1083.

Buschman TJ, Miller EK. (2007) Top-down versus bottom-up control of attention in the prefrontal and posterior parietal cortices. Science. 315: 1860-1862

Buxhoeveden DP, Casanova MF (2002) The minicolumn hypothesis in neuroscience. Brain. 125:935-951.

Carpenter GA, Grossberg S. (1987) ART2: Stable self-organization of category recognition codes for analog input patterns. Applied Optics. 26: 4919-4930.

Chadderdon GL, Sporns O. (2006) A Large-scale Neurocomputational Model of Task-oriented Behavior Selection and Working Memory in Prefrontal Cortex. J. Cogn. Neurosci. 18: 242–257.

Chait M, Simon JZ, Poeppel D. (2004) Auditory M50 and M100 responses to broadband noise: functional implications. 15: 2455-2458.

Chao LL, Knight RT. (1998) Contribution of human prefrontal cortex to delay performance. J Cogn Neurosci. 10: 167-177.

Chen JL, Zatorre RJ, Penhune VB (2006) Interactions between auditory and dorsal premotor cortex during synchronization to musical rhythms. Neuroimage. 32: 1771-1181.

Corchs S, Deco G (2002) Large-scale neural model for visual attention: integration of experimental single-cell and fMRI data. Cereb Cortex. 12: 339-348.

Colombo M, D'Amato MR, Rodman HR, Gross CG. (1990) Auditory association cortex lesions impair auditory short-term memory in monkeys. Science 247: 336–338.

Colombo M, Rodman HR, Gross CG. (1996) The effects of superior temporal cortex lesions on the processing and retention of auditory information in monkeys (Cebus apella). J. Neurosci. 16: 4501– 4517.

Condon CD, Weinberger NM (1991) Habituation produces frequency-specific plasticity of receptive fields in the auditory cortex. Behav Neurosci 105: 416-30.

Contreras-Vidal JL., Kerick SE. (2004) Independent component analysis of dynamic brain responses during visuomotor adaptation. NeuroImage 21: 936-945.

Cox RW. (1996) AFNI: Software for analysis and visualization of functional magnetic resonance neuroimages. Computers and Biomedical Research, 29: 162-173.

Cuffin BN, Cohen D. (1977) Magnetic fields of a dipole in special volume conductor shapes. IEEE Trans Biomed Eng. 24: 372-381.

David O, Friston K. (2003) A neural mass model for MEG/EEG: coupling and neuronal dynamics. NeuroImage. 20: 1743-1755.

David O, Kilner JM, Friston KJ. (2006) Mechanisms of evoked and induced responses in MEG/EEG. NeuroImage. 31(4):1580-1591.

Deco G, Rolls ET (2005) Attention, short-term memory, and action selection: a unifying theory. Prog Neurobiol. 76: 236-256.

Delorme A., Makeig S. (2004) EEGLAB: an open source toolbox for analysis of single-trial EEG dynamics including independent component analysis. Journal of Neuroscience methods. 134:9-21.

D'Esposito M, Postle BR, Jonides J, Smith EE. (1999) The neural substrate and temporal dynamics of interference effects in working memory as revealed by event-related functional MRI. Proc Natl Acad Sci U S A. 96:7514-7519.

Eimer M, van Velzen J, Driver J (2004) ERP evidence for cross-modal audiovisual effects of endogeneous spatial attention within hemifields. J Cogn Neurosci. 16: 272-288.

Forman SD, Cohen JD, Fitzgerald M, Eddy WF, Mintun MA, Noll DC. (1995) Improved assessments of significant activation in functional magnetic resonance imaging (fMRI): Use of a cluster-size threshold. 636-647.

Friston K, Jezzard P, Turner R. (1994) Analysis of functional MRI time-series. Hum. Brain Mapp. 1: 153– 171.

Friston, K (2005) A theory of cortical responses. Philos. Trans. R. Soc. Lond. B Biol. Sci. 360: 815–836.

Frith C, Dolan R. (1996) The role of the prefrontal cortex in higher cognitive functions. Brain Res Cogn Brain Res. 5:175-181.

Fritz J, Shamma S, Elhilali M, Klein D (2002) Rapid task-related plasticity of spectrotemporal receptive fields in primary auditory cortex. Nat Neurosci 6:1216-1223.

Fritz J, Elhilali M, Shamma S (2005) Differential Dynamic Plasticity of A1 Receptive Fields during Multiple Spectral Tasks. J. Neurosci 25(33):7623–7635.

Fritz JB, Elhilali M, David SV, Shamma SA. (2007) Auditory attention--focusing the searchlight on sound. Curr Opin Neurobiol. 17:437-455.

Fujiwara N, Nagamine T, Imai M, Tanaka T, Shibasaki H (1998) Role of the primary auditory cortex in auditory selective attention studied by whole-head neuromagnetometer. Cognitive Brain Research 7: 99–109.

Funahashi S (2006) Prefrontal cortex and working memory processes. Neuroscience. 139: 251-261.

Fuster JM, Alexander GE. (1971) Neuron activity related to short-term memory. Science. 173: 652-654.

Fuster JM. (1997) Network memory. Trends Neurosci. 20: 451-459.

Gisiger T, Kerszberg M, Changeux JP (2005) Acquisition and performance of delayed-response tasks: a neural network model. Cereb Cortex. 15: 489-506.

Gottlieb Y, Vaadia E, Abeles M. (1989) Single unit activity in the auditory cortex of a monkey performing a short term memory task. Exp Brain Res 74: 139–148.

Grady CL, Van Meter JW, Maisog JM, Pietrini P, Krasuski J, Rauschecker JP. (1997) Attention-related modulation of activity in primary and secondary auditory cortex. Neuroreport. 8: 2511-2516.

Grimm S, Roeber U, Trujillo-Barreto NJ, Schröger E. (2006) Mechanisms for detecting auditory temporal and spectral deviations operate over similar time windows but are divided differently between the two hemispheres. Neuroimage. 32: 275-282.

Gross J, Kujala J, Hamalainen M, Timmermann L, Schnitzler A, Salmelin R. (1999) Dynamic imaging of coherent sources: Studying neural interactions in the human brain. Proc Natl Acad Sci U S A. 98: 694-9.

Hämäläinen M, Hari R, Ilmoniemi R, Knuutila J, Lounasmaa OV. (1993) Magnetoencephalography -- theory, instrumentation and applications to noninvasive studies of the working human brain. Reviews of Modern Physics 65: 413-497.

Hämäläinen M, Sarvas J (1989) Realistic Conductivity Geometry Model of the Human Head for Interpretation of Neuromagnetic Data. IEEE Trans. Biomed. Eng. 36: 165-171.

Haenschel, C (2005) Event-related brain potential correlates of human auditory sensory memory-trace formation. J Neurosci 25: 10494–10501.

Hall DA, Hart HC, Johnsrude IS (2002) Relationships between Human Auditory Cortical Structure and Function. Audiol Neurootol 8:1–18.

Hari R (1990) The neuromagnetic method in the study of the human auditory cortex. *In Auditory Evoked Magnetic Fields and Electric Potentials. Adv. Audiol.* Grandori F, Hoke M, Romani GL (eds.) Basel, Karger, vol 6: 222-282.

Hari R, Levanen S, Raij T (2000) Timing of human cortical functions during cognition: role of MEG. Trends Cogn Sci. 4: 455-462.

Herdman AT, Wollbrink A, Chau W, Ishii R, Bernhard R, Pantev C (2003) Determination of activation areas in the human auditory cortex by means of synthetic aperture magnetometry. NeuroImage. 20:995-1005.

Hillyard SA, Hink RF, Schwent VL, Picton TW. (1973) Electrical signs of selective attention in the human brain. Science 182: 177-180.

Hlushchuk Y, Hari R. (2006) Transient suppression of ipsilateral primary somatosensory cortex during tactile finger stimulation. J Neurosci. 26: 5819-5824.

Horwitz B, Tagamets MA. (1999) Predicting human functional maps with neural net modeling. Hum. Brain Mapp. 8: 137– 142.

Horwitz B, Poeppel D. (2002) How can EEG/MEG and fMRI/PET data be combined? Hum Brain Mapp. 17: 1-3.

Horwitz B, Warner B, Fitzer J, Tagamets MA, Husain FT, Long TW. (2005) Investigating the neural basis for functional and effective connectivity. Application to fMRI. Philos Trans R Soc Lond B Biol Sci. 360: 1093-1108.

Houde JF, Nagarajan SS, Sekihara K, Merzenich MM. (2002) Modulation of the auditory cortex during speech: an MEG study. J Cogn Neurosci. 14:1125-1138.

Huang M, Mosher J, Leahy R. (1997) A sensor-weighted overlapping-sphere head model and exhaustive head model comparison for MEG. Phys Med Biol. 44(2):423-40.

Hughes RW, Jones DM. (2003) Indispensable benefits and unavoidable costs of unattended sound for cognitive functioning. 6:63-76.

Husain F, Tagamets M, Fromm S, Braun A, Horwitz B. (2004) Relating neuronal dynamics for auditory object processing to neuroimaging activity: a computational modeling and an fMRI study. Neuroimage. 21(4):1701-20.

Jääskeläinen IP, Ahveninen J, Bonmassar G, Dale AM, Ilmoniemi RJ, Levanen S, Lin FH, May P, Melcher J, Stufflebeam S, Tiitinen H, Belliveau JW (2004) Human posterior auditory cortex gates novel sounds to consciousness. Proc Natl Acad Sci USA 101:6809–6814.

Jackson JD. (1999) Classical electrodynamics, third ed. John Wiley & Sons, Inc. New York. 218-223.

James CJ, Gibson OJ. (2003) Temporally constrainted ICA: An application to artifact rejection in electromagnetic brain signal analysis. IEEE Trans.Biomed.Eng. 50:1108-1116.

Jones SR, Pritchett DL, Stufflebeam SM, Hämäläinen M, Moore CI. (2007) Neural correlates of tactile detection: a combined magnetoencephalography and biophysically based computational modeling study. J Neurosci. 27: 10751-10764.

Jonides J, Smith EE, Marshuetz C, Koeppe RA, Reuter-Lorenz PA. (1998) Inhibition in verbal working memory revealed by brain activation. Proc Natl Acad Sci U S A. 95: 8410-8413.

Jung TP, Makeig S, Humphries C, Lee TW, Mckeown MJ, Iragui V, Sejnowski TJ. (2000) Removing electroencephalographic artifacts by blind source separation. Psychophysiology 37: 163-178.

Kaas JH, Hackett TA, Tramo MJ. (1999) Auditory processing in primate cerebral cortex. Curr Opin Neurobiol. 9:164-70.

Kaiser J, Ripper B, Birbaumer N, Lutzenberger W. (2003) Dynamics of gamma-band activity in human magnetoencephalogram during auditory pattern working memory. Neuroimage. 20: 816-827.

Kiebel SJ, David O, Friston KJ (2006) Dynamic causal modelling of evoked responses in EEG/MEG with lead field parameterization. Neuroimage. 30:1273-1284.

Kikuchi-Yorioka Y, Sawaguchi T. (2000) Parallel visuospatial and audiospatial working memory processes in the monkey dorsolateral prefrontal cortex. Nat Neurosci. 3: 1075-1076.

Klimesch W (1997) EEG-alpha rhythms and memory processes. Int J Psychophysiol. 26: 319-340.

Klimesch W (1999) EEG alpha and theta oscillations reflect cognitive and memory performance: a review and analysis. Brain Res Brain Res Rev. 29: 169-195.

Klimesch W, Sauseng P, Hanslmayr S (2007) EEG alpha oscillations: the inhibition-timing hypothesis. Brain Res Rev. 53(1):63-88.

Knight RT, Staines WR, Swick D, Chao LL (1999) Prefrontal cortex regulates inhibition and excitation in distributed neural networks. Acta Psychol (Amst). 101: 159-178.

Kubovy, M., Van Valkenburg, D. (2001) Auditory and visual objects. Cognition 80: 97– 126.

Leiberg S, Kaiser J, Lutzenberger W (2006a) Gamma-band activity dissociates between matching and nonmatching stimulus pairs in an auditory delayed matching-to-sample task. Neuroimage. 30: 1357-1364.

Leiberg S, Lutzenberger W, Kaiser J (2006b) Effects of memory load on cortical oscillatory activity during auditory pattern working memory. Brain Res. 1120:131-140.

Levy R, Goldman-Rakic PS. (2000) Segregation of working memory functions within the dorsolateral prefrontal cortex. Exp Brain Res. 133: 23-32.

Liu Z, Ding L, He B. (2006) Integration of EEG/MEG with MRI and fMRI. IEEE Eng Med Biol Mag. 25: 46-53.

Logothetis NK, Pauls J, Augath M, Trinath T, Oeltermann A. (2001) Neurophysiological investigation of the basis of the fMRI signal. Nature. 412: 150-157.

Logothetis NK (2002) The neural basis of the blood-oxygen-level-dependent functional magnetic resonance imaging signal. Philos Trans R Soc Lond B Biol Sci. 357: 1003-37.

Logothetis NK (2003) The underpinnings of the BOLD functional magnetic resonance imaging signal. J Neurosci. 23: 3963-3971.

Lu ZL, Williamson SJ, Kaufman L (1992) Behavioral lifetime of human auditory sensory memory predicted by physiological measures. Science 258: 1668–1670.

Luo H, Husain F, Horwitz B, Poeppel D (2005) Discrimination and categorization of speech and non-speech sounds in an MEG delayed-match-to-sample study. NeuroImage. 28: 59-71.

Lütkenhöner B, Krumbholz K, Lammertamann C, Seither-Preisler A, Seinsträter O, Patterson RD (2003) Localization of Primary Auditory Cortex in Humans by Magnetoencephalography NeuroImage. 18: 58-66.

Lutzenberger W, Ripper B, Busse L, Birbaumer N, Kaiser J. (2002) Dynamics of gamma-band activity during an audiospatial working memory task in humans. J Neurosci. 22: 5630-5638.

Machens CK, Romo R, Brody CD. (2005) Flexible control of mutual inhibition: a neural model of two-interval discrimination. Science. 307:1121-1124.

Makeig S, Bell AJ, Jung T-P, and Sejnowski TJ. Independent component analysis of electroencephalographic data. In: D. Touretzky, M. Mozer and M. Hasselmo (Eds). Advances in Neural Information Processing Systems 8:145-151, MIT Press, Cambridge, MA 1996.

Makeig S, Jung TP, Bell AJ, Ghahremani D, Sejnowski TJ (1997) Blind separation of auditory event-related brain responses into independent components. Proc Natl Acad Sci U S A. 94(20):10979-10984.

Makeig S, Westerfield M, Jung TP, Covington J, Townsend J, Sejnowski TJ, Courchesne E. (1999) Functionally Independent Components of the Late Positive Event-Related Potential during Visual Spatial Attention. Journal of Neuroscience. 19: 2665-2680.

Makeig S, Westerfield M, Jung TP, Enghoff S, Townsend J, Courchesne E, Sejnowski TJ. (2001) Dynamic Brain Sources of Visual Evoked Responses. Science. 295: 690-694.

Malone BJ, Scott BH, Semple MN (2002) Context-dependent adaptive coding of interaural phase disparity in the auditory cortex of awake macaques. J Neurosci 22:4625-4638.

Marreiros AC, Kiebel SJ, Friston KJ (2008) Dynamic causal modelling for fMRI: a two-state model. Neuroimage. 39: 269-278.

Marsat G, Pollack GS. (2005) Effect of the temporal pattern of contralateral inhibition on sound localization cues. J Neurosci. 25: 6137-6144.

Martikainen MH, Kaneko K, Hari R (2005) Suppressed responses to self-triggered sounds in the human auditory cortex. Cereb Cortex. 15: 299-302.

May P, Tiitinen H, Ilmoniemi RJ, Nyman G, Taylor JG, Näätänen R (1999) Frequency change detection in human auditory cortex. J Comput Neurosci 6:99 – 120.

May PJ, Tiitinen H (2004) Auditory scene analysis and sensory memory: the role of the auditory N100m. Neurol Clin Neurophysiol 30;2004-2019.

Melara RD, Chen S, Wang H (2005) Inhibiting change: Effects of memory on auditory selective attention. Cognitive Brain Research 25: 431 – 442.

Miller EK, Cohen JD (2001) An integrative theory of prefrontal cortex function. Annu Rev Neurosci 24:167–202.

Miller P, Wang XJ. (2006) Inhibitory control by an integral feedback signal in prefrontal cortex: a model of discrimination between sequential stimuli. Proc Natl Acad Sci U S A. 103: 201-206.

Moody SL, Wise SP (2000) A model that accounts for activity prior to sensory inputs and responses during matching-to-sample tasks. J Cogn Neurosci. 12: 429-448.

Moran J, Desimone R. (1985) Selective attention gates visual processing in the extrastriate cortex. Science. 229: 782-784.

Mountcastle, VB (1979) An organizing principle for cerebral function: the unit module and the distributed system. In: F.O. Schmitt and F.G. Worden (Eds.), The Neurosciences 4th Study Program, Cambridge, MA: MIT Press, 1979.

Näätänen R, Picton T (1987) The N1 wave of the human electric and magnetic response to sound: a review and an analysis of the component structure. Psychophysiology. 24: 375-425.

Näätänen R (1990) The role of attention in auditory information processing as revealed by event-related potentials and other brain measures of cognitive function. Behavioral and Brain Sciences 13: 201-288.

Näätänen R, Tervaniemi M, Sussman E, Paavilainen P, Winkler I (2001) 'Primitive intelligence' in the auditory Cortex. Trends. Neurosci 24 (5): 283-288.

Nieder A. (2004) The number domain- can we count on parietal cortex? Neuron. 44:407-409.

Nieder A. (2005) Counting on neurons: the neurobiology of numerical competence. Nat Rev Neurosci. 6: 177-190.

Nelken I (2004) Processing of complex stimuli and natural scenes in the auditory cortex. Curr Opin Neurobiol. 14: 474-480.

Nunez PL, Silberstein RB (2000) On the relationship of synaptic activity to macroscopic measurements: does co-registration of EEG with fMRI make sense? Brain Topography. 13: 79-96.

Nunez PL and Srinivasan R (2006) Electric Fields of the Brain: The Neurophysics of EEG, 2nd Edition, New York: Oxford University Press.

Oatman LC. (1971) Role of visual attention on auditory evoked potentials in unanesthetized cats. 32: 341-356.

Oatman LC. (1976) Effects of visual attention on the intensity of auditory evoked potentials. Exp Neurol. 51: 41-53.

Ogawa S, Tank DW, R Menon RS, Ellermann JM, Kim SG, Merkle H, Ugurbil K. (1992) Intrinsic Signal Changes Accompanying Sensory Stimulation: Functional Brain Mapping With Magnetic Resonance Imaging. Proc. Natl. Acad. Sci. (USA), 89: 5951-5955.

Ohl FW, Scheich H. (2005) Learning-induced plasticity in animal and human auditory cortex. Curr Opin Neurobiol. 15: 470-477.

Pardo JV, Pardo PJ, Janer KW, Raichle ME. (1990) The anterior cingulate cortex mediates processing selection in the Stroop attentional conflict paradigm. Proc Natl Acad Sci U S A. 87: 256-259.

Palva S, Palva JM. (2007) New vistas for alpha-frequency band oscillations. Trends Neurosci. 30: 150-158.

Pasternak T, Greenlee MW. (2005) Working memory in primate sensory systems. Nat Rev Neurosci. 6(2):97-107.

Peterson DA, Thaut MH. (2002) Delay modulates spectral correlates in the human EEG of non-verbal auditory working memory. Neurosci Lett. 328: 17-20.

Pfurtscheller G, Neuper C, Mohl W. (1994) Event-related desynchronization (ERD) during visual processing. Int J Psychophysiol. 16: 147-153.

Poeppel D, Yellin E, Phillips C, Roberts TP, Rowley HA, Wexler K, Marantz A. (1996) Task-induced asymmetry of the auditory evoked M100 neuromagnetic field elicited by speech sounds.Brain Res Cogn Brain Res. 4: 231-242.

Poeppel D, Guillemin A, Thompson J, Fritz J, Bavelier D, Braun AR. (2004) Auditory lexical decision, categorical perception, and FM direction discrimination differentially engage left and right auditory cortex. Neuropsychologia. 42: 183-200.

Pollmann S, Maertens M. (2006) Perception modulates auditory cortex activation. Neuroreport. 17: 1779-1782.

Posner MI (1967) Short term memory systems in human information processing. Acta Psychol (Amst) 27: 267–284.

Postle BR, Berger JS, D'Esposito M (1999) Functional neuroanatomical double dissociation of mnemonic and executive control processes contributing to working memory performance. Proc Natl Acad Sci USA 96: 12959–12964.

Rämä P, Paavilainen L, Anourova I, Alho K, Reinikainen K, Sipilä S, Carlson S. (2000) Modulation of slow brain potentials by working memory load in spatial and nonspatial auditory tasks. Neuropsychologia. 38: 913-922.

Rauschecker JP, Tian B, Pons T, Mishkin M (1997) Serial and parallel processing in rhesus monkey auditory cortex. J Comp Neurol 382:89 – 103.

Rauschecker JP (1998) Parallel processing in the auditory cortex of primates. Audiol Neurootol 3: 86 – 103.

Rauschecker JP (1998) Cortical processing of complex sounds. Curr Opin Neurobiol. 8: 516 -521.

Riera JJ, Watanabe J, Kazuki I, Naoki M, Aubert E, Ozaki T, Kawashima R. (2004) A state-space model of the hemodynamic approach: nonlinear filtering of BOLD signals. Neuroimage21: 547-567.

Riera J, Aubert E, Iwata K, Kawashima R, Wan X, Ozaki T (2005) Fusing EEG and fMRI based on a bottom-up model: inferring activation and effective connectivity in neural masses. Philos Trans R Soc Lond B Biol Sci. 360(1457): 1025-1041.

Rinne T, Sarkka A, Degerman A, Schroger E, Alho K (2006) Two separate mechanisms underlie auditory change detection and involuntary control of attention. Brain Res. 1077: 135~143.

Roberts AC, Wallis JD. (2000) Inhibitory control and affective processing in the prefrontal cortex: neuropsychological studies in the common marmoset. Cereb Cortex. 10: 252-62.

Romanski LM, Bates JF, Goldman-Rakic PS (1999) Auditory belt and parabelt projections to the prefrontal cortex in the rhesus monkey. J Comp Neurol 403:141 – 157.

Romanski LM, Goldman-Rakic PS (2002) An auditory domain in primate prefrontal cortex. Nat Neurosci 5:15-16.

Romanski LM (2004) Domain specificity in the primate prefrontal cortex. Cogn Affect Behav Neurosci. 4:421-429.

Rong F, Contreras-Vidal JL. (2006) Magnetoencephalographic artifact identification and automatic removal based on independent component analysis and categorization approaches. J Neurosci Methods. 157(2):337-354.

Ruff CC, Blankenburg F, Bjoertomt O, Bestmann S, Freeman E, Haynes JD, Rees G, Josephs O, Deichmann R, Driver J. (2006) Concurrent TMS-fMRI and psychophysics reveal frontal influences on human retinotopic visual cortex. Curr Biol. 16: 1479-1488.

Sabri M, Liebenthal E, Waldron EJ, Medler DA, Binder JR (2006) Attentional modulation in the detection of irrelevant deviance: a simultaneous ERP/fMRI study. J Cogn Neurosci 18: 689-700.

Schafer EWP, Marcus MM (1973) Self-stimulation alters human sensory brain responses. Science 181: 175-177.

Schack B, Klimesch W, Sauseng P. (2005) Phase synchronization between theta and upper alpha oscillations in a working memory task. Int J Psychophysiol. 57:105-114.

Scheich H, Brechmann A, Brosch M, Budinger E, Ohl FW (2007) The cognitive auditory cortex: task-specificity of stimulus representations. Hear Res. 229:213-24.

Sotero RC, Trujillo-Barreto NJ. (2008) Biophysical model for integrating neuronal activity, EEG, fMRI and metabolism. Neuroimage. 39: 290-309.

Stanny R, Elfner L. (1980) A short-term memory influence on the N1 response of cerebral cortex. J Exp Psychol Hum Percept Perform. 6: 321-329.

Tagamets MA, Horwitz B. (1998) Integrating electrophysiological and anatomical experimental data to create a large-scale model that simulates a delayed match-to-sample human brain imaging study. Cereb. Cortex 8: 310– 320.

Tagamets MA, Horwitz B. (2000) A model of working memory: bridging the gap between electrophysiology and human brain imaging. Neural Netw. 13: 941-952.

Tagamets MA, Horwitz B. (2001) Interpreting PET and fMRI measures of functional neural activity: the effects of synaptic inhibition on cortical activation in human imaging studies. Brain Res Bull. 54: 267-273.

Talairach J, Tournoux P (1988) Co-planar Stereotaxic Atlas of the Human Brain: 3-Dimensional Proportional System - an Approach to Cerebral Imaging. Thieme Medical Publishers, New York, 1988.

Tang A., Pearlmutter B., Phung D., Reeb B. (2002) Independent component of Magnetoencephalography:localization. Neural computation. 14:1828-1857.

Ulanovsky N, Las L, Nelken I (2003) Processing of low-probability sounds by cortical neurons. Nat Neurosci 6:391-398.

Van Veen B, van Drongelen W, Yuchtman M, Suzuki A. (1997) Localization of brain electrical activity via linearly constrained minimum variance spatial filtering. IEEE Trans Biomed Eng. 44(9):867-80.

Vigario R., Sarela J., Jousmaki V., Hamalainen M., Oja E. (2000) Independent Component Approach to the analysis of EEG and MEG Recordings. IEEE Trans.Biomed.Eng. 47:587-593.

von Stein, A., Chiang, C., Konig, P. (2000). Top-down processing mediated by interareal synchronization. Proc. Natl. Acad. Sci. U. S. A. 97: 14748– 14753.

Warren JD, Zielinski BA, Green GGR, Rauschecker JP, Griffiths TD (2002) Perception of soundsource motion by the human brain. Neuron 34:139 – 148.

Wehr M, Zador A (2005) Synaptic mechanisms of forward suppression in rat auditory cortex. Neuron 47: 437-445.

Westbury CF, Zatorre RJ, Evans AC (1999) Quantifying variability in the planum temporale: A probability map. Cereb Cortex 9:392 – 405.

Wilson HR, Cowan JD (1972) Excitatory and inhibitory interactions in localized populations of model neurons. Biophys. J. 12: 1 – 24.

Winkowski DE, Knudsen EI. (2006) Top-down gain control of the auditory space map by gaze control circuitry in the barn owl. Nature. 439: 336-339.

Winkowski DE, Knudsen EI. (2007) Top-down control of multimodal sensitivity in the barn owl optic tectum. J Neurosci. 27: 13279-13291.

Woldorff MG, Gallen CC, Hampson SA, Hillyard SA, Pantev C, Sobel D, Bloom FE (1993) Modulation of early sensory processing in human auditory cortex during auditory selective attention. Proc Natl Acad Sci USA. 90:8722– 8726.

Wolpert DM, Kawato M (1998) Multiple paired forward and inverse models for motor control. Neural Netw. 11: 1317-1329.

Xiong J, Gao JH, Lancaster JL, Fox PT. (1995) Clustered pixels analysis for functional MRI activation studies of the human brain. Human Brain Mapping. 3: 287-301.

Zatorre RJ, Samson S (1991) Role of the right temporal neocortex in retention of pitch in auditory short-term memory. Brain 114: 2403–2417.

Zatorre RJ, Evans AC, Meyer E (1994) Neural mechanisms underlying melodic perception and memory for pitch. J Neurosci. 14: 1908–1919.

Zatorre RJ, Belin P (2001) Spectral and temporal processing in human auditory cortex. Cereb Cortex 11:946 – 953.

Zatorre RJ, Belin P, Penhune VB. (2002) Structure and function of auditory cortex: music and speech. Trends Cogn Sci. 6: 37-46.